NOVEL APPROACHES IN NON-DESTRUCTIVE UWB RF/ MICROWAVE CMOS INTEGRATED TIME DOMAIN SPECTROSCOPY SYSTEMS AND CIRCUITS

A Dissertation

by

ELIF KAYA

Submitted to the Graduate and Professional School of
Texas A&M University
in partial fulfillment of the requirements for the degree of

DOCTOR OF PHILOSOPHY

Chair of Committee,	Kamran Entesari
Committee Members,	Jose Silva-Martinez
	Jun Kameoka
	Jay Porter
Head of Department,	Miroslav M. Begovic

May 2022

Major Subject: Electrical Engineering

ABSTRACT

The ultra wide-band (UWB) systems are demanding for communication systems, radars, or spectroscopy stems. Recently, researchers have focused on expanding the use of RF/Microwave circuits and systems for multi-disciplinary applications. This dissertation aims to find new ways to integrate microwave broadband (MB) sensors and systems on CMOS integrated circuits (ICs) since system on chip (SoC) has great potential in the IC industry due to having a cheaper cost, more functionality, and smaller area. However, integration of these systems and sensors is challenging for their high-frequency operation, small area, low power consumption, required high sensitivity and accuracy. Furthermore, for today's microwave and mm-wave circuits and systems, miniaturization is an inevitable requirement. Therefore, developing novel miniaturized sensors/systems to reduce the physical size of the entire system while keeping their high-performance characteristics is highly desirable.

Various solid and liquid materials either absorb, transmit or reflect the microwave signal differently depending on several parameters such as their molecular structures, material compositions, shapes, and thicknesses. CMOS broadband dielectric spectroscopy (BDS) systems in RF/microwave frequencies intend to distinguish materials based on their complex relative permittivity, a unique response to an external microwave electric field at different frequencies. The CMOS BDS systems make it feasible to characterize materials over wide frequency ranges using a silicon-based mm-sized integrated chip that miniaturizes the overall system with low fabrication cost, high accuracy, and a smaller sample volume of the material under test (MUT). Due to its non-destructive, label-free, and real-time nature, microwave broadband dielectric spectroscopy (MBDS) is promising for various applications, such as food and drug safety, chemical/biological sensing, oil exploration and processing, disease diagnosis/tissue characterization, and biothreat detection. Traditional MBDS systems utilize either frequency-domain (FD) or time-domain (TD) measurement techniques. Conventional FD methods require bulky, heavy, and expensive instruments such as a high-cost vector network analyzer (VNA) and measurement setup that restrict

the use of the spectroscopy systems to only special applications in industry and laboratories. On the other hand, miniaturized CMOS TD MBDS systems first capture the output in the TD and then convert it to the FD using the fast Fourier transform (FFT), providing the MUT's dispersive and dissipative dielectric behavior versus frequency, while they can be convenient, cost and time-efficient, and have the potential of being portable in comparison with those FD methods. This dissertation addresses two CMOS integrated TD UWB spectroscopy systems for liquid chemicals' dielectric permittivity characterization.

In the first project, the first CMOS TD MBDS system with a homodyne RF transceiver architecture including an on-chip multitone excitation pulse generation and the contactless sensor consisting of two UWB Vivaldi antennas located in the near-field region is presented. The contactless system is implemented in a bistatic free space radar method where two antennas are placed on either side of MUTs, and the transmission signal is measured in TD to identify the complex permittivity from the phase delay and the amplitude mismatch introduced by the MUTs at the transmitted signal. The baseband signal is upconverted to RF frequencies in the transmitter using a UWB single-sideband (SSB) mixer to suppress the lower sideband of the exciting signal and prevent the signal distortion at the configured dc-free direct down-conversion receiver output. The system sub-blocks are designed with flat gain and constant group delay over the frequency range of 3-10 GHz to alleviate the impact of the entire system on MUT characterization. A prototype is fabricated in 65-nm CMOS process with an active chip area of 1.24 mm^2. The complex dielectric permittivity of different pure organic chemical liquids and mixtures has been detected and reported. The proposed CMOS MBDS system achieves an RMS permittivity error of less than 0.2%, and 0.4% for ϵ_r' and ϵ_r'' over the entire operation bandwidth.

In the second project, the first CMOS integrated UWB microwave coherent dual-comb spectroscopy (DCS) system with two on-chip frequency combs that have tunable and slightly different repetition frequency rates is presented for liquid chemicals detection. One of the frequency combs ($Comb_{RF}$) interrogates a coplanar waveguide (CPW) planar transmission line sensor loaded with the material under test (MUT) while the other identical empty sensor is excited by the second

comb ($Comb_{LO}$). Two frequency combs are then heterodyned using a UWB mixer to generate the dual-comb output representing the MUT's properties from microwave frequencies mapped to low-frequencies, eliminating the need to use high-frequency analog-to-digital converters (ADCs). To achieve detection of both real and imaginary parts of the complex permittivity of liquid samples, an adaptive sampling method along with phase-locking of all sources is utilized. The 3-10 GHz microwave DCS system is fabricated in 65-nm CMOS process and occupies a chip area of 1.98 mm^2. The proposed CMOS broadband microwave DCS system achieves an RMS permittivity error of less than 0.24$\%$, and 0.37$\%$ for ϵ_r' and ϵ_r'' over the entire desired bandwidth compared to sensor outputs.

DEDICATION

To my precious and devoted parents, Gültan and Orhan Kaya.

For their endless love, support, and encouragement.

Without whom none of my success would be possible.

"Science is the only true guide in life!" - Mustafa Kemal Atatürk

ACKNOWLEDGMENTS

"But still try for, who knows what is possible! It is the great beauty of our science that advancement in it, whether in a degree great or small, instead of exhausting the subject of research, opens the doors to further and more abundant knowledge, overflowing with beauty and utility."

Michael Faraday

Thanks be to God for giving me the patience and courage to complete this dissertation and fulfill the requirements for my Ph.D. degree.

First and foremost, I would like to express my gratitude to Professor Dr. Kamran Entesari for his guidance as an advisor. I wholeheartedly appreciate the freedom he gave me to do the research. This research would not be possible without his valuable scientific suggestions and the equipment and resources that were provided to me generously. I also would like to express my deepest gratitude to the members of my dissertation committee, Professor Dr. Jose Silva-Martinez, Professor Dr. Jun Kameoka, and Professor Dr. Jay Porter, for their advice, feedback, and timely responses to my requests.

I also would like to thank Prof. Aydin Karsilayan for supporting me in doing research on RFIC design. I should thank Prof. Samuel Palermo, Prof. Sebastian Hoyos, Prof. Laszlo B. Kish, and Prof. Robert D. Nevels for their teachings. I owe particular thanks to Professor Edgar Sanchez-Sinencio, who, although no longer with us, but has always been a source of inspiration and motivation in the Analog and Mixed-Signal Center Group. I am one of the luckiest people who had a chance to meet him and joined a couple of his classes. I would also like to thank members of the Department of Electrical and Computer Engineering, especially Ms. Ella Gallagher, Ms. Tammy Carda, Ms. Katie Bryan, Ms. Melissa Sheldon, Ms. Anni Brunker, Ms. Jeanne Prestwood, Ms. LaNita Jackson, and Ms. Rachel Rose for all their help throughout my years as a Ph.D. student.

A special note of appreciation goes to Professor Dr. Jose Silva-Martinez for employing me as a Graduate Teaching Assistant and introducing a new path for me for the first time. It has been a great honor to teach Analog Electronics Lab for his course. I have learned a lot from him through my Ph.D. I also would like to thank him for his kindness, continual support, and confidence in me.

I also would like to express my heartfelt gratitude to Professor James Pat Wallace of Engineering Technology and Industrial Distribution Department for employing me as his TA and later as Graduate Lecturer Assistant, providing me a second office as a personal study place, and for the numerous occasions in which he went way beyond the ordinary to help me out. I also would like to thank Prof. Reza Langari, Prof. Walter Buchanan, Dr. Robert M. Borsh, Ms. Susan Borsh, who always gives a hug whenever she sees me, Ms. Rosanne Gueguen, Ms. Wing Sze Wong, and Mr. Frank Cervantez for their help and support during my employment in the ETID department.

This research has been made possible by virtue of the support from many friends who have helped make my stay in College Station a pleasant and memorable experience throughout my time at Texas A&M University. I am immeasurably thankful to Merve Akdede for her sincere help, and she was the first person I met in Texas. I will always remember her and be thankful, may you rest in peace.

I also would like to extend my gratitude to my friends Gülçin Gülten and İzzet Şahin for the great moments we had together. You have been my emotional support and compassionate friends in College Station. Since the day we met, I cannot thank both of you enough for motivating me and always being by my side with your patience and support.

I also would like to thank Mohamed El-Kholy and Masoud Moslehi for all their help and discussions. I also would like to thank Negar Rashidi for her precious friendship and encouragement throughout my journey in the Analog and Mixed-Signal Center Group.

I also would like to thank my Graduate Teaching Assistant friends as supportive teammates. I have been fortunate to come across many good friends and colleagues, including MohammadHossein Naderi and his wife Sima Yaghoubi, Ramy Rady, and Alexander Edward, and special thanks go to my kind officemates, Fernando Lavalle and John Mincey.

I also would like to thank members of the Texas A&M University Office of Graduate and Professional Studies, International Student Services, Dr. Harry Hogan, Dr. Morgan Schweller, and Dr. Radhika Viruru for their supports through my teaching and research fellowship program, my mentors Dr. Rodney Boehm, Dr. Magda Lagoudas, and Dr. Saurabh Biswas during the Texas A&M University NSF Innovation Corps (I-Corps) Site Fellows program.

I also would like to express my appreciation to the Turkish Ministry of Education for the scholarship that has opened new gates to me and brought amazing opportunities, which I would not have been able to do alone.

Last, but most importantly, I am genuinely grateful to my parents, Gültan and Orhan, my sister Şafak, my twin-brother Tolga, my eldest brother Barış and his wife Gaye, my aunt Yazgül, and especially my nieces Naz and Mina for their dedication, endless patience, unconditional love, sacrifices and moral support in all my endeavors. I wonder if there is any way or any word that I could ever reveal my appreciation and gratitude to them. Although I am thousands of miles away from you, I feel your encouragement and prayers to pursue my Ph.D. degree; thank you for your belief in me under any condition. I dedicate this dissertation to you with all my heart and my love.

Finally, I also would like to thank God for giving me two invaluable cats Sakura and Akira, and I am very grateful for their accompany through my Ph.D. journey.

I feel the deepest gratitude to God for making me who I am and giving me all the beautiful things in my life. All of this happened because of your mercy, thank you God! And thank you for giving me the ability to thank you.

"Confidence comes from hours and days and weeks and years of constant work and dedication."

Roger Staubach

CONTRIBUTORS AND FUNDING SOURCES

Contributors

This work was supported by a dissertation committee consisting of Professor Dr. Kamran Entesari, Professor Dr. Jose Silva-Martinez, and Professor Dr. Jun Kameoka of the Department of Electrical and Computer Engineering, and Professor Dr. Jay Porter of the Department of Engineering Technology and Industrial Distribution.

All other work conducted for the dissertation was completed by the student independently.

Funding Sources

Graduate study was supported by a fellowship from Turkish Ministry of Education, Turkey, from 2014 to 2016, and Graduate Lecturer/Teaching Assistantship from Texas A&M University, from 2017 to 2021.

CMOS chip fabrications discussed in this dissertation are supported by the dissertation advisor, Professor Dr. Kamran Entesari.

TABLE OF CONTENTS

Page

ABSTRACT ii

DEDICATION v

ACKNOWLEDGMENTS vi

CONTRIBUTORS AND FUNDING SOURCES ix

TABLE OF CONTENTS x

LIST OF FIGURES xii

LIST OF TABLES xvii

1. AN INTRODUCTION TO ULTRA WIDE-BAND (UWB) DIELECTRIC SPECTROSCOPY SYSTEMS 1

    1.1 Overview of a Dielectric Spectroscopy and Terminology of the Complex Relative Permittivity 2
    1.2 Broadband Dielectric Spectroscopy 5
    1.3 Broadband Dielectric Measurement Techniques 5
    1.4 Design Challenges of Broadband Dielectric Spectroscopy 7
    1.5 Goals and Objectives of the Dissertation 8
    1.6 Organization of the Dissertation 10

2. PULSE-BASED BOARD-LEVEL BROADBAND DIELECTRIC SPECTROSCOPY SYSTEMS 12

    2.1 Motivation for Integrated Microwave Broadband Dielectric Spectroscopy Systems .. 12
    2.2 Contactless Sensing Unit 20
    2.3 Contacted-based Sensing Unit 24

3. AN ULTRA WIDE-BAND CMOS TIME DOMAIN COMPLEX DIELECTRIC SPECTROSCOPY SYSTEM USING A CONTACT-LESS SENSOR 29

    3.1 Introduction 29
    3.2 Contact-less Microwave Broadband Dielectric Spectroscopy Platform Architecture and System Analysis 32
        3.2.1 The Proposed MBDS Architecture and Frequency Planning: 33
        3.2.2 Contact-Less Near-Filed Sensor and MUT Cuvette: 38

3.2.3 System Analysis and Design Parameters: 39
3.3 Circuit Implementation 41
3.3.1 Transmitter Unit (TX) 41
3.3.1.1 Baseband Unit 41
3.3.1.1.1 Baseband Pulse Generation 41
3.3.1.1.2 PPF and Buffers 44
3.3.1.2 RF Unit 48
3.3.1.2.1 UWB SSB Up-converter 48
3.3.1.2.2 Differential-to-Single Ended Converter and Power Amplifier 49
3.3.2 Receiver Unit (RX) 51
3.3.2.1 UWB LNA 51
3.3.2.2 UWB Downconverter and Output Buffer 53
3.3.3 Quadrature LO Generation for Up/Down-Converter 54
3.4 System Integration and Test Set-up 56
3.5 Experimental Results 59
3.5.1 Electrical Characterization 59
3.5.2 Chemical Characterization and Calibration 59
3.6 Future Works for the Fully Integrated Contactless MBDS System 69
3.6.1 Miniaturized Contactless Fully Integrated MBDS Platform 69
3.6.2 On-chip Wideband Frequency Generation 72

4. A CMOS MICROWAVE UWB ADAPTIVE DUAL-COMB DIELECTRIC SPECTROSCOPY SYSTEM 74

4.1 Introduction 74
4.2 UWB Adaptive DCS System Design and Sensing Unit 77
4.2.1 Overall UWB Adaptive DCS System Architecture: 78
4.3 Sensor Design 81
4.4 Circuit Implementation 85
4.5 Fabrication and Experimental Results 89

5. CONCLUSION 95

REFERENCES 97

LIST OF FIGURES

FIGURE Page

1.1 Electromagnetic spectrum with wavelength, frequency, and energy with common spectroscopic techniques listed. (Reprinted from [1]) 2

1.2 Dielectric complex relative permittivities of ethanol and methanol versus frequency following the Cole-Cole model. 4

1.3 Survey of the measurement techniques used in the frequency range from 10^{-6} to 10^{15} Hz. (Reprinted from [2]) 6

1.4 (a) Concept of the TD MBDS for a two-port network (x(t) is the broadband input, h(t) models the sensing unit transfer function while it is loaded with the MUT, and y(t) is the output results of the convolution of x(t) and h(t) in TD), (b) a Dirac impulse in TD, and (c) output impulse response in FD. 8

2.1 (a) Block diagram of the first proposed contact-less board-level MBDS system, (b) Photograph of the fabricated first contactless board-level MBDS spectroscopy system, (c) generated 1 GHz BW BB pulse magnitude and (d) phase, (e) measurement of the proposed pulse in FD, and (f) conceptual signal spectrum representation before and after sensing unit loaded with MUT, respectively. (Modified from [17]) 13

2.2 (a) Block diagram of the second proposed contact-less board-level MBDS system, (b) Photograph of the fabricated second contactless board-level MBDS spectroscopy system, (c) generated 3.5 GHz BW BB pulse (SRD diode output) and upconverted TX output pulse (7 GHz BW) in TD, (d) magnitudes of SRD diode output pulse and upconverter output pulse and (e) their phase graphs, discrepancies circled, (f) conceptual signal spectrum representation of 3.5 GHz BW and 7 GHz BW pulses in FD along with their mirror images, and (g) UWB pulse and its image representation after passing through sensing unit loaded with MUT, respectively. (Modified from [18]) 15

2.3 (a) Block diagram of the proposed contacted-base board-level MBDS system, and (b) Photograph of the fabricated contacted-based board-level MBDS system, respectively. (Modified from [19]) 16

2.4 FD FFT calculated $\Delta\phi$ and ΔMag of the TD output voltage for different reference MUTs measurements: (a) and (b) second contactless board-level MBDS system, (c) and (d) contacted-based board-level MBDS system, respectively. (Adapted from [18,19]) 18

2.5 Comparison of measured and theoretical ϵ_r' and ϵ_r'' for unknown MUTs: (a) and (b) second contactless board-level MBDS system, (c) and (d) contacted-based board-level MBDS system, respectively. (Adapted from [18,19]) 19

2.6 (a) Two near-field coupled antennas faced each other, and the E-field distribution is shown in the middle and at the position of MUT at f = 3 GHz, (b) E-field distribution in a plane in between the two antennas where the MUT is located at different frequencies. The design values are W_{MUT}= h_{MUT} = 51 mm, and d = 30 mm, (c) E-field distribution on the edges of the MUT cuvette at 3 GHz, Fabricated UWB Vivaldi antennas simulated and measured return loss (d) and (e) group delay of the setup when the distance between the two antennas is 2d = 60 mm, and (f) simulated S11 of the setup when different MUTs are placed in between two antennas, respectively. (Adapted from [18]) 22

2.7 (a) Design of inductor: layout in Sonnet and its equivalent circuit, (b) 3-D layout of sensor with two stages and (c) equivalent circuit model, (d) impedance matching of the sensor to 50 Ω by adding attenuators, schematic of the sensor with two attenuators, S_{11} and (e) S_{21} simulated, (f) 3D response of the sensor ϵ', and (g) ϵ'', respectively. (Adapted from [19]) 26

3.1 Block diagram of the proposed contact-less TD MBDS system with frequency planning. (Reprinted from [7]) 34

3.2 Comparison of the Gaussian (a,b), first derivative of the Gaussian (c,d), sinc (a,b) and haversinc (c,d) as functions in time and frequency domains, respectively. (Reprinted from [7]) 37

3.3 Proposed baseband signal, (a) added five up-converted Gaussian pulses and, (b) flat spectrum and linear phase change in 1 GHz. (Reprinted from [7]) 38

3.4 Baseband Unit; (a) transistor level circuit of baseband pulse generator along with PPF unit, (b) circuit topology of the baseband mixer, (c) up-converted Gaussian pulses at the input of analog adder, (d) simulation results of the generated baseband pulse in TD and, (e) its spectrum, respectively. (Reprinted from [7]) 40

3.5 Baseband LO generation block diagram (a), high/low frequency clock generation,(b), and (c) TSPC-H/L DFF transistor level circuits , respectively. (Reprinted from [7]) 43

3.6 (a) Measured baseband pulse in TD, and (b) measured pulse spectrum. (Reprinted from [7]) 44

3.7 (a) Transistor level schematic of the 5-stage PPF network with 2-stage output buffers , (b) generated quadrature I/Q outputs in time domain, and (c) magnitude and phase mismatches of the quadrature signals. (Reprinted from [7]) 45

3.8 (a) Block diagram of the SSB upconverter along with the conceptual signal spectrum , and (b) transistor-level schematic of the UWB TX RF Unit (UWB SSB up-converter, DTS, and UWB PA). (Reprinted from [7]) 47

3.9 Simulation results of the lower-sideband suppression ratio (LSSR) for each sub-carrier with 800 MHz BW at RF TX output over 3-10 GHz. (Reprinted from [7])..... 49

3.10 UWB Transmittersimulation results, (a) S21 of the UWB PA and Mixer+PA, and (b) group delay (GD) of the UWB PA and Mixer+PA. (Reprinted from [7]) 50

3.11 Schematic of RX front-end for the proposed miniaturized contactless microwave broad band dielectric spectroscopy (MBDS) system. (Reprinted from [7])..... 51

3.12 RX front-end simulation results, (a) phase and magnitude difference of the differential output of the LNA, (b) S21, S11 of the UWB LNA and conversion gain (CG) of the LNA+Mixer, (c) noise figure (NF) of the LNA and LNA+Mixer, and (d) group delay (GD) of the LNA and LNA+Mixer. (Reprinted from [7]) 53

3.13 Circuit topology of differential quadrature LO generation/distribution unit, (a) CML frequency divider-by-2, (b) divider schematic, and (c) CML-to-CMOS converter and duty cycle corrector. (Reprinted from [7]) 55

3.14 (a) Micrograph of the fabricated MBDS sytem chip, and (b) test set-up for the proposed MBDS system with packaged chip, respectively. (Reprinted from [7]) 57

3.15 (a) Measured magnitude of nine sub-carriers at TX output with flat spectrum , and (b,c,d) measured sub-carriers 1, 5, and 9 in TD, respectively. (Reprinted from [7])... 58

3.16 (a) $\Delta\phi$-phase and (b) ΔMag-magnitude measurement results of the proposed MBDS system compared with the VNA, and (c) system output in TD for sub-carrier5. (Reprinted from [7]) 60

3.17 Theoretical ϵ_r' and ϵ_r'' curves over the frequency range of 0-20 GHz for the MUTs used in Fig. 3. 16. (Reprinted from [7]) 61

3.18 Measured $\Delta\phi$ and ΔMag as a function of theoretical ϵ_r' and ϵ_r'' at 3-6-and-10 GHz. (Reprinted from [7]) 62

3.19 Measured $\Delta\phi$ and ΔMag for the reference materials as a function of ϵ_r' and ϵ_r'' at 3-6-and-10 GHz, respectively, along with the fitted curves. (Reprinted from [7])..... 63

3.20 Coefficients of ϵ_r'-$\Delta\phi$ and ϵ_r''-ΔMag versus frequency. (Reprinted from [7]) 64

3.21 3-D plots of the fitted curves, $\Delta\phi$ versus ϵ_r' and ΔMag versus ϵ_r'' with respect to frequency. (Reprinted from [7]) 65

3.22 ϵ_r' and ϵ_r'' measurement versus frequency for acetone as unknown MUT. (Reprinted from [7]) 66

3.23 ϵ_r' and ϵ_r'' measurement versus frequency for ethanol and methanol mixtures with the mixing ratios q=0,10,...,100$\%$. (Reprinted from [7]) 67

3.24 The block diagram of the possible contactless fully integrated MBSD system. 70

3.25 The block diagram of the possible frequency synthesizer for a self-sustained fully integrated MBSD system..... 73

4.1 Block diagram of the proposed microwave broadband DCS system. (Reprinted from [99])..... 78

4.2 DCS system combs in TD and FD. (Reprinted from [99]) 80

4.3 Proposed sensing unit conceptual structure and MUT loaded case (strips are not shown), (a) and (b) top and side views, and (c) 3D layout of the S-CPW sensor, respectively.(Reprinted from [90,99]) 83

4.4 S_{11} simulated magnitude results of the loaded sensor with different MUTs..... 84

4.5 S_{21} simulated magnitude (a) and phase (b) results of the loaded sensor with different MUTs. (Reprinted from [90]) 84

4.6 Circuit schematic of the proposed DCS system. (Reprinted from [99])..... 86

4.7 (Continue of Fig.4.6) Circuit schematic of the proposed DCS system. (Reprinted from [99])..... 87

4.8 (a) Generated Gaussian monopulse in FD, and (b) generated on-chip UWB pulse in FD, respectively. (Reprinted from [99])..... 88

4.9 (a) Micrograph of the fabricated DCS sytem, (b) plastic tube glued on top of chip, and (c) partially packaged chip (only the sensor of the test path is open). (Reprinted from [90,99]) 90

4.10 Measurement results of the proposed DCS system in TD. (Reprinted from [99]) 91

4.11 (a) Magnitude and (b) phase measurement results of the proposed DCS system in FD for ethanol, methanol, and water, respectively. (Reprinted from [99]) 92

4.12 Output (a) Magnitude and (b) phase difference from the reference material measurement, FFT results of the proposed DCS system in FD for ethanol, methanol, and water, respectively. 93

LIST OF TABLES

TABLE Page

3.1 Sytem Level Design Parameters of UWB RF Receiver Blocks (Reprinted from [7]) . 39

3.2 Performance Summary and Comparison with State of the Art (Reprinted from [7]) .. 68

4.1 CMOS Dielectric Microwave Detector Comparison with State of the Art 94

1. AN INTRODUCTION TO ULTRA WIDE-BAND (UWB) DIELECTRIC SPECTROSCOPY SYSTEMS

A system-on-chip (SoC) integrates multiple blocks onto a single substrate necessary to implement an electronic system that provides multiple advantages, including lower cost and power consumption and reduced size of products. With the recent advancements of the complementary metal-oxide-semiconductor (CMOS) technologies, the feature size of transistors is gradually dropping; therefore, SoC concepts require a massively increased number of transistors have a high interest in the multi-disciplinary research that focuses on expanding the use of integrated electronics and systems including applications such as chemical/biochemical sensors, biomedical devices, and micro-electromechanical systems (MEMS). The global trend in these research areas is moving toward self-sustained and fully integrated SoC platforms and even lab-on-chip systems to achieve a stand-alone operation without the need of any external equipment that provides portable, miniaturized, inexpensive, and simple designs without bulkiness.

The research presented in this dissertation addresses the concept of employing the methods to implement and fabricate compact on-chip spectroscopy systems within the radio frequency (RF), and microwave (MW) frequency ranges to identify liquid organic and binary-mixture chemicals using their dielectric permittivity properties.

The goal of this dissertation is to conduct precision and high-accuracy research utilizing laboratory-based measurements to characterize the dielectric properties of unknown materials, as well as, to perform a careful signal processing method using captured measurement data while applying calibration techniques for the measurement and system uncertainties and nonlinearities to achieve reliable interpretation of the targeted unknown material dielectric permittivity extraction from the uniquely determined dielectric spectra of the sample over frequency. This research is important in view of the need for miniaturized system designs that enable portable, efficient, effective, fast, real-time, and affordable dielectric spectroscopy systems.

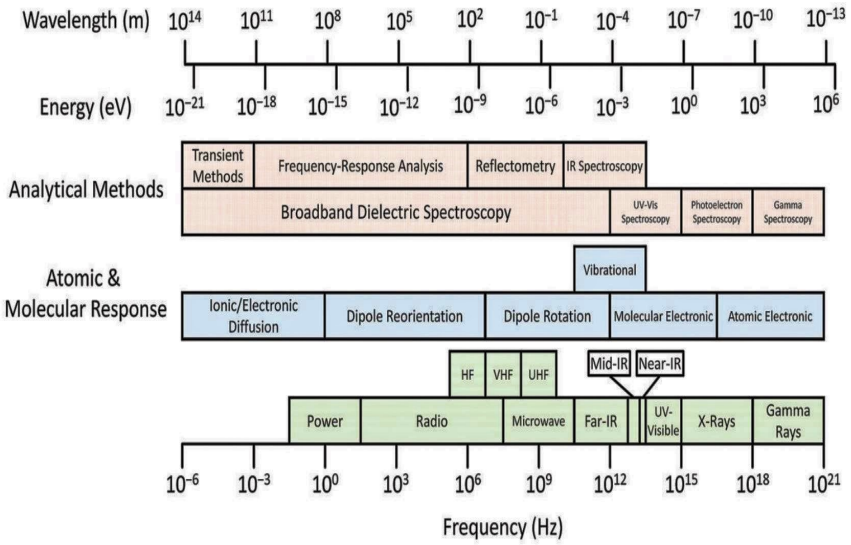

Figure 1.1: Electromagnetic spectrum with wavelength, frequency, and energy with common spectroscopic techniques listed. (Reprinted from [1])

1.1 Overview of a Dielectric Spectroscopy and Terminology of the Complex Relative Permittivity

The characteristics of materials/objects can be determined by their electric or magnetic properties. Electrical properties of a material can be defined when exposed to an external electric field; in contrast, magnetic properties can be defined when exposed to an external magnetic field. Electrical properties are specified by conductivity "σ" and permittivity "ϵ".

Spectroscopy is a system that presents the reciprocal influences between matter and electromagnetic radiation. Generally, specific types of radiation are absorption, transmission, or emission, which are defined by frequency, wavelength, or energy, as shown in Fig. 1.1 [1].

Dielectric spectroscopy shows the interaction between the sample and a portion of the signal's spectrum that is a time-varying electric field with frequency. Spectra are complex, and each spectrum holds a wide variety of information. Dielectric spectroscopy (DS) is a powerful measurement technique for detecting complex relative permittivity $\epsilon_r^* = \epsilon_r' - j\epsilon_r''$ as a unique subscription of materials over frequency. A transmitted or reflected signal through a material (liquid/solid) can give complex permittivity of material over frequency [2].

Real relative permittivity ϵ_r' indicates how much energy from an external electric field is stored by the sample, while imaginary relative permittivity ϵ_r'' indicates how lossy the sample is to an external electric field.

By measuring the dielectric spectra response of the sample, we can relate the effect of structure influencing its dielectric properties on the amplitude and phase of the transmitted signal through the material to define its dispersive and dissipation characteristics.

Many representations exist for frequency dispersive complex permittivity, which shows the frequency dependency of the complex relative permittivity for a large class of compounds. The Cole-Cole representation [3–6] is one of the most common equations and is given by,

$$\epsilon_r^* = \epsilon_r' - j\epsilon_r'' = \epsilon_\infty \frac{\epsilon_0 - \epsilon_\infty}{1 + (jw\tau)^{1-\alpha}} \tag{1.1}$$

where ϵ_0 and ϵ_∞ are the "static" (at zero frequency) and "infinite frequency" (at ∞) dielectric permittivity constants, w is the angular frequency, τ is the characteristic relaxation time, and α is the relaxation time distribution parameter (has a value between 0 and 1), while these parameters are constant for a particular material and vary for another material. As an example, the relative permittivities of ethanol and methanol as a function of frequency using their reported Cole-Cole parameters are given in Fig. 1.2.

On the other hand, the complex relative permittivity of a binary mixture (composed of at least two materials with ratios) is a function of the complex permittivities of the two constituting materials and the fractional volume ratio, which can be represented mathematically as follows [6]:

$$\frac{\epsilon_{eff} - \epsilon_e}{\epsilon_{eff} + 2\epsilon_e + v(\epsilon_{eff} - \epsilon_e)} = \frac{\epsilon_i - \epsilon_e}{\epsilon_i + 2\epsilon_e + v(\epsilon_{eff} - \epsilon_e)} \tag{1.2}$$

where ϵ_{eff} is the effective mixture permittivity, ϵ_e is the permittivity of the environment, ϵ_i is the inclusion permittivity, and v is a parameter to define the employed model (has a value of 0, 2, or 3 corresponding to Maxwell–Garnett, Polder-van Santen, and quasi-crystalline approximation rules).

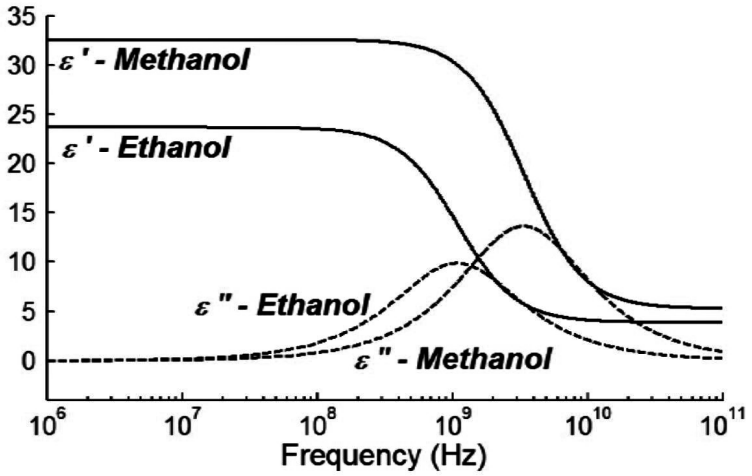

Figure 1.2: Dielectric complex relative permittivities of ethanol and methanol versus frequency following the Cole-Cole model.

The dielectric permittivity of many materials has a solely unique frequency response at RF/microwave frequencies. Taking advantage of this property, microwave broadband dielectric spectroscopy (MBDS), which is a non-destructive, cost-effective, and real-time characterization procedure, is a promising technique to determine the complex permittivity of materials for a wide range of applications, including chemical/biological sensing, biomedical devices (such as microwave thermography and tomography), disease diagnosis (such as distinguishing breast cancer cells, monitoring blood glucose concentration, and identifying antibodies, etc.), bio-threat detection, oil exploration and processing, agriculture and food quality/safety, and drug development in the pharmaceutical industry [7].

At microwave frequencies, some studies have shown that the dielectric properties of biological samples such as blood [8, 9], semen [10], and cerebra spinal fluid [11] show the discernible change in patients regarding specific diseases compared to healthy people. As a result, MBDS systems have a great potential for specific point-of-care clinical system applications, which need portable devices that can rapidly extract required medical information from a small amount of biological sample. For example, glucose concentration detection in blood by means of dielectric measurements can have potential applications in blood sugar control for diabetics [12]. As another

example, cancerous cells can be distinguished from healthy cells since dead cells have a different response from living cells; therefore, the extraction of electrical properties of cancerous cells can be helpful for early detection and treatment. In addition, the dielectric constant is an important property to define the polarity of organic chemicals such as solvents used in the chemical industry. Furthermore, knowledge of complex dielectric properties at microwave frequencies is essential to develop microwave techniques that can be used to understand possible health hazards and non-thermal effects of microwave signals to the end-users.

1.2 Broadband Dielectric Spectroscopy

The need for broadband microwave dielectric spectroscopy is quite relevant for more accurate complex relative permittivity characterization of the above mentioned applications. Dielectric complex permittivity measurement within a broader range of frequencies is required to define interactions of the material under test (MUT) with signal since many materials might share the same value of the real/imaginary relative permittivity at a single certain frequency point. Therefore, for high accuracy, detection of the unique frequency dispersive characteristics of the MUT over a broad frequency range is needed. Furthermore, ionic liquids fail during the zero-frequency complex permittivity detection due to their high electrical conductance properties at low frequencies; on the other hand, the complex dielectric permittivity properties of these liquids can be easily extracted at microwave frequencies [13].

1.3 Broadband Dielectric Measurement Techniques

The complex dielectric permittivity can be measured within an extraordinary broad frequency span from 10^{-6} to 10^{12} Hz while therein different measurement techniques based on various measurement methods as shown in Fig. 1.3 [2].

UWB microwave dielectric spectroscopy measurement techniques can be categorized as frequency-domain (FD) and time-domain (TD). FD measurement techniques commonly utilize a frequency sweeping source such as a vector network analyzer (VNA) (a complex, power-hungry source) for broadband sensing to directly measure the complex dielectric permittivity of the material in the FD.

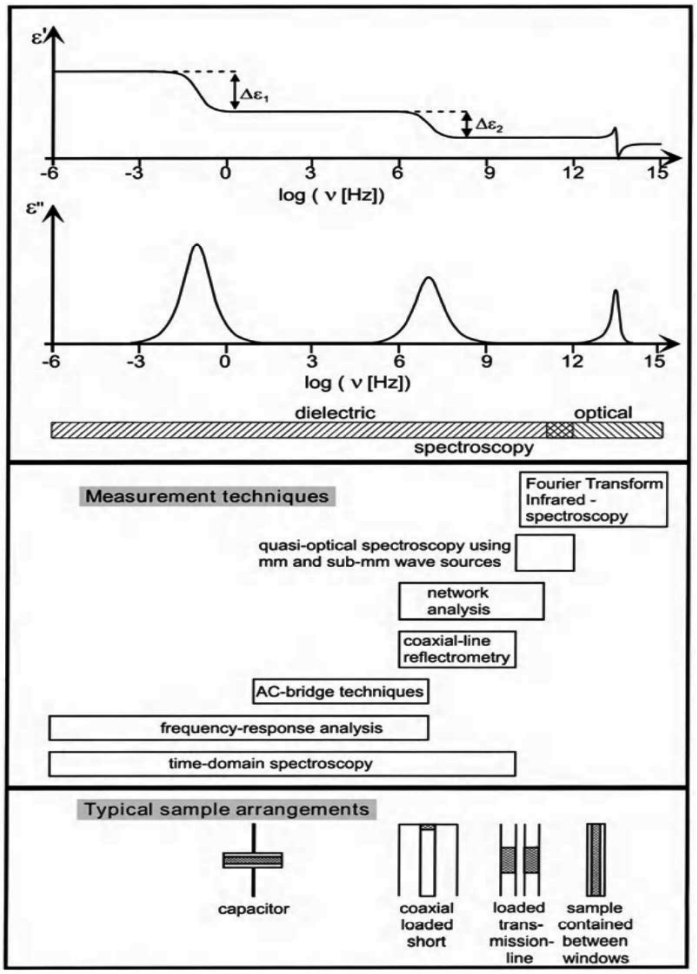

Figure 1.3: Survey of the measurement techniques used in the frequency range from 10^{-6} to 10^{15} Hz. (Reprinted from [2])

Contrarily, TD measurement techniques utilize an impulse UWB pulse with a short duration in the TD that provides the entire frequency content of the desired frequency span, which carries the complex dielectric properties of the test material, while this signal is first captured in the TD and then converted to the FD using the fast Fourier transform (FFT) approach [14, 15]. Although this makes the TD technique as fast in nature, due to the low spectral frequency resolution compared to a single frequency measurement such as a resonance point, the output signal has to be averaged to improve the signal-to-noise ratio (SNR), resulting in a low or moderate speed comparable to that of an FD technique.

1.4 Design Challenges of Broadband Dielectric Spectroscopy

Ultra-wideband (3.1 to 10.6 GHz) has a wide range of applications such as wireless communication systems, radars, medical-image systems, spectroscopy systems, and vehicular communications while it provides high data rate, low cost, and low power dissipation. However, it has limiting factors, including integration of required broadband functional blocks, on-chip broadband pulse generation, chip area, and analog-to-digital converter (ADC) design due to its bandwidth (BW, 7 GHz). Furthermore, broadband dielectric spectroscopy requires high sensitivity and dynamic range for a wideband frequency range operation. UWB microwave sensing unit exhibits changes in the transmitted signal when exposed to MUTs. The interface circuitries convert these sensing element changes into a baseband signal that can be easily extracted and readout for material detection.

The challenges of system-on-chip/lab-on-chip UWB microwave dielectric spectroscopy implementation is summarized as follows:

1. Implementation of UWB on-chip/onboard sensing unit,

2. Implementation of UWB on-chip pulse generation and shape of the pulse for accurate material characterization,

3. Implementation of UWB RF circuits such as Low-noise Amplifier (LNA) and up/down converter mixers, which require low noise, stability, high gain, and phase linearity due to the material dispersive and dissipation characteristics, elimination of the effects of interference, harmonics, leakages of RF/LO signals, DC-offsets, flicker noise,

4. Miniaturization and simplification of on-chip self-sustained broadband spectroscopy at microwave frequencies for portable systems while achieving high sensitivity, high dynamic range, and high accuracy,

5. Minimizing the consumption of test materials while dealing with the chemical liquids' leakages on the surface of the chip to the entire system,

6. Developing sensing algorithms, including sensor and system calibration for accurate dielectric permittivity characterization,

7. Developing mathematical models to match the captured measurement values to reported

theoretical permittivities of the materials to generate a database for unknown material detection while having faster readout rates.

1.5 Goals and Objectives of the Dissertation

The primary objective of this dissertation is to propose, implement and validate on-chip UWB microwave dielectric spectroscopy system prototypes for liquid chemical detection in the TD by taking advantage of recent advances in circuit miniaturization and integration techniques, along with novel system architectures.

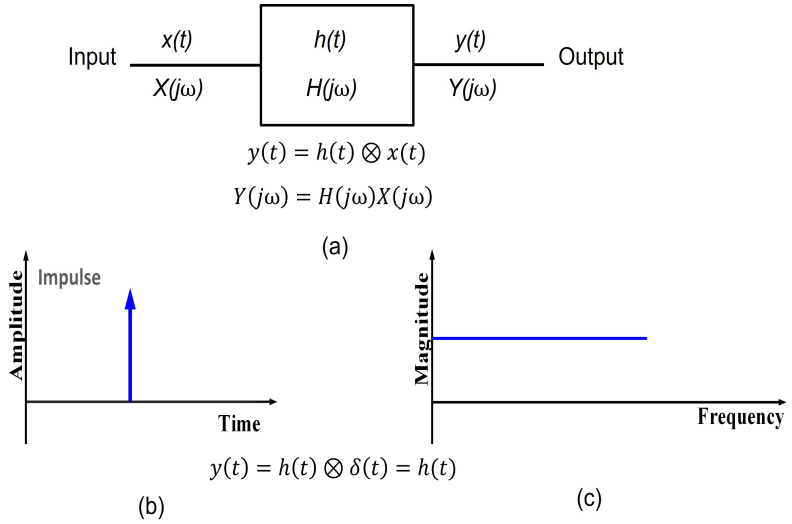

Figure 1.4: (a) Concept of the TD MBDS for a two-port network (x(t) is the broadband input, h(t) models the sensing unit transfer function while it is loaded with the MUT, and y(t) is the output results of the convolution of x(t) and h(t) in TD), (b) a Dirac impulse in TD, and (c) output impulse response in FD.

The concept of the TD MBDS for a two-port network is depicted in Fig. 1.4 (a). This two-port network symbolizes the sensing unit loaded with an MUT. While the sensing unit is excited by a short duration pulse, the input pulse $x(t)$ will be convolved with the transfer function of the sensing unit $h(t)$ in the TD $y(t)$ equals multiplication in the FD $Y(jw)$, in other words, in the FD the corresponding relation is given by Fourier transformation as shown in Fig. 1.4 (b).

The magnitude and phase of the two-port network transmission coefficients ($S_{21_{magnitude,phase}}$) will be changed while the input signal is exposed to the MUT due to its dispersive properties. This will cause insertion loss and phase delay of $y(t)$, which will vary with different MUTs relative to the $x(t)$. The variation in the insertion loss has the information of the imaginary part of the MUT's relative complex dielectric constant (ϵ_r''), while the phase change is related to the real part (ϵ_r') [16]. Fig 1.4 (c) illustrates that if the system is excited by a Dirac impulse $\delta(t)$, the output becomes $h(t)$; hence the impulse response results as a sensing unit transfer function.

This verifies that if the excitation pulse has a uniform spectrum in the FD, the output $y(t)$will represent only exactly the sensing unit response, including the loaded MUT effects, and hence, after the empty sensing unit response calibration out from the loaded sensing unit response (subtract), the resulted TD output will express the only magnitude and phase information of the MUT.

Considering the concepts mentioned above, the objective of this dissertation is summarized as follows:

1- Implementing a portable miniaturized prototype for chemical sensing at UWB microwave frequencies that does not rely on bulky and expensive pulse generators (Vector Network Analyzer (VNA) or high-frequency arbitrary wave generator (AWG)) as transmitters and laboratory settings such as high-speed oscilloscopes as receivers,

2- Developing signal processing algorithms to measure complex dielectric permittivity highly accurately,

3- Designing blocks that are conventionally needed to be off-chip to maximize integration while minimizing the total size and cost of the prototype,

4- Generating an on-chip broadband excitation pulse that has uniform spectra while designing required circuitry parts of the MBDS that provide flat gain and linear phase change or constant group delay through the entire system for detection of complex permittivity,

5- Implementing a DC-free RF homodyne transceiver (TRX) in the TD for a more compact product and simplified frequency synthesizer,

6- Maximizing the frequency and dynamic range of the operation to increase the functionality

of the product,

7- Reducing the effect of the DC-offsets, flicker noise, temperature, and environment variations to improve the overall system sensitivity,

8- Implementing sensing units that either prevents chemical leakages (contact-less) or minimize their effects of it (contacted-base),

9- For further improvement, design a dual-comb spectroscopy with on-chip calibration and time/phase correction via adaptive sampling.

Realizing the pulse generation, transmitter, and receiver on a single chip results in significant cost and size reduction, low power consumption, enormous processing, and higher throughput

To the best of the author's knowledge, according to all reported on-chip/on-board frequency and time domain spectroscopy techniques, there is no work reported in the literature on homodyne transceiver architecture. There is no work reported in the literature as dual-comb spectroscopy has phase lock and auto phase/time correction and system calibration at microwave frequencies.

1.6 Organization of the Dissertation

The dissertation contains five sections, besides the introduction section. This dissertation targets to introduce miniaturized novel integrated CMOS sensing systems suitable for complex dielectric spectroscopy in the 3 to 10 GHz UWB frequency range. The organization is as follows:

Chapter II discusses the motivation that explains the contact-less and contacted-base board-level broadband dielectric spectroscopy systems and their disadvantages, which were implemented collaboratively. The combined FD/TD technique was implemented and converted to a fully TD system. Both systems were measured, verified compared with the direct measurements of the vector network analyzer (VNA), then it was converted to a contact-based system along with a miniaturized onboard sensor design.

Chapter III presents a novel CMOS time-domain complex dielectric spectroscopy system using a contactless sensor, including system architecture along with the system analysis, link budget, the compact near-field contactless sensing unit, the complete CMOS circuit implementation of the main building blocks, and the simulation results, system integration and test setup, measure-

ment results of the prototype, sensor calibration, dielectric permittivity detection of mixtures, and discussion of the frequency synthesizer design for the self-sustained system, respectively.

In Chapter IV, a background of the dual-comb spectroscopy system prototyped system design along with the proposed on-chip sensor and the complete CMOS circuit implementation, including the simulation results, system integration, measurement results, signal processing for detection of the unknown MUTs are studied, respectively.

Finally, Chapter V concludes the dissertation and provides future potential works. The implemented system disclosed in Chapter III can be extended to a complete self-sustained dielectric spectroscopy system configuration. Moreover, the proposed dual-comb spectroscopy system disclosed in Chapter IV can be utilized as an integrated hybrid platform that might be a combination of the optical and microwave circuit architectures resulting in expanded extraordinary bandwidth, better resolution, self-sustained, high-speed measurement, and wider dynamic range and applications.

2. PULSE-BASED BOARD-LEVEL BROADBAND DIELECTRIC SPECTROSCOPY SYSTEMS

The objective of this chapter is to present collaboratively implemented board-level architectures and discuss the disadvantages of these systems for lab-on-chip applications. Both board and chip-level architectures with two main contact-less and contact-based sensing subcategories were implemented as miniaturized microwave broadband dielectric spectroscopy systems for materials' complex permittivity detection. The proposed systems were analyzed in this dissertation from board-level to chip-level; contact-less and contact-based board level systems are the motivation for chip-level system designs that are the main proposed works in this dissertation. The proposed methods were experimentally tested. The ultimate goal of the board-level implementations was to set the system specifications of the chip-level designs. Implemented three pulse-based UWB (3-10 GHz) board-level MBDS systems are presented.

2.1 Motivation for Integrated Microwave Broadband Dielectric Spectroscopy Systems

Two realizations of contactless UWB MBDS systems were implemented. The block diagram along with the photograph of the fabricated first prototyped board-level contact-less UWB MBDS system with a combined FD/TD technique is demonstrated in Fig.2.1 (a) and (b) [17]. This system is composed of a contact-less sensing unit, a UWB direct-conversion transmitter (including a mixer and a local oscillator as an upconverter, and an amplifier), and a UWB low-IF receiver (including an amplifier and a downconverter mixer). Two radiative near-field-coupled UWB Vivaldi antennas are used as the contactless sensing unit, where a removable fluidic container carrying a volume of $\sim$15 mL MUT is placed in the middle of these two Vivaldi antennas.

Due to the sampling constraints of available DACs (digital-to-analog converter) (1250 MSps), to generate the baseband (BB) pulse, five Gaussian signals with 125 MHz 3- dB bandwidth at center frequencies of 0, 100, 200, 300, and 400 MHz are combined resulting 450 MHz BW centered at 0 Hz. To be able to generate a flat spectrum and lower the power consumption, a BB signal that has

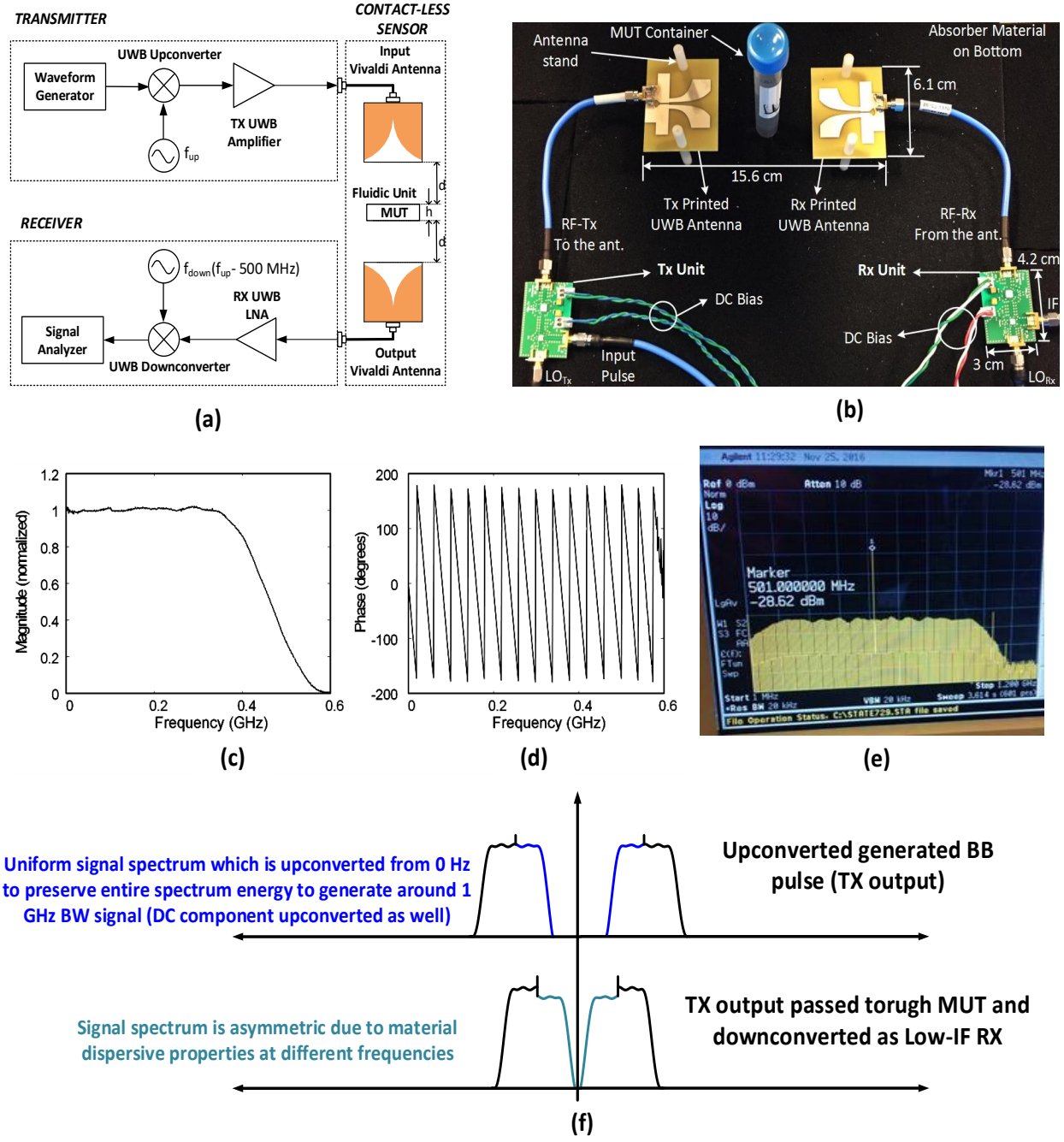

Figure 2.1: (a) Block diagram of the first proposed contact-less board-level MBDS system, (b) Photograph of the fabricated first contactless board-level MBDS spectroscopy system, (c) generated 1 GHz BW BB pulse magnitude and (d) phase, (e) measurement of the proposed pulse in FD, and (f) conceptual signal spectrum representation before and after sensing unit loaded with MUT, respectively. (Modified from [17])

a similar to half-square pulse spectrum in FD is upconverted with an LO_{TX} signal, which means that the mirror of the generated combined 450 MHz BW signal is used to generate a 10-dB BW of 1 GHz BB pulse by preserving the entire spectrum energy as depicted in Fig.2.1 (c), (d), and (f), and measurement of the proposed 1 GHz BB pulse in FD is shown in Fig.2.1 (e). However, this comes at the cost of a heterodyne architecture (low-IF receiver) instead of a homodyne one due to prevent the flicker noise effect at the receiver and self-corruption of the asymmetric received signal because of the material dispersion, which is illustrated in Fig.2.1 (f). To achieve the minimum number of measurements, for the transmitter LO_{TX}, frequencies of 3.4, 4.2, 5, 5.8, 6.6, 7.4, 8.2, 9, 9.8 GHz, while for the receiver LO_{RX}, frequencies of f_{LOTX}-500 MHz are used.

The second implemented contactless system is comprised of an onboard miniaturized picosecond pulse generator, the same UWB direct-conversion transmitter with the first one, and a high-speed oscilloscope as a receiver. In contrast, the system utilizes pure TD measurement technique. A removable fluidic Quartz glass container carrying a volume of $\sim$5 mL MUT is placed in the middle of these two Vivaldi antennas. Fig.2.2 (a) and (b) present the block diagram and prototyped system test setup of this system, including a step recovery diode (SRD)-based BB UWB pulse generator with a 10-dB bandwidth of 3.5 GHz, a UWB upconverter with a carrier frequency of 6.5 GHz, and a UWB amplifier to achieve a 7 GHz 10-dB BW as the input of the sensing unit [18]. The onboard BB pulse generator uses a similar approach to the first system. To generate a single-carrier UWB pulse covering the entire 3-10 GHz BW, the output of the SRD diode with a 0 Hz carrier is upconverted with a LO=6.5 GHz while preserving both sides of the spectrum energy, which has high ripples within 10 dB BW and also has some phase discrepancies. However, this improvement is at the cost of a high-speed oscilloscope as a receiver since a down-conversion cannot be utilized here to keep the entire BW=7 GHz information that carries the material dispersive characteristics; in other words, this system cannot be turned into a homodyne architecture because the asymmetric image (lower half-sideband of the spectrum) that half of the entire spectrum will overlap with the received signal higher half-sideband while only 3.5 GHz BW information can be captured which will be a combination of the entire 7 GHz BW resulting in a very high error as demonstrated in

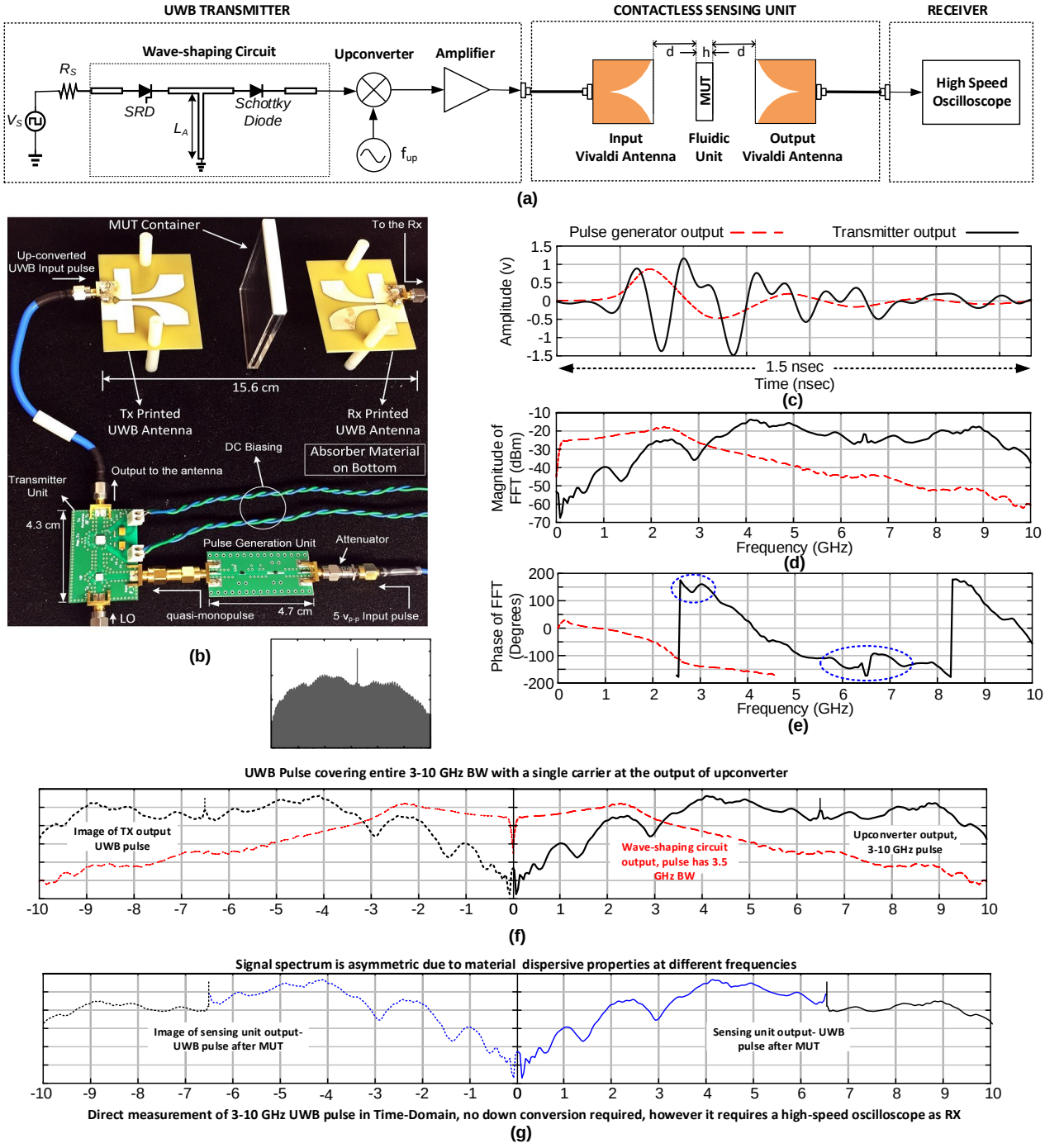

Figure 2.2: (a) Block diagram of the second proposed contact-less board-level MBDS system, (b) Photograph of the fabricated second contactless board-level MBDS spectroscopy system, (c) generated 3.5 GHz BW BB pulse (SRD diode output) and upconverted TX output pulse (7 GHz BW) in TD, (d) magnitudes of SRD diode output pulse and upconverter output pulse and (e) their phase graphs, discrepancies circled, (f) conceptual signal spectrum representation of 3.5 GHz BW and 7 GHz BW pulses in FD along with their mirror images, and (g) UWB pulse and its image representation after passing through sensing unit loaded with MUT, respectively. (Modified from [18])

Fig.2.2 (c), (d), (e), (f), and (g). Furthermore, an analog-to-digital converter (ADC) with a greater than 14 GHz BW according to the Nyquist theory is not practically feasible due to current technical limitations and very high power consumption.

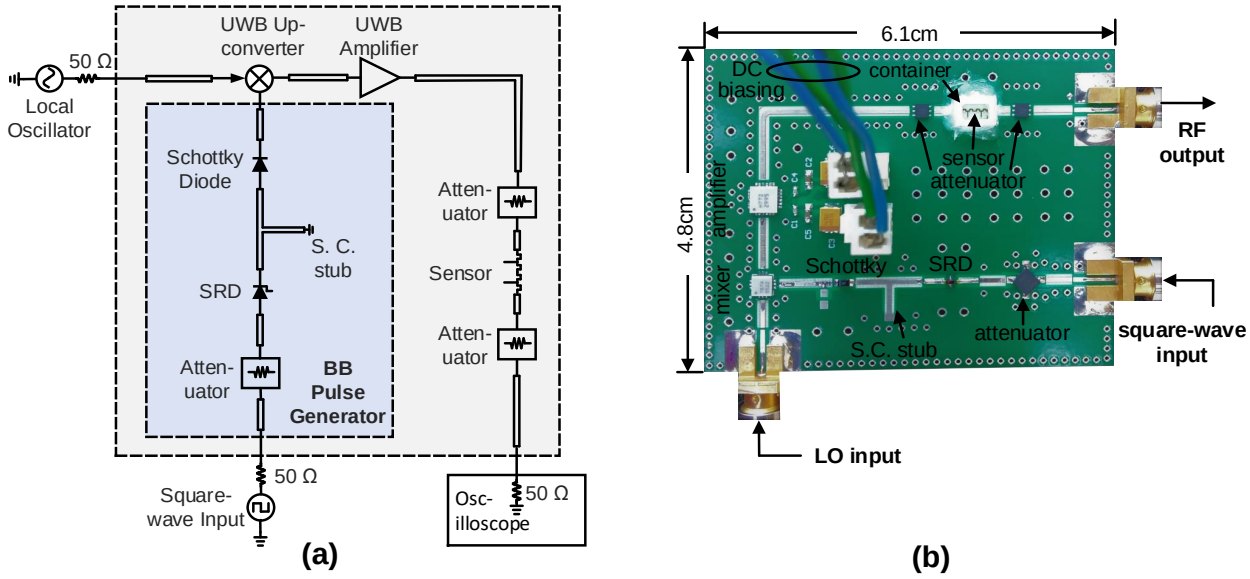

Figure 2.3: (a) Block diagram of the proposed contacted-base board-level MBDS system, and (b) Photograph of the fabricated contacted-based board-level MBDS system, respectively. (Modified from [19])

The third UWB MBDS system that operates only TD measurement technique has a similar onboard SRD-based BB pulse generator, a UWB upconverter and a UWB amplifier as a transmitter, and a high-speed oscilloscope as the receiver while it employs a contacted-base sensor depicted in Fig.2.3 (a) and Fig.2.3 (b) display the block diagram and photograph of the fabricated system [19], respectively.

The main disadvantage of these all three proposed systems is pulse generation methods that can be summarized as follows:

1-To generate a broadband BB pulse, a direct up-conversion from DC (0 Hz) will upconvert the DC component that causes a high DC peak at the center of the produced signal, which is passing

through the MUT as shown in Fig.2.1. (e) and Fig. 2.2. (f) and (g). Therefore, this method cannot be used for biomedical applications since the pulse carrying a DC component will destroy either body tissue or biomaterial.

2-Due to the onboard SRD-based pulse generator approach, the receiver will be an expensive high-speed oscilloscope that will not be a practical lab-onboard application while requiring high power consumption.

3-Although the TD measurement technique is supposed to be a faster process in nature, on the contrary, the captured 7 GHz BW signal carrying the MUT dispersive properties will have low-frequency resolution that will cause a poor signal-to-noise ratio (SNR) at the output and high error for material characterization. In consequence, to increase the output SNR and the system accuracy for material detection, an oscilloscope with a sampling rate of at least 14 Giga samples/second (Gs/s) and a high averaging ratio are required, which will lead to a longer measurement and data capturing time.

The same calibration method was utilized for both contactless and contact-based architectures for the material characterization.

The changes in phase and magnitude of transmitted pulse passing through the sensing unit are related to the complex permittivity properties of the MUT (dispersive and dissipation characteristics). Fig.2.4 demonstrates the measured output signal $\Delta\phi$-phase and ΔMag-magnitude spectrum captured in TD by a high-speed oscilloscope and transformed to the FD using FFT for different MUTs. To caliber out the nonideal effects of the sensing unit, transmitter, and receiver on the transmitted signal, a reference test (a container filled with air rather than an MUT) $\Delta\phi$-phase and ΔMag-magnitude are subtracted from the MUT $\Delta\phi$-phase and ΔMag-magnitude (($\Delta\phi$ = ϕ_{Air}-ϕ_{MUT} and ΔMag = Mag_{Air}-Mag_{MUT})). Secondly, several known reference MUTs are chosen according to the system's dynamic range. $\Delta\phi$-phase and ΔMag-magnitude of those materials are mathematically mapped to their known ϵ_r' and ϵ_r'' using MATLAB curve fitting tools that generate coefficients for all chosen reference MUTs. Finally, generated coefficients through mapping functions are used to create a database to characterize the unknown MUTs using their measured

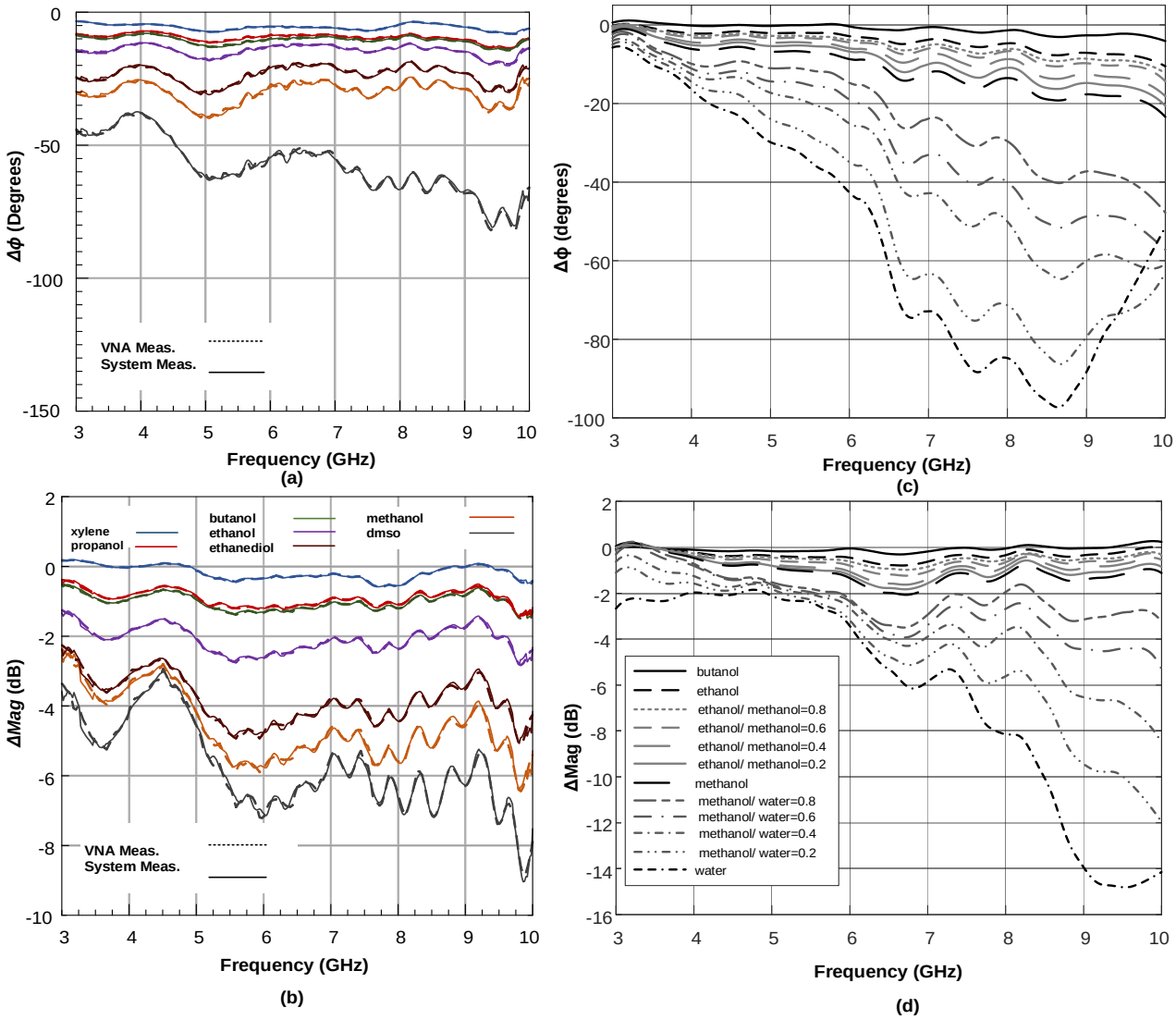

Figure 2.4: FD FFT calculated $\Delta\phi$ and ΔMag of the TD output voltage for different reference MUTs measurements: (a) and (b) second contactless board-level MBDS system, (c) and (d) contacted-based board-level MBDS system, respectively. (Adapted from [18,19])

$\Delta\phi$-phase and ΔMag-magnitude as shown in Fig.2.5.

The characterization behavior of the contactless system shows root-mean-squared error (RMSE) of 1.92% in ϵ_r' and 3.84% in ϵ_r'', and 2.47% in ϵ_r' detection of ethanol–methanol mixtures, and the contacted-based system produces RMSE of 0.2896% in ϵ_r' and RMSE of 0.3615% in ϵ_r''.

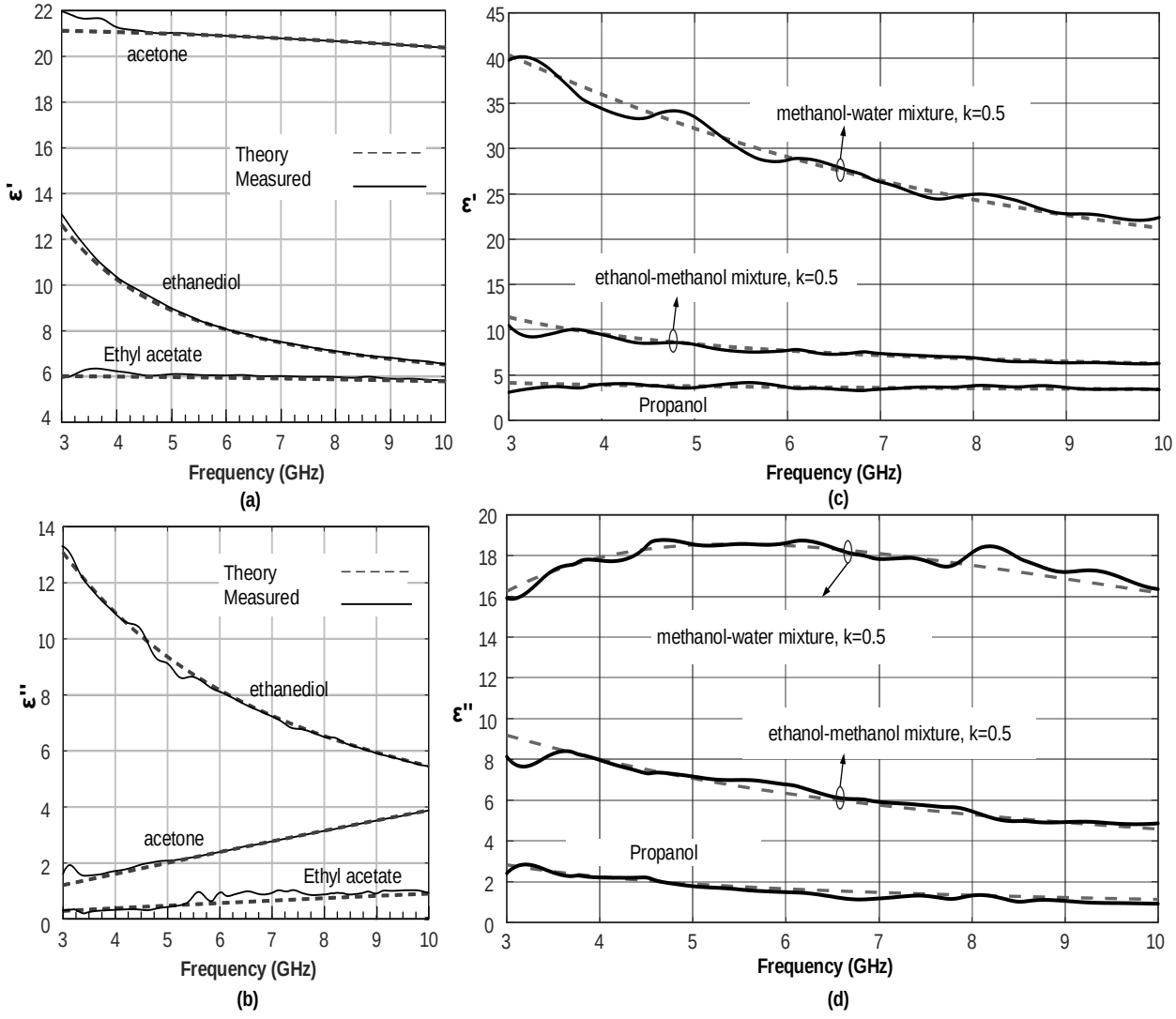

Figure 2.5: Comparison of measured and theoretical ϵ_r' and ϵ_r'' for unknown MUTs: (a) and (b) second contactless board-level MBDS system, (c) and (d) contacted-based board-level MBDS system, respectively. (Adapted from [18,19])

2.2 Contactless Sensing Unit

Free-space[1] techniques are commonly used for contact-less measurement of dielectric properties of materials [20, 21]. This technique is mainly based on using two spot-focusing lens antennas faced to each other with the material-under-test (MUT) in the middle. This method has been proven to be useful for relatively large sample volumes. However, if the sample volume of the liquid MUT is within few mm^3, then, common far-field free-space techniques, commonly used at mm-wave range [22], are impractical at microwave frequencies.

In order to achieve contact-less broad-band microwave sensing suitable for time-domain material characterization with a compact setup size, and relatively low volume of the sample, near-field sensing is proposed as a solution. Two antennas are coupled in their near-field region while the MUT is placed in between. The near-field region of each antenna has two sub-regions; reactive, and radiative (Fresnel) regions. The former is in the immediate vicinity of the antenna, where the reactive fields predominate. In this case, the electric and magnetic fields are not necessarily in phase to each other, and the angular field distribution is highly dependent on the distance and direction away from the antenna. However, in the latter case the radiating fields predominate, and electric and magnetic fields are in phase. The angular field distribution in the Fresnel region still is highly dependent upon the distance from the antenna. In the proposed setup, the distance between the two antennas (d) needs to be adjusted accurately, so that the two antennas are coupled to each other in their Fresnel regions, and therefore, have minimum effect on each other's return loss characteristics. As a result, the overall size of the setup depends on the targeted frequency range, antenna size, and its Fresnel region distance, which determines the value for d. Due to the complex electromagnetic field distribution in the Fresnel region full-wave simulations are required to finalize the overall dimensions of the setup adequately. The Fresnel region is commonly defined as follows [23]:

[1]* ©2017 IEEE. Part of this section is reprinted with permission from "A miniaturized contactless UWB microwave system for time-domain dielectric spectroscopy," R. E. Ghiri, A. P. Saghati, E. Kaya, and K. Entesari, IEEE Trans. Microw. Theory Techn., vol. 65, no. 12, pp. 5334–5344, Dec. 2017.

$$0.62\sqrt{\frac{D^3}{\lambda}} < R < \frac{2D^2}{\lambda}, \tag{2.1}$$

where, D is the largest dimension of the antenna, and λ is the operating wavelength. Each MUT perturbs the near-field electromagnetic fields around the two coupled antennas based on its specific dielectric properties, which will be translated into phase and amplitude variations of S_{21}, and could be used for material detection and characterization.

The proposed antenna type requires two main criteria. First, the system design is based on covering the complete 3-10 GHz UWB frequency range. Therefore, impedance matching within this band is needed for the sensing antennas. Second, the antenna element needs to be non-dispersive in order to be able to detect the dispersive properties of solely the MUT. Otherwise, any dispersion caused from the sensor itself results in error in reading, and makes post processing and calibration even more cumbersome. As a result, the sensing antenna has to provide UWB operation with relatively constant group-delay over the entire band. In this setting, the Vivaldi antenna is one of the best candidates due to its broad bandwidth, low cross-polarization, and constant group delay. Fig.2.6 (a) shows the utilized printed UWB Vivaldi antenna first proposed in [24]. The antenna excitation, on the back side of the substrate, is a stepped microstrip line in order to cover the UWB frequency range. Both the inner and outer edges of the top metal patches are tapered to achieve the optimized group delay and impedance matching performance as discussed in [24].

Another important factor in the proposed contact-less setup is the container used to place the liquid MUT in between the two antennas. Since the proposed setup is based on sensing in the Fresnel region in a controlled environment, the shape, dimensions, and the material of the container also require to be designed and set for all the measurement trials. At the same time, the container needs to be low-cost in order to make inexpensive repeating of the measurement for various MUTs feasible. In [17], a standard tube pipet (made from polypropylene with a diameter of 17 mm) is utilized as the liquid container between the two antennas. Using this container, roughly 15 ml of the sample is required. Moreover, this container has a cylindrical shape, which is not optimized for having minimum diffraction from the edges of the container due to discontinuity in the dielec-

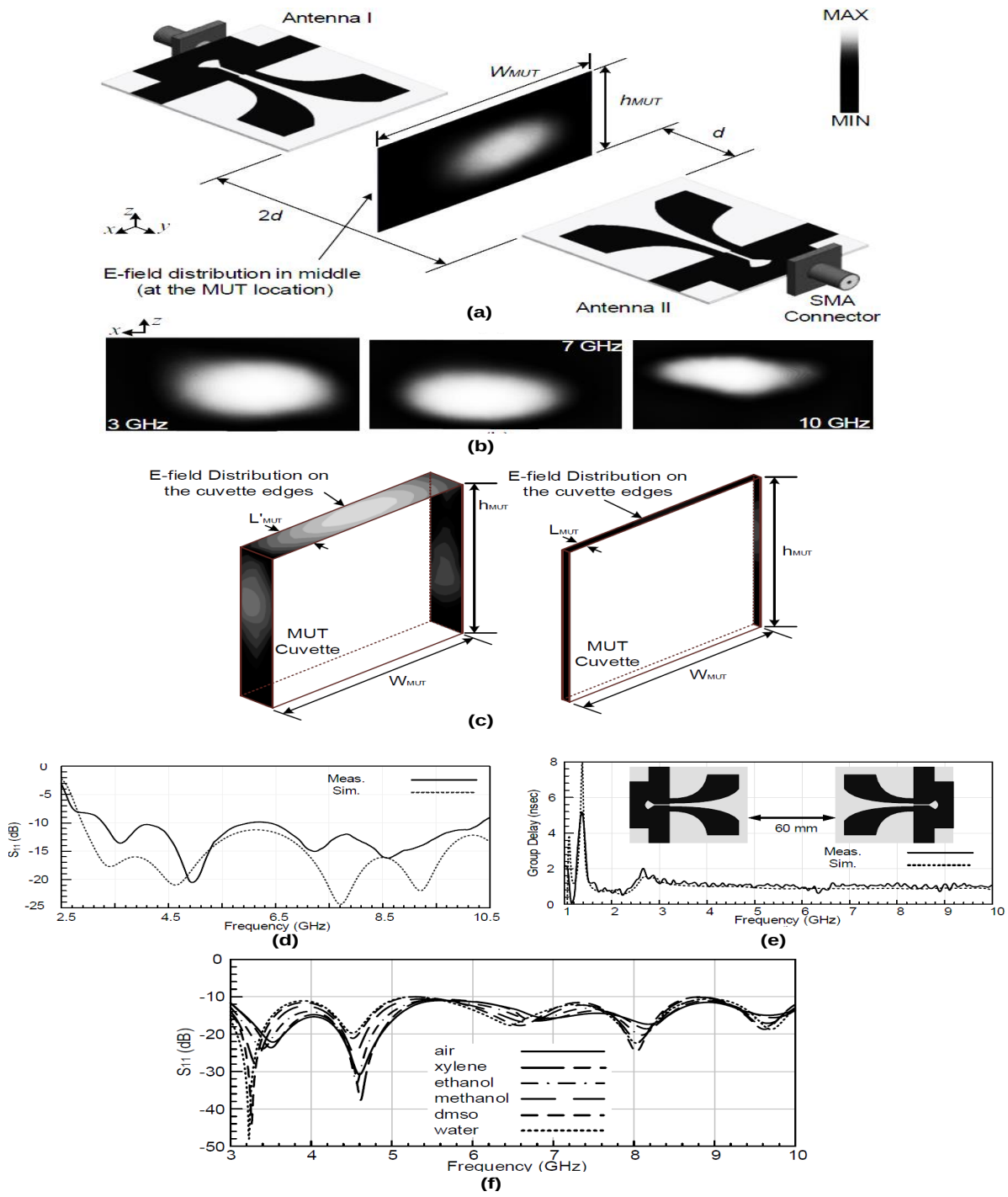

Figure 2.6: (a) Two near-field coupled antennas faced each other, and the E-field distribution is shown in the middle and at the position of MUT at f = 3 GHz, (b) E-field distribution in a plane in between the two antennas where the MUT is located at different frequencies. The design values are W_{MUT}= h_{MUT} = 51 mm, and d = 30 mm, (c) E-field distribution on the edges of the MUT cuvette at 3 GHz, Fabricated UWB Vivaldi antennas simulated and measured return loss (d) and (e) group delay of the setup when the distance between the two antennas is 2d = 60 mm, and (f) simulated S11 of the setup when different MUTs are placed in between two antennas, respectively. (Adapted from [18])

tric constant. However, the required volume of the sample can be reduced, and the accuracy of the sensor improves if the shape and dimensions of the container are custom designed. In order to better show the importance of the container shape, and dimensions, the E-field distribution is plotted in between the two antennas, and where the MUT is placed, and shown in Fig.2.6 (a) and (b) at different frequencies. As can be seen, the container requires to cover the area where the E-field distribution is concentrated. Otherwise, considerable amount of energy will be diffracted from the edges of the MUT and container, which reduces the accuracy of the sensor specially for MUTs with large dielectric constants, such as dmso (ϵ' = 46.4 at 3 GHz), and water (ϵ' = 76.4 at 3.41 GHz).

This cuvette is made of Quartz glass with a dielectric constant of 3.78 and a loss tangent of below 0.0004, which is roughly independent of the frequency over the desired UWB range. The thickness of the glass is chosen to be 2 mm, which is less than λ/10 at 10 GHz, to avoid multiple reflections and electromagnetic bouncing between the glass slabs. The width and height of the cuvette are chosen to cover the main concentration of the E-field distribution in the middle plane, as was shown in Fig.2.6 (a) at different frequencies. As a result, W_{MUT}, and h_{MUT} are both chosen 51 mm. On the other hand, the length of the cuvette needs to be lower than λ/10 at the upper limit (10 GHz) in order to avoid multiple reflection, and electromagnetic bouncing inside the MUT. A lower length for the cuvette also reduces the required volume of the MUT. Moreover, a length, L_{MUT}, smaller than λ/10 at 10 GHz results in negligible diffraction from the edges of the MUT, while having a larger L_{MUT} can result in significant electromagnetic diffraction from the edges. This is better shown in Fig.2.6. (c), where the E-field distribution is plotted on the edges of the cuvette at 3 GHz for two different values of L_{MUT}. As can be seen, when the length is as large as 8.5 mm, which is $\sim 0.28\lambda$ at 10 GHz, there are E-field maximums on each edge of the cuvette, while reducing the length to 2 mm ($\sim 0.06\lambda$ at 10 GHz) would result in negligible E-field concentration on the edges. As a result, the length of the cuvette, L_{MUT}, is chosen to be 2 mm $<\lambda/10$ at 10 GHz, in order to (1) reduce the required volume of the sample liquid MUT, (2) avoid Electromagnetic bouncing and multiple reflection issues, and (3) significantly reduce the

diffraction from the edges of the cuvette. In this case, the required volume is $\sim$ 5 ml, which is $\sim$ 67% less than the cylindrical tube used in [17].

The antenna is fabricated based on using common single-layer FR-4 substrate with a dielectric constant of 4.4, and a thickness of 0.8 mm. Fig.2.6 (d) shows the simulated and measured return losses of the designed Vivaldi antenna, which covers the interested bandwidth of 3-10 GHz. In order to extract the group delay of the utilized Vivaldi antenna in the proposed setup, first the distance between the two antennas (d) needs to be determined according to (2.1). The largest dimension of the utilized antenna is D = 51.4 mm, and the wavelength of the interested frequency range covers 3-10 cm. According to (2.1), and performing fine tuning simulations using Ansys High Frequency Structure Simulator (HFSS), the distance between the two antennas is chosen, $2d$ = 60 mm, in order to couple the two antennas in their Fresnel regions while the mutual coupling and the MUT have negligible effects on the return loss characteristics of the two antennas. In this setting, the simulated and measured group delay is extracted and shown in Fig.2.6 (e). The slight differences between the simulation and measurement is due to the tolerances between the SMA connector model in HFSS, and the actual SMA connector used in measurement. In order to better show that the two near-field coupled antennas remain matched to 50 Ω regardless of the MUT in between, the simulated S_{11} response is plotted in Fig.2.6 (f) when different MUTs are placed in middle. Debye-based relaxation models of MUTs are imported into HFSS in order to take into account the frequency dependence of the dielectric constants in full-wave simulations. As can be seen, the antenna element shows return losses better than 10 dB over the entire bandwidth for all the materials with a broad range of dielectric constants.

2.3 Contacted-based Sensing Unit

Response[2] of an MUT to an external electric field depends on the relative permittivity of the MUT [25]. Therefore, when an MUT is placed on top of a microstrip transmission line, the electric field over the signal trace will be affected by the MUT [26], which is measured as a variation in

[2*]

phase and magnitude of the voltage signal. A microstrip open stub exposed to an MUT, which can be modeled as a microstrip line loaded by fringing capacitance C_f and resistance R_f. C_f and R_f vary by changing the MUT. With different MUTs, such as air, ethanol, methanol, and water, the impedance Z_{sh} seen at the beginning of the stub changes. C_f and R_f are determined by equalizing Z_{sh}. Here the shunt stub is in direct contact with the MUT, hence, it senses variations in both ϵ' and ϵ'' of the MUT.

To detect the phase and magnitude variations of the open stub impedance (Z_{sh}) as phase and magnitude variations of a transmitted signal, and develop a wide band sensing structure, the microstrip stub is located between two series inductors L. The combination of shunt stub and inductors is considered as a sensing cell with two ports. The value of inductor in cell should be designed to provide enough phase and magnitude sensitivity for detecting different MUTs and to meet matching condition. Having Z_{sh}, the Z-parameters of the single cell will be:

$$Z_{11} = Z_{22} = j\omega L + Z_{sh}, \tag{2.2}$$

$$Z_{12} = Z_{21} = Z_{sh}. \tag{2.3}$$

From these Z-parameters, the S-parameters, and then T-parameters of the single cell are calculated [27]. Because cascading multiple cells increases S_{21} phase variations, sensors with two and three cells are created by multiplication of the T-matrix. Then, T-parameters are converted back to S-parameters to study the effect of L on the behavior of two- and three-stage sensors. The sensitivity of the sensors are measured based on $\Delta\phi = \phi_{MUT} - \phi_{air}$ and $\Delta Mag = Mag_{MUT} - Mag_{air}$ parameters, where ϕ and Mag are phase and magnitude (in dB) of S_{21}, respectively, and subscripts indicate the name of MUT used in testing. To investigate the sensitivity of the sensor, minimum $\Delta\phi$ and $|\Delta Mag|$ values versus L over the frequency range of 3-10GHz are evaluated. Larger value of L enhances phase sensitivity, but in terms of magnitude sensitivity, values of L larger than 1.4nH, will degrade $min|\Delta Mag|$ for water. This is due to the creation of nulls in S_{11} response in the frequency band of interest, which maximizes the transmission coefficient, S_{21}, showing small mag-

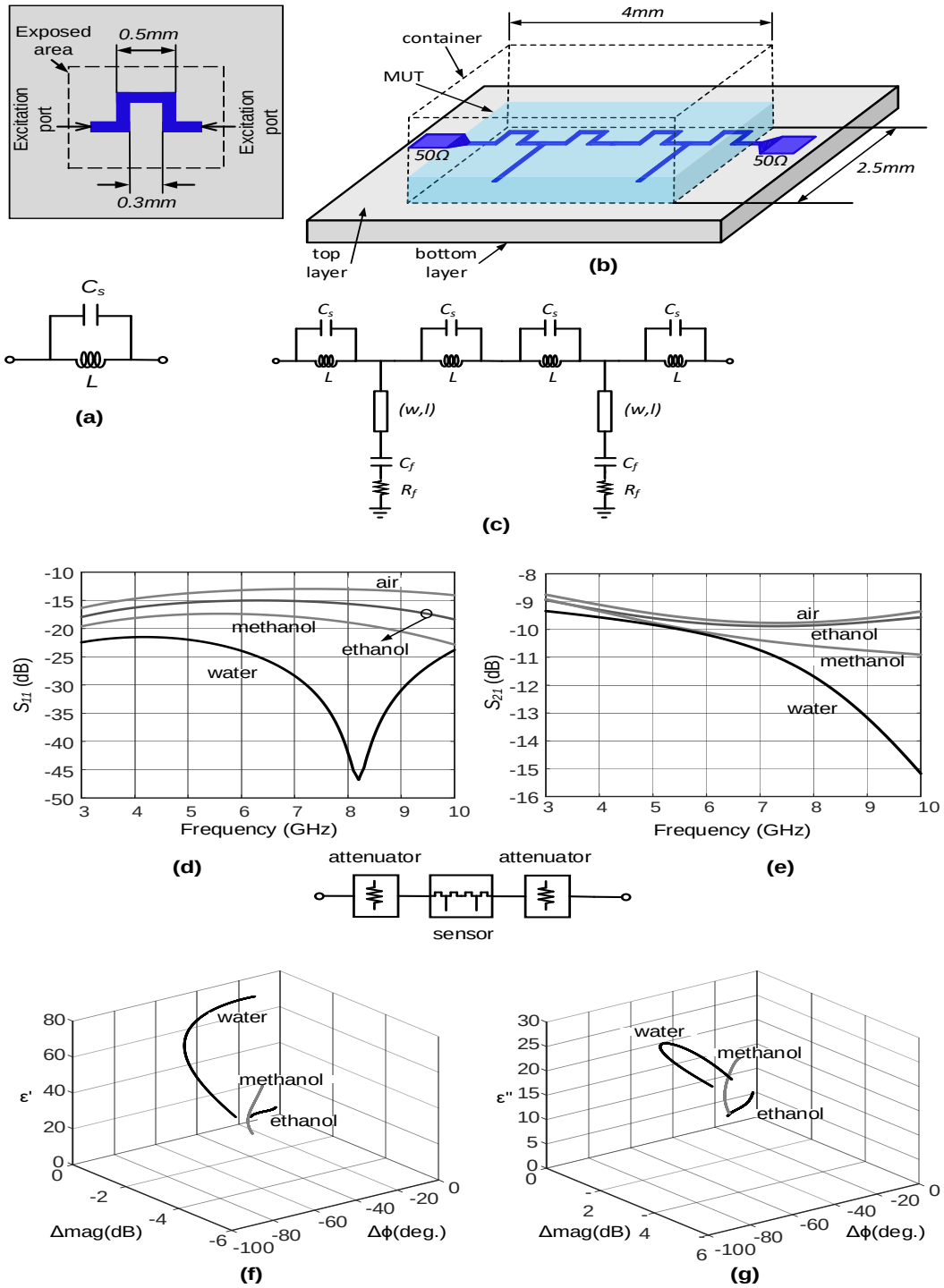

Figure 2.7: (a) Design of inductor: layout in Sonnet and its equivalent circuit, (b) 3-D layout of sensor with two stages and (c) equivalent circuit model, (d) impedance matching of the sensor to 50 Ω by adding attenuators, schematic of the sensor with two attenuators, S_{11} and (e) S_{21} simulated, (f) 3D response of the sensor ϵ', and (g) ϵ'', respectively. (Adapted from [19])

nitude variations for different MUTs. Similar phenomenon happens for ethanol and methanol, but at frequencies larger than 10GHz. Furthermore, increasing the number of stages from two to three will improve phase sensitivity, but it will further limit the range of L. Consequently, the value of L is decided to be in the range of 0.8nH to 1nH, and two cells are chosen which also suggests smaller space for sensor and lower volume of MUT. With two cells, $\Delta\phi_{ethanol} = 2.4°$, $\Delta\phi_{methanol} = 6.2°$, $\Delta\phi_{water} = 13°$, and $\Delta Mag_{ethanol} = 0.2dB$, $\Delta Mag_{methanol} = 0.5dB$, $\Delta Mag_{water} = 0.9dB$ are the minimum values to be measured. For a sensor with only one cell, the minimum $\Delta\phi$ and ΔMag values change in smaller ranges requiring a receiver with higher sensitivity for their detection.

Fig.2.7 (a) shows the designed inductor in Sonnet, its equivalent circuit model, and the effect of MUT on the value of inductor. The resultant inductance L_a can be considered as a parallel combination of constant L and C_s while the value of C_s changes with MUT. L_a is a frequency dependent inductance which is related to L and C_s according to the following equation:

$$\begin{aligned} j\omega L_a &= (j\omega L)||(\frac{1}{j\omega C_s}), \\ L_a &= \frac{L}{1-\omega^2 L C_s}. \end{aligned} \tag{2.4}$$

which proves L_a increases with the frequency.

The length of shunt stub, l, also affects the properties of the cell. Using L_a values designed in Sonnet and the R_f and C_f values for each MUT , the effect of different lengths of shunt stub on sensitivity can be studied. Assuming width of transmission line w to be minimum 0.1mm on RO4350B substrate, the characteristic impedance Z_0 of transmission line will be 117Ω at 10GHz. With Z_L=R_f+$1/(j\omega C_f)$, Z_{sh} can be calculated as a function of l [27]:

$$Z_{sh} = Z_0 \frac{Z_L + jZ_0 tan(\beta l)}{Z_0 + jZ_L tan(\beta l)}, \tag{2.5}$$

where β =2π/λ is the phase constant, while $\lambda = \lambda_0 / \sqrt{\epsilon_{eff}}$ and ϵ_{eff} is calculated to be 2.461 at 10GHz. Although larger value of l increases $\Delta\phi$, but large l limits the bandwidth and transmission of signal. As the result, a relatively small l=0.9mm is selected to achieve acceptable sensitivity.

The final layout of the sensor with its complete electrical model are presented in Fig.2.7 (b) and (c).

Although the sensor is sensitive to both ϵ' and ϵ'' of MUTs, the matching condition is not satisfied over 3-10 GHz. To improve S_{11}, constant attenuators are added to the input and output of sensing structure as shown in Fig.2.7 (d) and (e). According to Fig.2.7 (d), after adding two 4-dB attenuators at the input and output of the sensor, S_{11} for different MUTs is always less than -13 dB. Fig.2.7 (e) shows simulated S_{21} which cannot be larger than -8dB because of attenuators.

$\Delta\phi$ and ΔMag are functions of both ϵ' and ϵ'', simultaneously. The theoretical values of ϵ' and ϵ'' versus simulated $\Delta\phi$ and ΔMag are shown in Fig.2.7 (f) and (g) for three different MUTs. The frequency variable has been excluded from Fig.2.7 (f) and (g), while all values change from 3-10 GHz.

3. AN ULTRA WIDE-BAND CMOS TIME DOMAIN COMPLEX DIELECTRIC SPECTROSCOPY SYSTEM USING A CONTACT-LESS SENSOR

This chapter[1][2] aims to present proposed the first chip-level UWB integrated microwave dielectric spectroscopy system in TD. The system employs a contactless sensing application with a 1 GHz BW BB on-chip pulse generator unit. Due to today's CMOS existing technology limitations, it utilizes nine subcarriers to cover 3-10 GHz BW. According to the Nyquist theory, it is not feasible to design an ADC with a BW of at least 14 GHz BW to cover the desired frequency span as a single BB pulse. Therefore, to take advantage of the TD measurement technique, the targeted 7 GHz BW is divided into nine subcarriers to make a fully integrated system possible.

To the best of the author's knowledge, according to all reported on-chip/on-board frequency and time domain spectroscopy techniques, there is no work reported in the literature on homodyne transceiver architecture.

3.1 Introduction

The dielectric permittivity of many materials has a solely unique frequency response at RF/microwave frequencies. Taking advantage of this property, microwave broadband dielectric spectroscopy (MBDS), which is a nondestructive, cost-effective and real-time characterization procedure, is a promising technique to determine the complex permittivity of materials for a wide range of applications including chemical/biological sensing, disease diagnosis (such as distinguishing breast cancer cells, monitoring blood glucose concentration, and identifying antibodies, etc.), biothreat detection, oil exploration and processing, agriculture and food quality/safety, and drug development in the pharmaceutical industry [28].

Traditional MBDS systems utilize either frequency domain (FD) or time domain (TD) complex

[1]* ©2019 IEEE. Parts of this section, Part of this section is reprinted with permission from "A 3–10-GHz CMOS Time-Domain Complex Dielectric Spectroscopy System Using a Contactless Sensor," E. Kaya, A. P. Saghati, and K. Entesari, IEEE Trans. Microw. Theory Techn., vol. 67, no. 12, pp. 5202-5217, Dec. 2019.

[2]* ©2019 IEEE. Parts of this section, Part of this section is reprinted with permission from "A CMOS Time Domain Microwave Broadband Dielectric Spectroscopy System with a Contact-less Sensor for Liquid Chemical Detection," E. Kaya, A. P. Saghati, and K. Entesari, IEEE MTT-S Int. Microw. Symp. Dig., pp. 800-803, Jun. 2019.

dielectric permittivity measurement and detection methods. FD spectroscopy (FDS) techniques that employ waveguide resonant method work with a very narrow microwave frequency range [8, 9], while FDS coaxial-line techniques are able to perform up to 20 GHz [29]. Traditional microwave FDS systems using a single-tone excitation signal to characterize the material under test (MUT) require an expensive, bulky external Vector Network Analyzer (VNA). On the other hand, although the traditional microwave TD spectroscopy (TDS) systems perform over a very wide band frequency range with high accuracy, to capture the signal, an expensive bulky high-speed digital oscilloscope is necessary [14]. In essence, all the traditional MBDS systems are constrained by high power and cost, the large size of the measurement setup, and exaggerated volume of the MUT.

Conventional board-level miniaturized MBDS systems have been mostly implemented with FD technique. The MUT is in direct-contact with their sensing element and they often require bulky and expensive signal generators for broadband operation [30]. Recently, a board-level contact-less UWB combined TD/FD spectroscopy system is reported in [31], which uses multiple sub-bands to cover the entire frequency range with the volume of MUT $\sim$15 ml. Also, a contact-less UWB TDS system is presented in [18], which utilizes a custom cuvette with the volume of MUT $\sim$5 ml and a picosecond pulse generator covering the overall frequency span, respectively. The TD/FD one requires two different LO inputs for up/down converters, while a high speed-bulky oscilloscope is needed as the receiver for the TD one.

Due to recent advances in CMOS technology, the integrated MBDS systems on silicon are demanded owing to significant cost reduction, smaller size, better system integration, enormous processing, and higher throughput. All the reported integrated MBDS systems are in direct contact with either an on-chip or off-chip sensing unit utilizing only FD techniques. They can be grouped into either the RF receiver-based architecture [32, 33], or voltage-controlled oscillator (VCO)/phase-locked loop (PLL)-based architecture [34, 35]. The RF receiver-based architecture is capable of evaluating both real and imaginary parts of the permittivity within a wide frequency range by capturing the amplitude and phase of the single-tone excitation signal. However, it re-

quires an additional frequency synthesizer for signal generation that causes high power consumption. Moreover, the integrated RF receiver MBDS systems with heterodyne or homodyne-receiver architecture either depend upon two different frequency synthesizers [33] or have the issue of flicker noise and dc-offset [32], respectively. RF receiver MBDS systems also suffer from the limited dynamic range of the voltage-mode analog to digital converter (ADC). Contrarily, the VCO (LC-VCO or ring-VCO)/PLL-based architecture conserves power by combining the excitation and sensing functions into a single VCO and can use a highly efficient, high-resolution time-mode ADC that may be simply implemented as a digital counter [36], [37]. However, employing low phase noise LC-VCOs to improve the sensitivity, limits the tuning range of this approach. Furthermore, since ring-VCO has poor phase noise, it results in relatively low accuracy [38]. To address limited tuning range of LC-VCOs, the one in [39] employs a wideband low-power low-noise LC-digitally controlled oscillator (DCO) with three dual-band VCO cores , which uses large chip area and in terms of the complex permittivity detection is still limited to 1-3.8 GHz range with 5% permittivity error. Differently, the one described in the [40] consists of a PLL, and a wideband VCO that can only identify the dielectric permittivity of the MUT with 3 GHz BW (5-8 GHz) and requires quadrature-VCO (QVCO) to generate the LO frequencies which needs calibration to prevent the high-frequency quadrature phase/magnitude mismatches.

This project presents a time-domain MBDS system using a contact-less sensor maintaining the near-field excitation and detection similar to [18], and a novel integrated silicon platform to distinguish both $\epsilon_r'(w)$ and $\epsilon_r''(w)$ accurately over the 3-10 GHz frequency range. By taking advantage of the benefits of TDS systems, the bandwidth of the entire system is widened. Comparing the proposed system with the two types of reported FD architecture, the proposed MBDS system as a homodyne RF transceiver does not require two different LO signals for up/down conversion making the frequency synthesizer design much easier when compared to heterodyne receiver-based FD architectures [33]. Also, compared to homodyne receiver-based FD architectures [32], the proposed system eliminates the effect of flicker noise and dc-offset errors by defining a dc-free baseband signal improving sensitivity of the system. While the VCO/PLL-based ones have the

advantage of self-sustained detection, the proposed system with an on-chip pulse generator, can be turned into a self-sustained system by implementing an on-chip frequency synthesizer. Furthermore, the proposed system avoids the need for a VCO alleviating phase noise and spurs effects of the frequency detector while it provides a wider frequency range for characterizing both real and imaginary parts of the complex permittivity. Finally, because of the contact-less sensor, the fluidic module is easily replaceable instead of replacing the entire chip or the sensing element which is more cost effective, makes the experiments safer and protects the overall system against the material leakages although the proposed system can be easily converted to a contact-based architecture as described in [41], [19].

The author first introduced an integrated CMOS MBDS system in [42] which can measure both ϵ_r' and ϵ_r'' of different liquid chemicals with 7 GHz BW. In this paper, a more in-depth analysis on the MBDS system design, circuit implementation of different building blocks, system performance with a wide variety of MUTs, and more insight into the calibration and characterization of the complex permittivity are provided.

The operation of the entire MBDS system is verified by a prototype fabricated using 65-nm CMOS technology. The chapter is organized as follow. Section 3.2 presents the proposed system architecture along with the system analysis, link budget, and the compact near-field contact-less sensing unit. The complete CMOS circuit implementation of the main building blocks and the simulation results are explained in Section 3.3, while the system integration and test setup are described in Section 3.4. Section 3.5 presents and discusses the measurement results of the prototype, sensor calibration, and dielectric permittivity detection of mixtures, respectively. Finally, Section 3.6 describes the future works for the possible fully integrated, self-sustained contactless MBDS system.

3.2 Contact-less Microwave Broadband Dielectric Spectroscopy Platform Architecture and System Analysis

This section first discusses the proposed system architecture along with the frequency planning. The contact-less sensor with the shape and size of the MUT cuvette is then described. Finally,

system analysis is presented.

3.2.1 The Proposed MBDS Architecture and Frequency Planning:

The proposed MBDS system targets the following main three goals:

1) Generation of an on-chip excitation pulse with a 1-GHz bandwidth and a uniformly distributed broadband spectral energy in the desired 100-900-MHz frequency span, and transmission of the generated signal by preserving the spectral flatness through the entire system to characterize MUT's magnitude spectrum, hence its dissipation factor (ϵ_r'').

2) Implementation of a dc-free direct signal up-/downconversion with a single LO frequency to provide flexibility in the frequency synthesizer design and correlate TX/RX LO phase noises, and utilization of a single-sideband (SSB) mixer for signal upconversion to avoid the corruption of the asymmetric signal spectrum at the RX baseband output. This is due to the fact that both the sides of the RF carrier do not provide exactly the same information due to the dispersive characteristics of the materials.

3) Provision of constant group delays (GDs) (GD= $-d\varphi/dw$) to have a linear phase change through the entire system to obtain the accurate dispersive property of MUT (ϵ_r'), from the phase of the captured output signal.

The proposed integrated TD MBDS system with an off-chip contact-less sensing unit is composed of four essential parts: 1) a baseband pulse generation unit, 2) a UWB transmitter (TX) unit, 3) a UWB receiver (RX) unit, and 4) a high-frequency quadrature LO generator/distributor unit. The block diagram of the proposed contactless MBDS system is shown in Fig. 3.1.

In the baseband pulse generation unit, the low-frequency differential ramp input is externally provided to differential baseband Gaussian pulse generator, and then, Gaussian pulses are coupled to five baseband mixers which their outputs are added through an analog adder to generate the proposed wideband excitation pulse, while a set of true single-phase-clock (TSPC) frequency dividers with an external 9.6 GHz reference input frequency are used to generate the LO inputs for the baseband mixers. By merging multiple frequency-shifted Gaussian pulses, a UWB baseband signal with 1 GHz bandwidth (500 MHz center frequency) is generated to improve the material

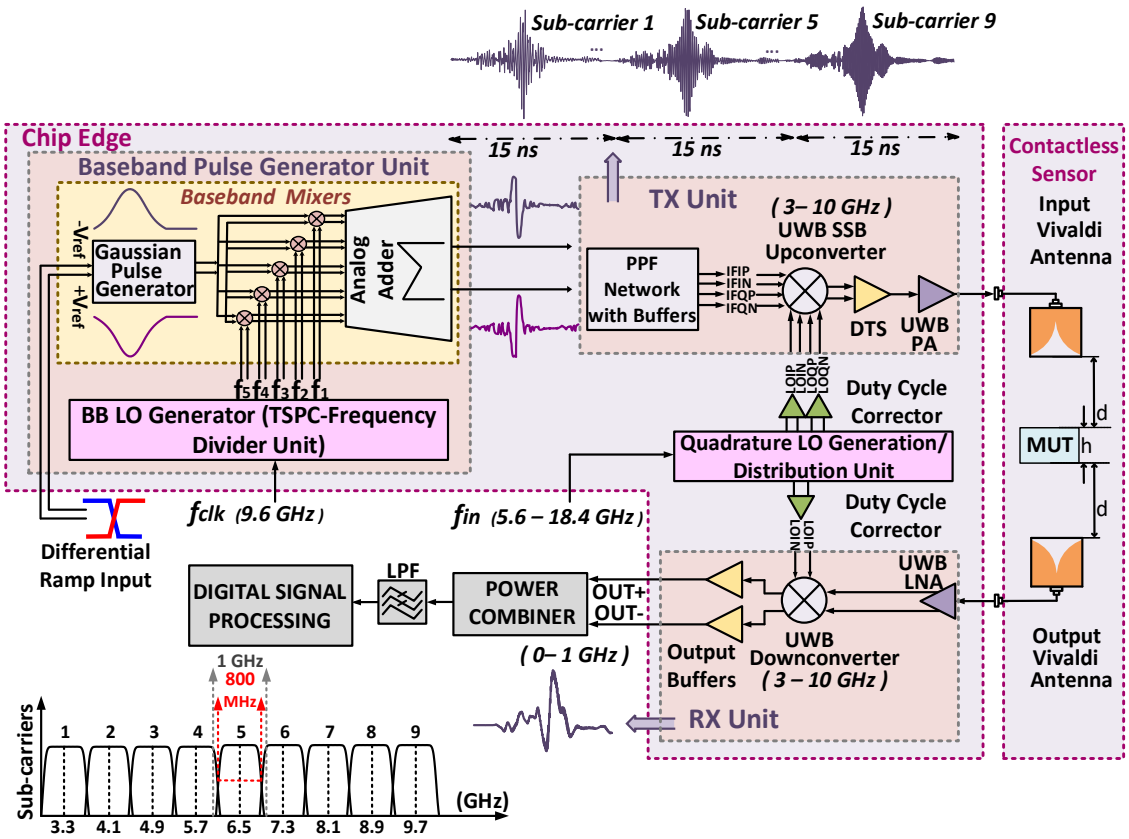

Figure 3.1: Block diagram of the proposed contact-less TD MBDS system with frequency planning. (Reprinted from [7])

detection accuracy. Contrarily, in the discrete implementation reported in [31], the added five Gaussian pulses were centered at dc. Hence, through up/down conversion process, the receiver output signal SNR was degraded due to flicker noise component. In addition, two different LO frequencies were required for up/downconversion procedure.

The TX includes a poly-phase filter (PPF) network with output buffers to generate quadrature IF inputs, a broadband SSB mixer for upconversion, a differential-to-single ended (DTS) output buffer, and a broadband (3-10 GHz) power amplifier (PA) with $50\ \Omega$ matched output impedance. The generated broadband excitation signal is directly upconverted to nine microwave subbands within 3-10 GHz frequency range one at a time. Each microwave subband is then passed through the UWB contactless sensing element by placing the MUT in between two UWB Vivaldi antennas coupled in their Fresnel region [18]. The electric field inside the MUT changes depending on the

complex permittivity of the material and provides variations on the phase and magnitude of the signal exposed to the MUT.

The front-end UWB RX is composes of a 3-10 GHz low-noise amplifier (LNA) with $50\ \Omega$ matched input impedance and a UWB direct downconverter with baseband output buffers. The captured signal is directly downconverted to the baseband centered at 500 MHz with 1 GHz bandwidth through the RX. Afterward, an off-chip low-pass filter eliminates the unwanted high frequencies. By realizing integrated TX and RX units with a constant group delay and flat magnitude along with the constant group delay contact-less sensor for the overall desired 7 GHz frequency band, the microwave signal passing through the MUT inside the fluidic unit represents only the loss and the dispersive properties of the material related to its dielectric properties.

The quadrature LO generator/distributor unit provides the required LO frequencies as differential I/Q signals to the upconverter and same differential I signal to downconverter by dividing the external (5.6 GHz to 18.4 GHz) input LO frequency using on-chip frequecny dividers along with a chain of CMOS buffers for 50% duty cycle correction.

In this work, the time domain output of the receiver is captured using DSA91304A infiniium oscilloscope, and then, data are imported to MATLAB for FFT calculation and finding the complex permittivity of the MUT, $\epsilon_r^* = \epsilon_r' - j\epsilon_r''$. It is also possible to have an on-chip analog-to-digital converter (ADC) with $3 \sim 4$ GSample/sec sampling rate with $8 \sim 11$-bit resolution to avoid using the bulky oscilloscope [43], [44], but this part was not implemented in the current chip.

As discussed earlier, one of the challenges in the proposed MBDS system is the generation of a wideband on-chip excitation signal as the baseband pulse. Although generation of stepped-frequency continuous-wave (SFCW) signals is possible at microwave range [45], however; it has a narrow bandwidth (lower than 500 MHz) and requires many measurements over a wide range of frequencies. Furthermore, frequency-modulated continuous-wave (FMCW) signals are commonly used in radars; however, they also suffer from a narrow bandwidth [46]. Most of the UWB systems use a Gaussian pulse or its derivatives for that purpose [47]. For the proposed MBDS system, a single Gaussian signal has low amplitude at the lower and higher frequencies of its spectrum

when it is upconverted to microwave frequencies and is not suitable to detect the effect of the MUT on the magnitude of the signal as shown in Fig. 3.2 (a) and (b). It is possible to generate a UWB signal with Gaussian derivatives covering the UWB frequency span [48]. The spectrum of a Gaussian derivative pulse has also wide tails that cause signal energy wasted in the frequency regions without interest as shown in Fig. 3.2 (c) and (d). To be able to use Gaussian pulse and its derivative as UWB baseband pulses, instead of direct conversion architecture, a heterodyne architecture has to be employed (different LO signals for TX/RX units are required). Otherwise, a UWB image rejection circuit is required for the homodyne architecture to prevent destructive effect of the dispersive material on the amplitude of the downconverted signal at the RX baseband, which might not be feasible with available CMOS circuit topologies. Furthermore, if the excitation signal is very wideband, LO and IF frequencies will be very close to each other, then the LO leakage will not be filtered out, and hence, it will interfere with the RX output degrading the accuracy of the measurement.

To overcome the above challenges, a signal that has a near rectangular spectrum in the frequency domain with a 1 GHz bandwidth is proposed. One way to obtain such an excitation signal is to use a sinc function as depicted in Fig. 3.2 (a) and (b). However, it has a dc component [48]. Here, a new excitation signal is generated by adding five upconverted Gaussian pulses centered at 160-320-480-640 and 800 MHz to generate a signal with minimized ripples and avoid the dc component to eliminate the flicker noise (1/f) and dc-offset effects resulting in improved RX SNR. The spectrum of the Gaussian function is also Gaussian without any side lobes. On the other hand, square-wave LO signals used to upconvert the five Gaussian pulses have odd harmonic frequency components ($3f_{LO}$, $5f_{LO}$, $7f_{LO}$, ...) besides the fundamental frequency f_{LO}. By equally spacing the Gaussian subcarriers (each has a 240 MHz 10-dB BW) with the same spacing of 160 MHz, the harmonic spurs which can cause the intercarrier interference are moved away from the desired frequency band (except the $3f_{LO}$ harmonic for the first subcarrier with negligible effect on the spectrum flatness) resulting in a uniform spectrum.

Subsequently, a flat frequency spectrum with the near perpendicular drop-down energy outside

the unwanted bandwidth and linear phase change within the desired frequency band is achieved. To demonstrate the feasibility of the proposed baseband signal, five Gaussian pulses with the target specs are added in Advanced Design Systems (ADS) as shown in Fig. 3.3. The obtained signal has similar characteristic properties of haversinc function ($sin^2(\omega t)/\omega t$) as shown in Fig. 3.2 (c) and (d) commonly preferred in implantable/wearable biological systems due to the absence of the dc component [48].

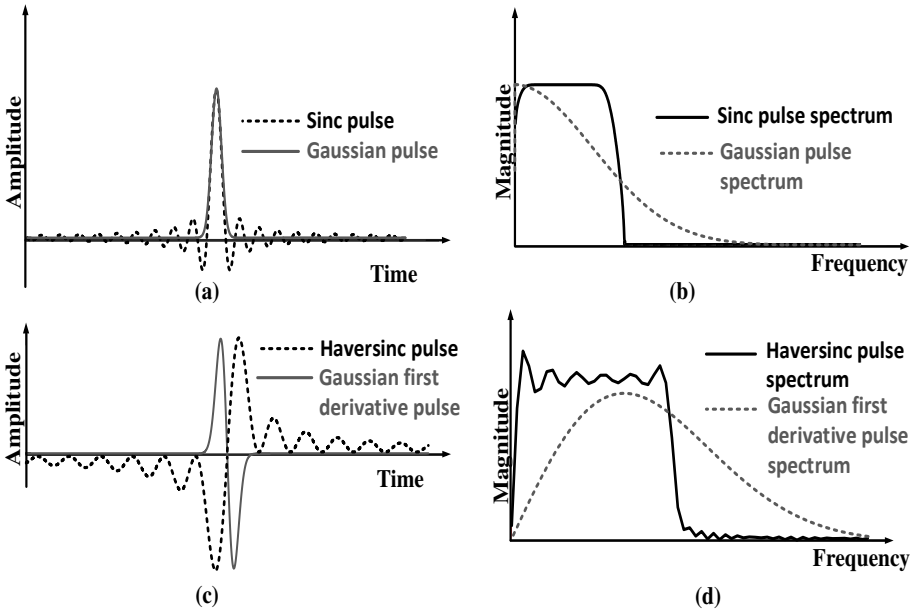

Figure 3.2: Comparison of the Gaussian (a,b), first derivative of the Gaussian (c,d), sinc (a,b) and haversinc (c,d) as functions in time and frequency domains, respectively. (Reprinted from [7])

The microwave frequency span of 3–10 GHz is divided into nine subbands with LO frequencies of 2.8, 3.6, 4.4, 5.2, 6, 6.8, 7.6, 8.4, and 9.2 GHz as shown in Fig. 3.1. Each subband's center frequency is formulated as follows;

$$f_c = (2500 + 800 * n)\ MHz,\ n = 1, \ldots, 9 \tag{3.1}$$

where n is the subband number.

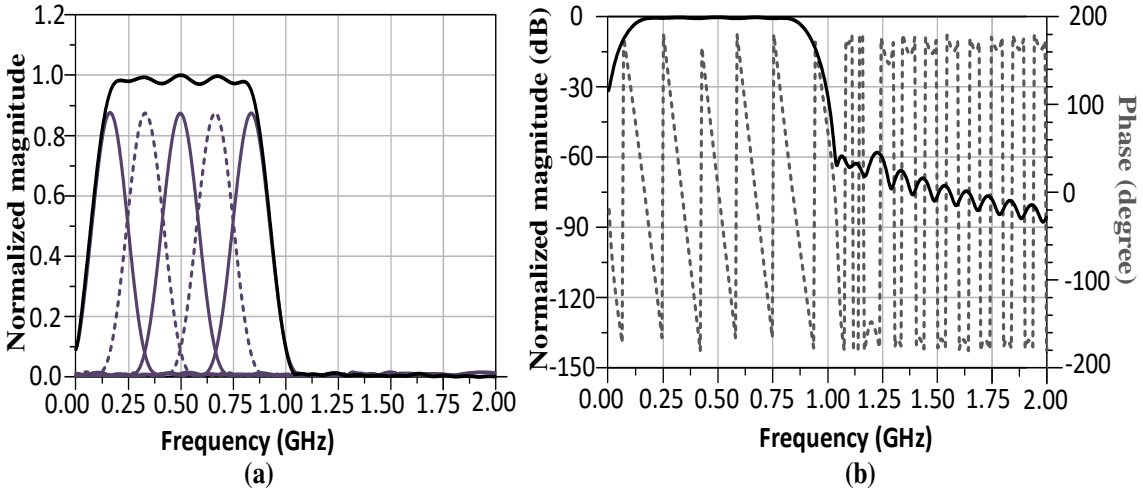

Figure 3.3: Proposed baseband signal, (a) added five up-converted Gaussian pulses and, (b) flat spectrum and linear phase change in 1 GHz. (Reprinted from [7])

These subbands have 100 MHz overlap from each side. With this approach, the information at the edge of the signal spectrum will not be lost (each subband has a flat amplitude spectrum with effective 800 MHz bandwidth). The UWB upconverter shifts the baseband pulse with 800 MHz bandwidth to each of these subbands accordingly, and the received signal is down converted to the same baseband frequency of 100-900 MHz centered at 500 MHz using the same LO signal.

3.2.2 Contact-Less Near-Filed Sensor and MUT Cuvette:

Traditional far-field broadband dielectric spectroscopy systems are commonly used at mm-Wave range since the volume of the liquid MUT is mostly within a few mm^3 which makes their implementation impractical for microwave range. In this work, a contact-less broadband near-field microwave sensor is employed as in [18]. Two broadband (3-10 GHz) Vivaldi antennas are coupled in their rediative near-field regions by placing them with a distance of 64 mm to minimize their effects on each other's return-loss characteristics [18]. Because of using the Vivaldi antennas, wide bandwidth, low cross polarization , and constant group delay are achieved. To place the liquid MUT between two Vivaldi antennas and reduce the required volume of the MUT, a Quartz-glass cuvette with the dimensions of 2x51x51 mm^3 is used to prevent the electromagnetic multiple-reflections/transmissions from MUT and edges of the cuvette [18] (also see Fig. 2.6 (c)).

3.2.3 System Analysis and Design Parameters:

For different MUTs (xylene, butanol, proponal, ethanol, ethanediol, methanol, and dmso), s-parameters of the contact-less sensor were extracted using Ansys High Frequency Structure Simulator (HFSS) in [18], showing the sensing unit has the loss variation of 12-to-26 dB (minimum loss is for xylene and maximum is for dmso). To target the detection of different materials with maximum SNR at the RX input, the link budget equation is used as follows

$$P_{RX}\ (dB) = P_{BB,in} + G_{TX} - P_{Losses} \tag{3.2}$$

where $P_{RX}\ (dB)$ is the received signal power at the RX input for the MUT with the lowest attenuation, $P_{BB,in}$ is the power of baseband pulse at the input of TX up-converter with the value of -32 dBm, G_{TX} is total gain of the TX RF unit, P_{Losses} represents the minimum loss of the entire sensing unit which includes transmitter/receiver antennas and MUT in the cuvette ($\sim$12 dB). Table 3.1 shows the break down of system-level specs for gain, noise figure (NF), and the 3rd order intercept point (IIP3) of broadband RF receiver front-end main blocks based on reported UWB CMOS blocks [49–51]. According to the system-specs, the total input 1-dB compression point (P_{1dB}) and the noise-figure of the RX (NF_{RX}) are found to be $\sim$ -22 dBm and 4.35 dB, respectively. Backing off sufficiently from the P_{1dB}, the maximum acceptable signal level (P_{RX}) at the receiver input in an interferer-free environment is set to be -30 dBm.

Table 3.1: Sytem Level Design Parameters of UWB RF Receiver Blocks (Reprinted from [7])

	UWB LNA	UWB Down-converter
Gain (dB)	17.5	5.5
NF (dB)	3.6	14
IIP3 (dBm)	-2.5	-11.5

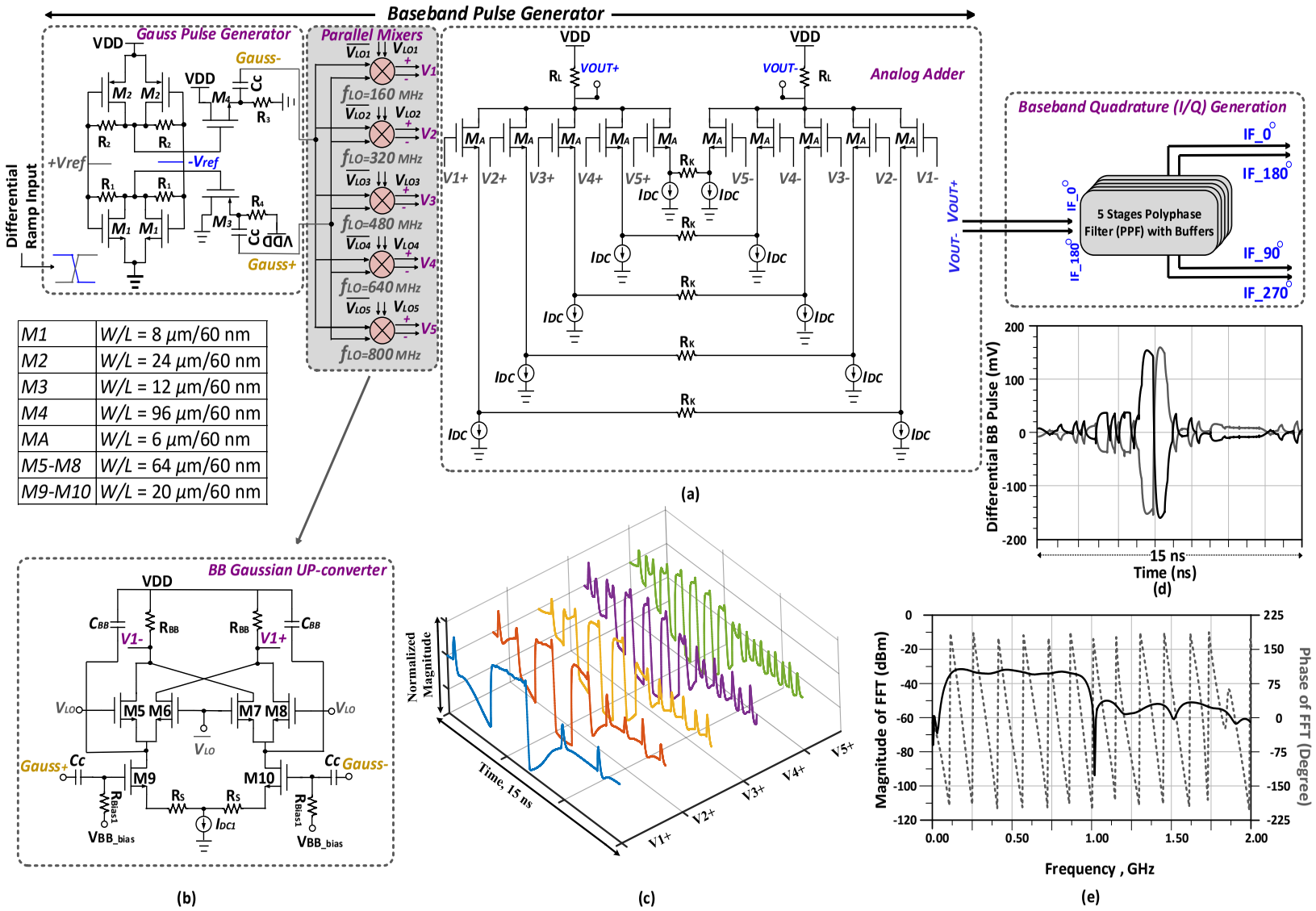

Figure 3.4: Baseband Unit; (a) transistor level circuit of baseband pulse generator along with PPF unit, (b) circuit topology of the baseband mixer, (c) up-converted Gaussian pulses at the input of analog adder, (d) simulation results of the generated baseband pulse in TD and, (e) its spectrum, respectively. (Reprinted from [7])

The required transmitter gain, G_{TX} (using (3.2)) and the total integrated noise power, which can be defined with $P_{Noise}\,(dBm) = -174 + 10log(BW_{RX}) + NF_{RX}$, ($BW_{RX}$ equal to 1 GHz for each sub-band), are found to be 14 dB and -79.65 dBm, respectively. The received maximum SNR at the receiver input, $SNR_{max}\,(dB) = P_{RX} - P_{Noise}$, is then ∼49.65 dB. Using similar approach, SNR_{min} for the highest material attenuation is found to be ∼35.65 dB.

3.3 Circuit Implementation

Circuit implementation and simulation results of the main MBDS system building blocks including the UWB transmitter (baseband pulse generator, polyphase filter (PPF), SSB up-converter, and PA), and the UWB receiver (LNA and down-converter) are all described in this section.

3.3.1 Transmitter Unit (TX)

3.3.1.1 Baseband Unit

3.3.1.1.1 Baseband Pulse Generation

The proposed differential-baseband signal generation circuit is demonstrated in Fig. 3.4(a). The circuit is composed of a Gaussian pulse generator, five double-balanced (DB) mixers, an analog adder, and a baseband LO signal generator. To form an excitation signal with a flat frequency spectrum with adequate amplitude and linear phase change all over the desired bandwidth, 5 Gaussian pulses with 10 dB bandwidth of 240 MHz at center frequencies of 160, 320, 480, 640, and 800 MHz are added Fig. 3.4 (b) and (c). The resulting baseband pulse with 500 MHz center frequency has a 10 dB bandwidth of 880 MHz. Simulation results of the generated baseband signal, with a larger constant phase slope when compared with a single Gaussian pulse are shown in Fig. 3.4 (d) and (e) with flat frequency spectrum. The faster phase permutation over the 1 GHz frequency span of the achieved signal does not affect the system accuracy of the MUT detection as also reported in [31].

An external symmetric differential voltage ramp signal is applied as the input of the Gaussian pulse generator. The required Gaussian pulse which is a combination of quadratic and exponential

functions is obtained by implementing one pMOS pulse generator with an nMOS source follower buffer ($M2, M4$) and one nMOS pulse generator with a pMOS source follower buffer ($M1, M3$) [47]. Since the long-channel nMOS transistors cannot follow the abrupt slope change for very short duration pulses, short-channel differential CMOS transistors are used. To generate the frequency shifted Gaussian pulses, differential Gaussian signals are ac coupled to the baseband DB Gilbert-cell mixers with a large capacitor ($C_c = 1.5$ pF) to prevent the generation of the Gaussian-mono cycle pulse Fig. 3.4 (b). In addition, by avoiding the upconversion of the dc values of the generated signal through the transmitter, the effect of the $1/f$ flicker noise at the receiver baseband unit is reduced.

Since signal amplification is not the main requirement in BB upconversion, gm of the RF transistors ($M9, M10$) inside each mixer is not very high, as a result, mixers have low CG, and LO switching transistors ($M5 - M8$) are properly sized to work with 100 μA to have proper abrupt switching and low power consumption. Considering the imperfect switching action, a rail-to-rail square pulse LO drive is preferred to avoid the noise and linearity degradation at baseband up-converters [52]. Minimum channel length is used for both the switching and the transconductance pairs to attain enough conversion gain and high LO-to-IF and LO-to-RF isolations. To increase the linearity, source degeneration resistors are used. Capacitor C_{BB}, ($C_{BB_i} = 904$ fF, 452 fF, 301 fF, 226 fF, and 181 fF, i=1, ..., 5 for five baseband up-converters), along with $R_{BB} = 990\ \Omega$ in Fig. 3.4(b) is utilized to lower the ripples at the desired baseband signal amplitude and suppress the high-frequency components to increase the spectrum flatness [53].

To combine the frequency shifted differential currents at five up-converter outputs (see Fig. 3.4(c)) and achieve high linearity, an analog adder with a source-degeneration resistor ($R_K = 5$ KΩ) is implemented. The small device aspect ratios are used to prohibit the common-mode signal at the output and reduce parasitics [47]. By increasing the common mode rejection at high frequencies, the LO feed-through at the output is also reduced.

Comparing the true single-phase clocked (TSPC) logic with Current-mode logic (CML) which provides very high-speed operation at the expense of high power consumption, TSPC D-flip-flop

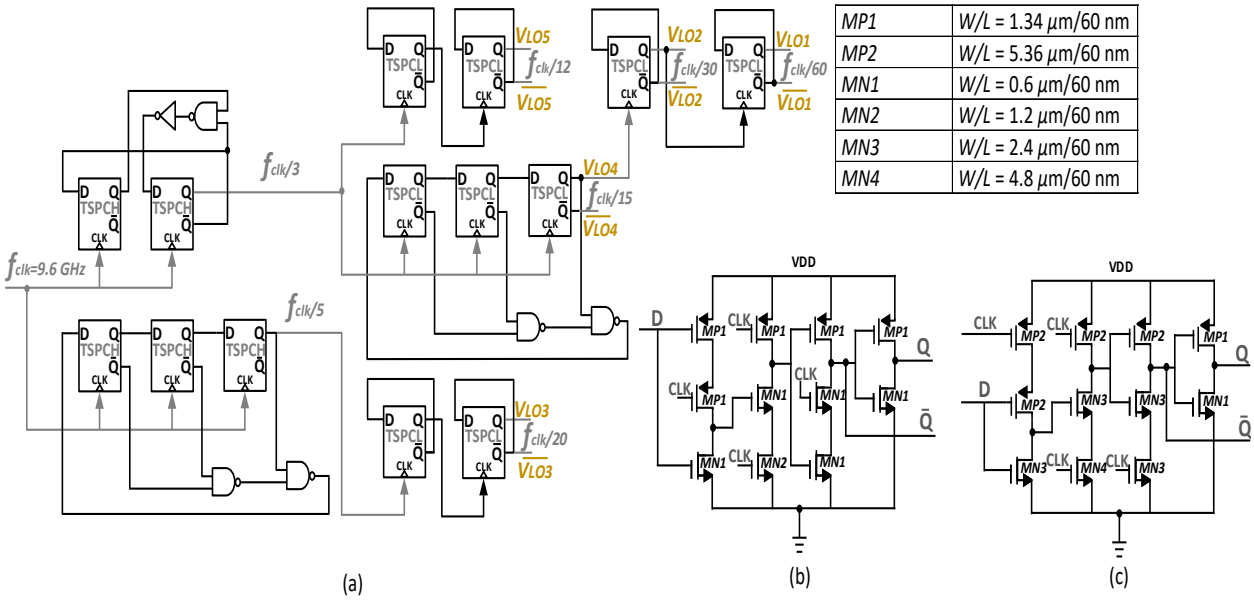

Figure 3.5: Baseband LO generation block diagram (a), high/low frequency clock generation,(b), and (c) TSPC-H/L DFF transistor level circuits , respectively. (Reprinted from [7])

(D-FF) is compact in size and does not require a differential clock and so does not have static power dissipation. It can also operate at multi-gigahertz frequencies [54]. As a result, TSPC D-flip-flops are implemented for integer frequency dividers to generate the required LO frequencies. Considering supply voltage, temperature, and process corner variations at higher frequencies, to achieve five simultaneous LO frequencies with acceptable propagation delay and to obtain a highly accurate baseband signal, two different TSPC D-FFs are used, one for the high frequency input dividers (TSPCH), and the second one for the low frequency dividers (TSPCL). The block diagram of the entire frequency dividers and the architectures of D-FFs are shown in Fig. 3.5 (a), (b), and (c) [54, 55]. To generate different baseband LO frequencies, an external input signal with the frequency of 9.6 GHz (f_{clk}) is divided by the divider ratios $12/15/20/30$, and 60. Regardless of the divider ratio, TSPC D-FF provides an output clock with a 50% duty-cycle except the one with ratio 15, hence, a similar architecture explained in section 3.3.3 (Fig. 3.13(c)) is used for this LO frequency duty-cycle correction.

As seen in Fig. 3.6, the measured BB pulse has peak-to-peak voltage of 280 mV in TD and flat

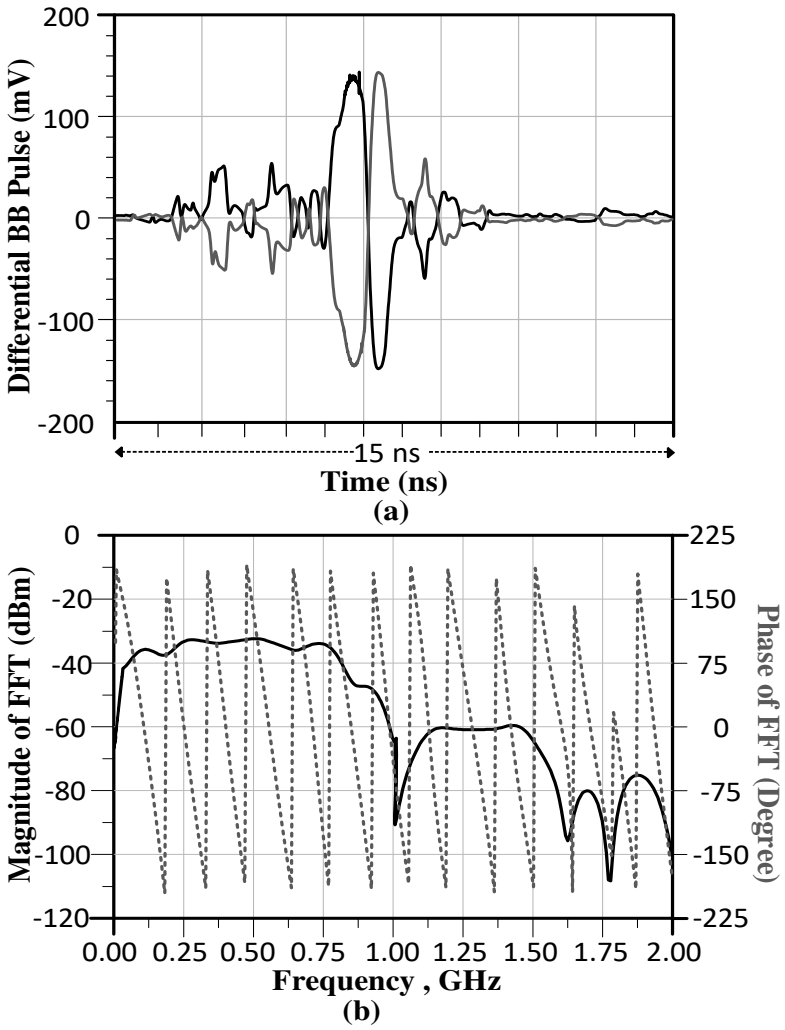

Figure 3.6: (a) Measured baseband pulse in TD, and (b) measured pulse spectrum. (Reprinted from [7])

magnitude with linear phase change within 1 GHz span.

3.3.1.1.2 PPF and Buffers

A 5-stage cascaded passive polyphase filter (PPF) with 5-pole used for quadrature phase generation and derived from the classical RC-CR phase-shift network (Fig. 3.7(a)). The PPF is chosen due to its small chip area and simple design, though it has a high inherent loss (4 dB). The PPF converts the differential baseband input signals into four quadrature-phase IF signals that are fed into the SSB up-converter. According to [56], a single stage PPF provides exactly 90-degree phase difference between I and Q signals at its output over all frequencies independent of the R/C values,

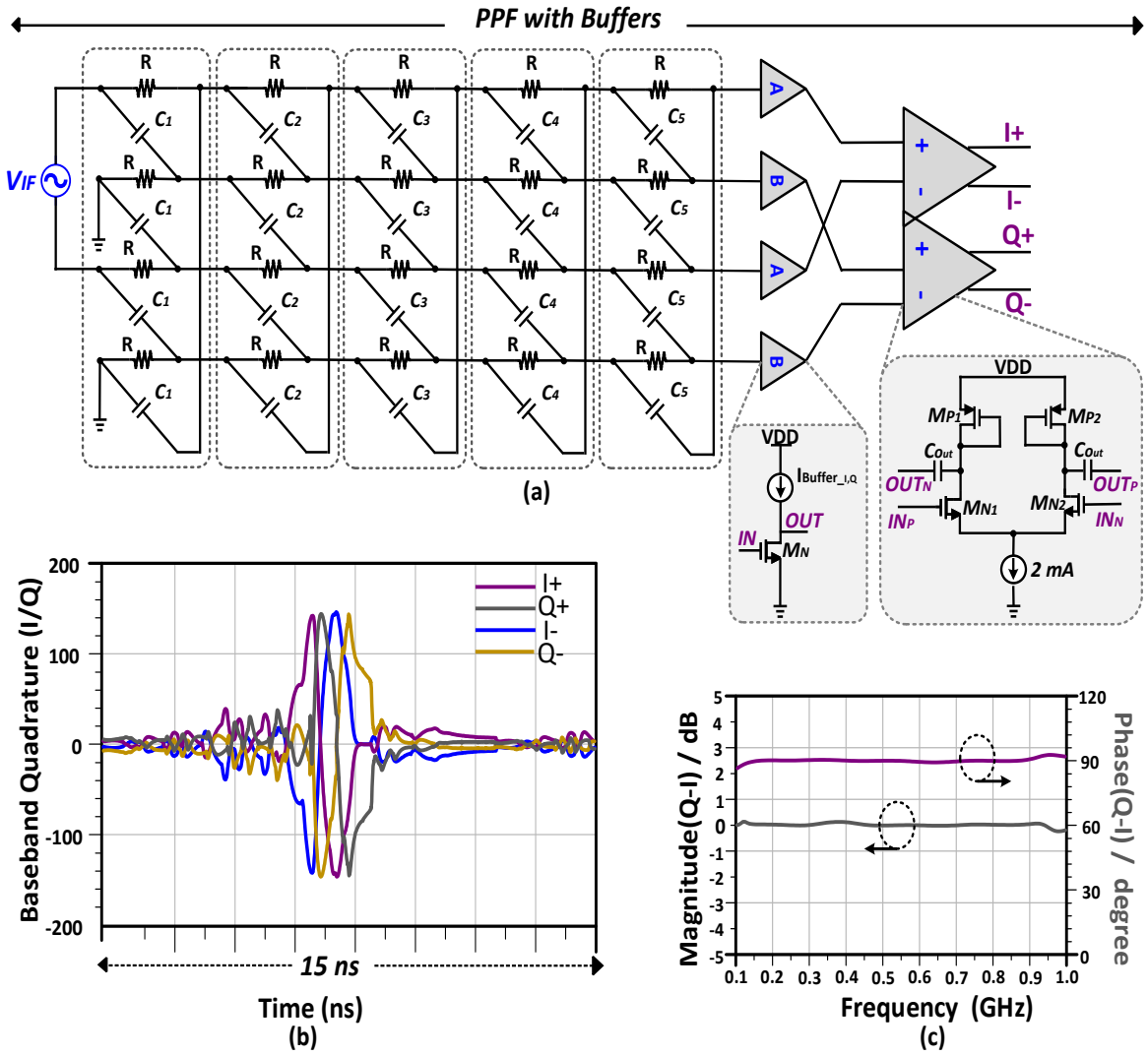

Figure 3.7: (a) Transistor level schematic of the 5-stage PPF network with 2-stage output buffers , (b) generated quadrature I/Q outputs in time domain, and (c) magnitude and phase mismatches of the quadrature signals. (Reprinted from [7])

but the unity gain balance is achieved at $w_0 = 1/RC$. Consequently, implementation of a multi-stage poly-phase filter circuit not only extends the amplitude balance in a fairly wide band but also decreases the sensitivity of the filter against the on-chip RC process variations. The highest I/Q accuracy and required bandwidth of the PPF network with poles equal to the baseband LO carrier frequencies are determined by choosing the value of R = 2 KΩ and C_1, C_2, C_3, C_4, and C_5 = 498 fF, 249 fF, 166 fF, 124 fF, and 99 fF, respectively. Subsequently, by adopting the 5-stage PPF with

sequential poles, imperfect quadrature phase and imbalanced amplitude are mitigated, and unity magnitude for the desired frequency range is achieved along with 90^0 phase balance at all desired frequencies with an average 1.325 dB gain and 0.978 degree phase mismatch over 0.1-1 GHz as shown in Fig. 3.7 (b) and (c), respectively.

Dc blocking capacitors at the input and output of the PPF are chosen in a way not to affect the lowest or highest frequency pole of the filter. To prevent the mismatches caused by the loading effect of the SSB mixer, two-stage output buffers follow the IF polyphase network, with the schematic illustrated in Fig. 3.7(a). To compensate for added insertion loss throughout the PPF, the first stage of the buffer is realized as a CS amplifier with a 140 μA current-source supply to provide high input resistance (R_{in}) and high voltage gain ($|A_v|$).

To maximize the image rejection of the up-converter stage, the phase and magnitude flatness over the 1GHz BW is important so two different tuning nodes ($I_{Buffer,I}$ and $I_{Buffer,Q}$) are used to optimize the current supply for the quadrature and in-phase paths after fabrication. To avoid the degradation of the voltage gain due to loading effect of the next stage, a single-stage differential unity gain amplifier ($|A_v| = g_{mN}/g_{mP} = 1$) with diode-connected load is utilized as the second stage of the buffer. The symmetrical layout of the filter with the buffer stage minimizes the effect of the parasitic capacitors and resistors to ensure near perfect balanced quadrature IF signals enter the SSB mixer.

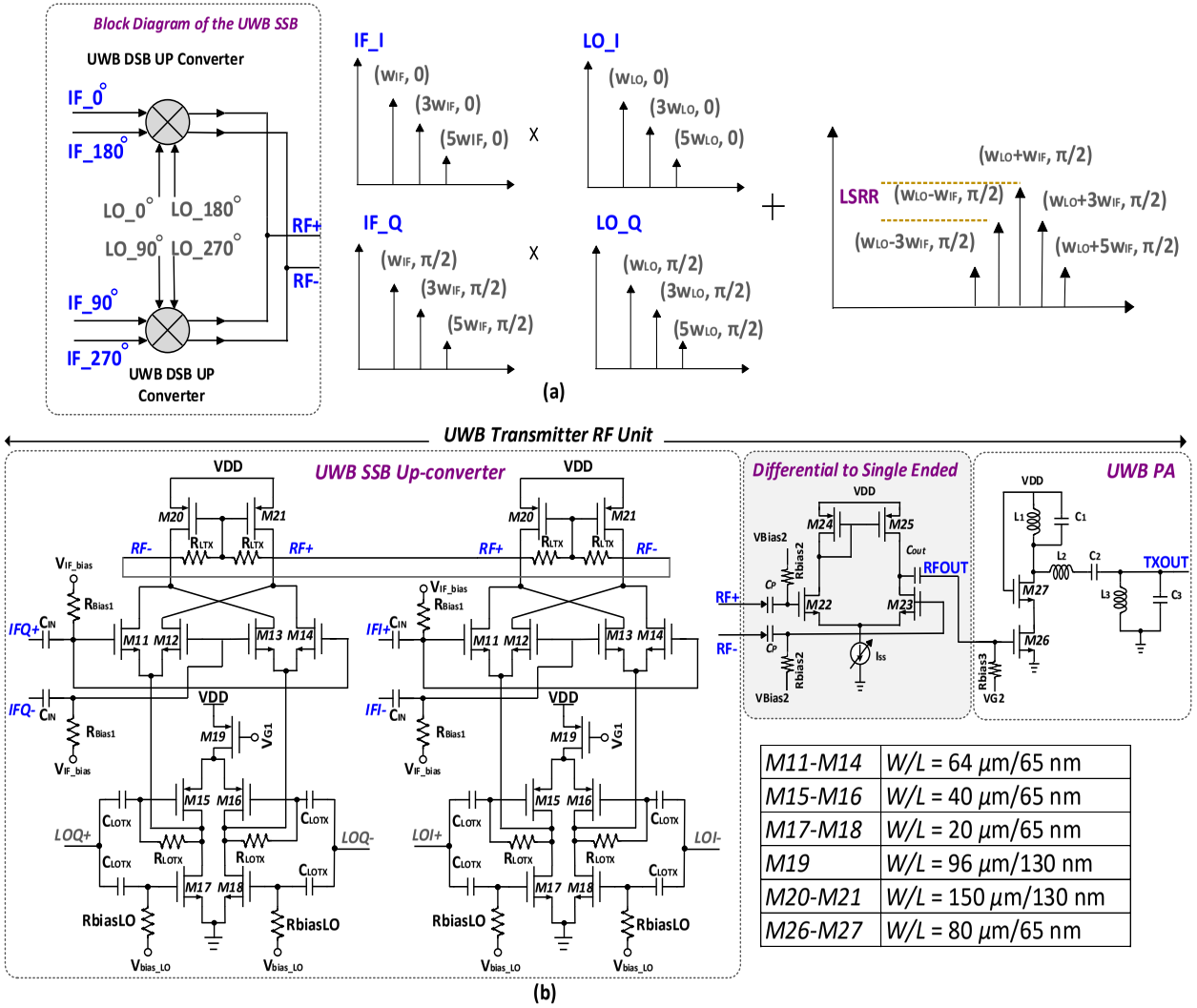

M11-M14	W/L = 64 µm/65 nm
M15-M16	W/L = 40 µm/65 nm
M17-M18	W/L = 20 µm/65 nm
M19	W/L = 96 µm/130 nm
M20-M21	W/L = 150 µm/130 nm
M26-M27	W/L = 80 µm/65 nm

Figure 3.8: (a) Block diagram of the SSB upconverter along with the conceptual signal spectrum , and (b) transistor-level schematic of the UWB TX RF Unit (UWB SSB up-converter, DTS, and UWB PA). (Reprinted from [7])

3.3.1.2 RF Unit

3.3.1.2.1 UWB SSB Up-converter

The block diagram of the UWB SSB up-converter along with the signal spectrum is shown in Fig. 3.8(a) [57, 58] and the circuit schematic of the SSB up-converter core as part of transmitter unit is shown in Fig. 3.8(b), respectively. The up-converter is realized with two interconnected identical double-side-band (DSB) mixers that act as up-converters for I and Q signals generated by PPF and an analog-adder to add the outputs of two DSB mixers as shown in;

$$\begin{aligned} V_{SSB}(t) &= Acos(w_{IF}t)cos(w_{LO}t) \\ &\quad + Acos(w_{IF}t + \pi/2)cos(w_{LO}t + \pi/2) \\ &= Acos(w_{IF}t)cos(w_{LO}t) \\ &\quad - Asin(w_{IF}t)sin(w_{LO}t) \\ &= Acos(w_{IF}t + w_{LO}t) \end{aligned} \tag{3.3}$$

In the ideal case, the IF input is up-converted in a way that only the upper RF sideband is retained while the unwanted lower-sideband image is internally suppressed. However, in practice, because of the I/Q mismatches, the phasor representing the image (at $w_{LO} - w_{IF}$ in Fig. 3.8(a)) will not be canceled out perfectly. Additionally, SSB mixer produces sidebands due to its own nonlinearities that create spurs in the spectrum [57]. Therefore, to minimize the inter-modulated spurs, a symmetric layout is utilized. While all transistors are biased in the saturation region, for broadband application and reducing die area, active loads are used instead of LC tank which requires inevitably large area. The differential IF input is applied to the switching quad whereas LO inputs are exploited to the inverter part. Full-swing quadrature square-pulse LO inputs are utilized, apart from improving conversion gain, the suppression of unwanted sideband is improved. As mentioned before, accuracy of the entire MBDS system is strongly affected by the lower-sideband rejection ratio (LSRR) of SSB up-converter. According to the spectral simulation results, LSRRs

for different sub-bands (each with 800 MHz bandwidth) fall in the range of 18-60 dB as shown in Fig 3.9.

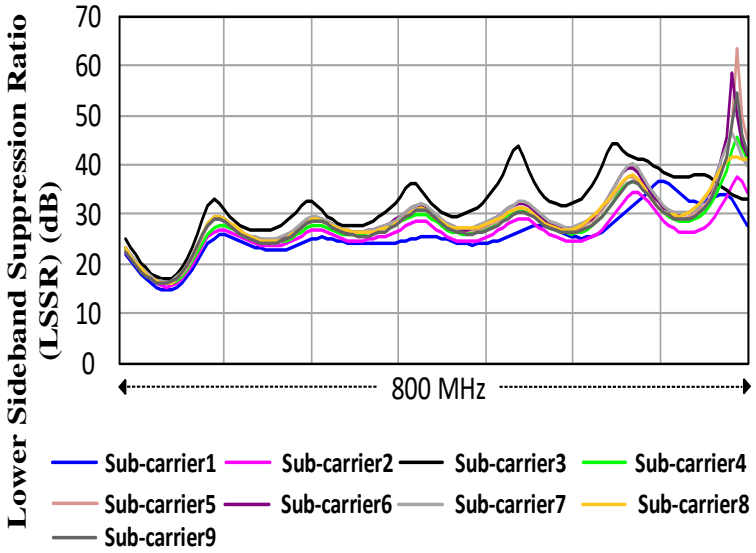

Figure 3.9: Simulation results of the lower-sideband suppression ratio (LSSR) for each sub-carrier with 800 MHz BW at RF TX output over 3-10 GHz. (Reprinted from [7])

3.3.1.2.2 Differential-to-Single Ended Converter and Power Amplifier

The output of the UWB SSB up-converter is converted from differential to single-ended to drive the single-ended Class-A UWB power amplifier (PA) with a single-ended antenna [59]. The schematics of the differential-to-single-ended converter (DTS) and UWB PA are demonstrated in Fig. 3.8(b). To convert the output of up-converter to a single-ended signal and provide a high impedance to the mixer output, a differential amplifier (DA) buffer with active load is used. To provide high unity gain bandwidth, decrease the delay, and lower the power consumption with a low threshold voltage, the differential to the full-swing converter is designed with the short channel length. The presence of the converter should not affect performance of the SSB up-converter adversely and thus the buffer is constructed with the gain of $\sim$2 relaxing the gain requirement of the proceeding PA stage. To improve the common-mode rejection ratio (CMRR), Wilson current mirror is used as a tail current source.

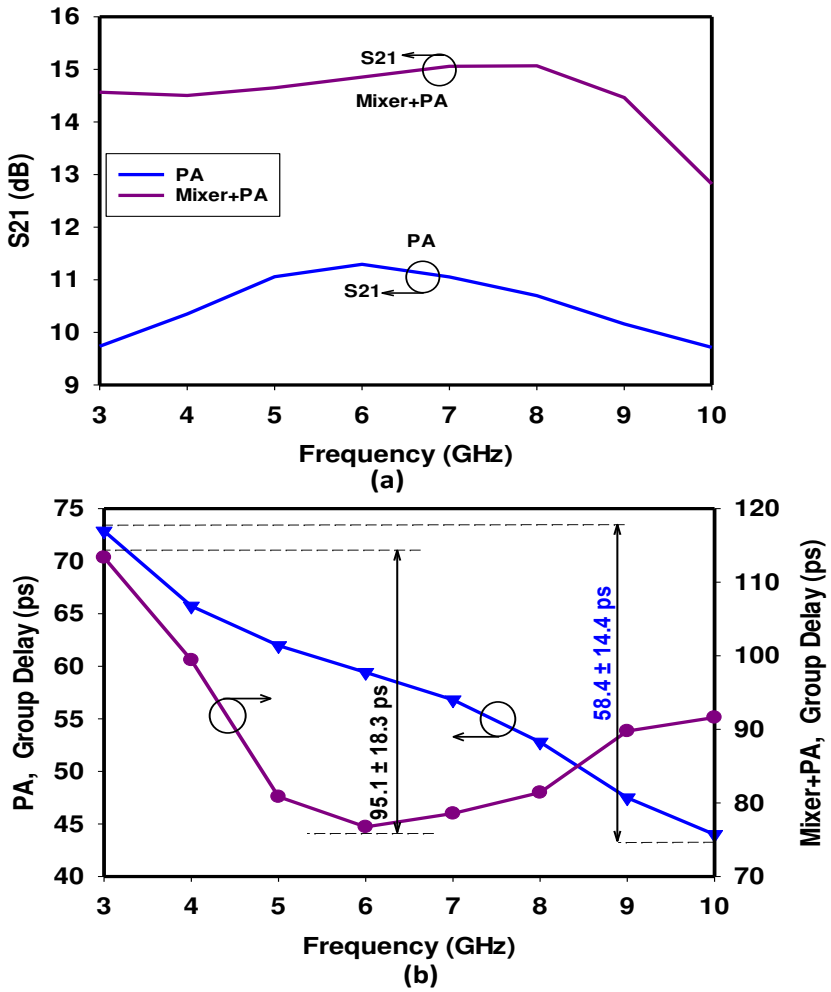

Figure 3.10: UWB Transmittersimulation results, (a) S21 of the UWB PA and Mixer+PA, and (b) group delay (GD) of the UWB PA and Mixer+PA. (Reprinted from [7])

A Class-A PA is designed with all transistors in the saturation region to preserve the linearity. While L_1 and C_1 are adjusted to extend the BW, cascaded $M26$ and $M27$ with lumped components are sized to achieve flat-group delay and gain. To obtain the wideband impedance matching at the output of the PA for 3-10 GHz range, a third-order BPF ($L_1 - L_3$ and $C_1 - C_3$) is used. The simulation results of the entire TX RF unit including SSB up-converter and PA are depicted in Fig. 3.10 (a) and (b). The transmitter RF unit achieves flat forward gain ($S21$) of 14 ± 1 dB, and GD of PA when is connected to SSB up-converter ($LO : ON$), is 95.1 ± 18.3 ps.

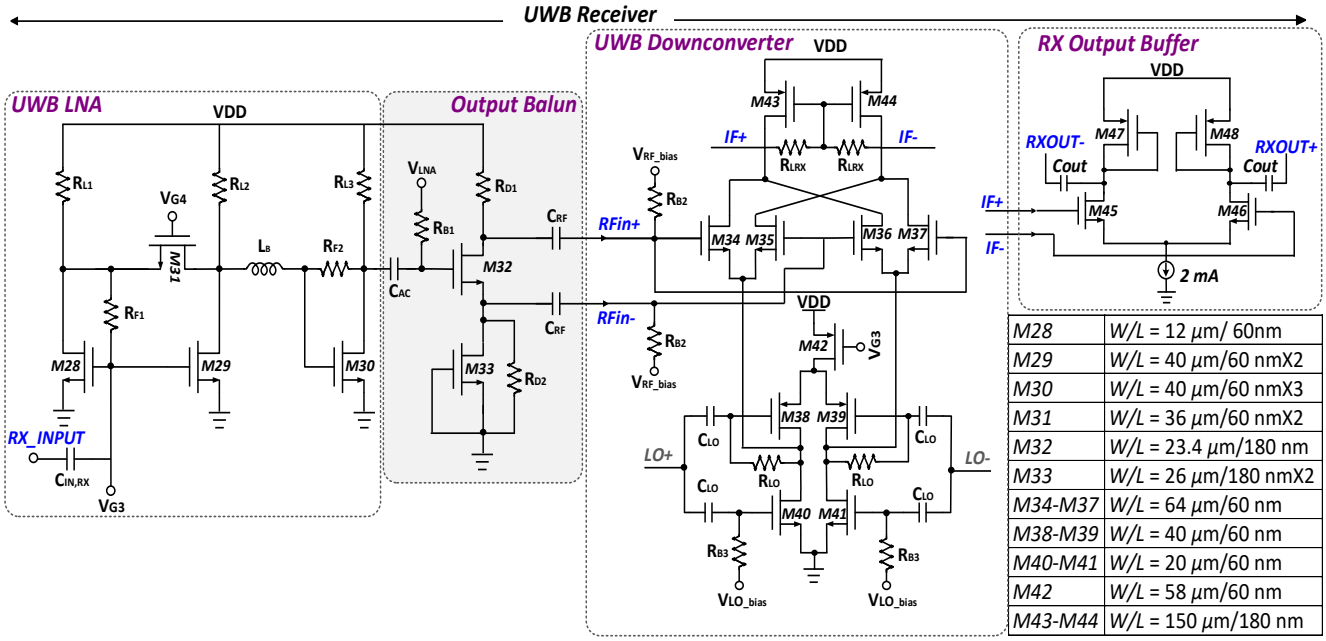

M28	W/L = 12 μm/ 60nm
M29	W/L = 40 μm/60 nmX2
M30	W/L = 40 μm/60 nmX3
M31	W/L = 36 μm/60 nmX2
M32	W/L = 23.4 μm/180 nm
M33	W/L = 26 μm/180 nmX2
M34-M37	W/L = 64 μm/60 nm
M38-M39	W/L = 40 μm/60 nm
M40-M41	W/L = 20 μm/60 nm
M42	W/L = 58 μm/60 nm
M43-M44	W/L = 150 μm/180 nm

Figure 3.11: Schematic of RX front-end for the proposed miniaturized contactless microwave broad band dielectric spectroscopy (MBDS) system. (Reprinted from [7])

3.3.2 Receiver Unit (RX)

At the RX front-end, the output of the contact-less sensor is applied with a large input capacitor $C_{IN,RX} = 5\,pF$ to a single-ended UWB low noise amplifier (LNA) covering the 3-10 GHz desired frequency band. Afterwards, the signal at the output of the LNA is converted to a differential signal along with an active output balun, which is subsequently applied to a UWB down-converter for frequency-down-conversion and detection. Fig. 3.11 demonstrates the circuit schematic of the entire UWB receiver front-end.

3.3.2.1 UWB LNA

The main requirement of the RX is providing flat group delay and flat gain within 3-10 GHz frequency range. The essential constraints in the design of the LNA are high gain to achieve low noise figure for the entire RX, broadband input matching to minimize the return loss, low input referred noise to enhance the sensitivity of the receiver, flat group delay to reduce phase errors

introduced during signal detection, high linearity to preserve shape of the received pulse, low power consumption and small die area for better signal integrity. As a result, a noise canceling gain-enhanced technique with resistive feedback is implemented to achieve simultaneous wideband input matching with low input referred noise, as depicted in Fig. 3.11 [60]. A common-gate transistor $M31$ is added to make both $M28$ and $M29$ drain signals in-phase to subtract the noise at drain of $M29$ and to increase g_{m28} by providing some part of the current into $M28$ drain. Correspondingly, the size of $M28$ is reduced for matching at higher frequencies and low noise figure is obtained by canceling the noise of $M28$ with the noise of $M29$ and $M31$ [60]. Since $M31$ in the upper feed-forward path matches the phase delay for two paths, a flat wideband group delay for LNA is realized.

To accomplish the input matching at low frequencies, a shunt feedback resistor R_{F1} = 150 Ω and to increase the overall gain, a resistive shunt feedback, R_{F2} = 365 Ω are used. By connecting an inductor L_B = 1 nH between the drain of $M29$ and gate of $M30$, a series LC resonance with the gate capacitance of $M30$ is exploited. Consequently, the group delay flatness is improved and the bandwidth of the LNA with flat gain is extended for 3-10 GHz range.

To generate differential input signals for down-converter mixer, a common-source (CS) amplifier with resistive load and degeneration comprising transistors $M32$ and $M33$ (a dummy transistor to achieve the balance with drain capacitance of $M32$) are utilized as shown in Fig. 3.11. The active balun provides high linearity with low power consumption [61,62]. To reduce the mismatches on differential signal outputs due to short channel effects and load impedance variations, and ensure the differential conversion linearity, $M32$ and $M33$ of $L = 180\ nm$, $R_{D1} = 214\ \Omega$, and $R_{D2} = 240\ \Omega$ are used , respectively, resulting in 0.75 dB and 3.5^0 amplitude and phase imbalance within 7 GHz, as shown in Fig. 3.12(a).

The proposed UWB LNA achieves simulated $S11$ of -13.7 to -17.5 dB, flat forward gain $S21$ of 17.7 ± 0.4 dB with a NF of 3.6 dB, and excellent GD variation of ± 4.02 ps over the 3-10 GHz band as shown in Fig. 3.12(a), (b), and (c).

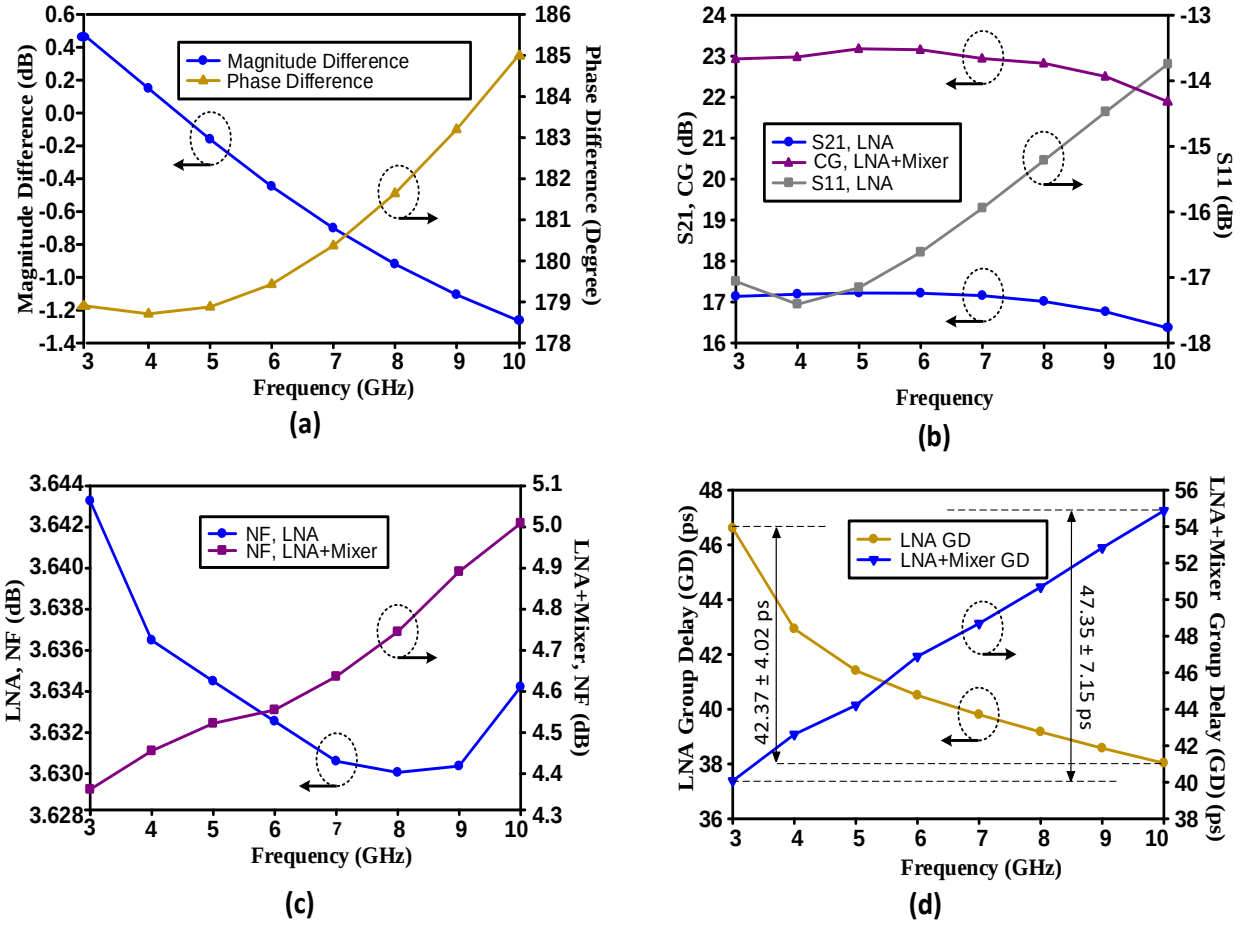

Figure 3.12: RX front-end simulation results, (a) phase and magnitude difference of the differential output of the LNA, (b) S21, S11 of the UWB LNA and conversion gain (CG) of the LNA+Mixer, (c) noise figure (NF) of the LNA and LNA+Mixer, and (d) group delay (GD) of the LNA and LNA+Mixer. (Reprinted from [7])

3.3.2.2 UWB Downconverter and Output Buffer

The double-balanced switched transconductor (SwGm) UWB down-conversion mixer architecture is employed as shown in Fig. 3.11 [63]. Compared to a standard Gilbert-cell mixer, this topology provides lower flicker noise, noise figure, and higher linearity with similar conversion gain. The LO stage ($M38-M41$) converts input differential LO voltage to current for the transconductance of RF stage ($M34-M37$) [64]. To overcome the voltage headroom problem and increase

the conversion gain (CG), the load resistors are replaced with active load devices having common-mode feedback (CMFB) resistors, ($R_{LRX} = 3.6$ KΩ).

In order to further increase flat-conversion gain, lower the noise figure and third order non-linearity, bias current of the RF transconductance stage transistors is decoupled from LO switching stage transistors [60, 65]. The RF transistors are biased in moderate inversion to achieve high enough conversion gain ($\sim$6 dB). It is imperative to have near square wave LO signal to drive LO transistors for flat conversion gain and low power consumption. Therefore, a buffer with a shunt-feedback resistor ($R_{LO} = 160\ \Omega$) providing constant transconductance ($g_{mn} + g_{mp}$) is chosen for LO transistors [60, 66]. For UWB matching at the LO input terminal, a relatively small feedback resistor (R_{LO}) is used, hence; the LO input return loss better than 10 dB over the frequency range is accomplished [60]. The differential double-balanced topology reduces LO-IF leakage, and provides a constant impedance to LNA.

A differential output buffer dc coupled to the down-converter is used to drive a $50\ \Omega$ output system load. System simulations show placing different materials inside the contact-less sensor varies the input of the LNA from -24 to -12 dBm. LNA+Mixer front-end is tested to prove that the system has flat gain for desired 3 to 10 GHz band the results are shown in Fig. 3.12(b). The RX unit achieves conversion gain of 22.45 ± 0.45 dB, NFmin of 4.365 dB (Fig. 3.12(b) and (c). The value of GD when LO is ON, is 47.35 ± 7.15 ps providing very good phase linearity as shown in Fig. 3.12(d).

3.3.3 Quadrature LO Generation for Up/Down-Converter

To generate the required differential quadrature LO signals, the frequency of the external differential input clock (5.8-18.4) GHz is divided-by-2. As shown in Fig. 3.13(a), the divider is implemented by cascading two differential D-latches. A static current mode logic (CML) frequency divider with inductive peaking ($L \simeq$ 1nH and $R_L \simeq 470\Omega$) is chosen to achieve a faster dividing operation with a broad-band range and low power consumption [67]. Fig. 3.13(b) illustrates the circuit diagram of the CML divide-by-2 frequency divider based on the master ($M49 - M54$) and slave latches ($M55 - M60$). To increase the signal injection and relax the voltage headroom, the

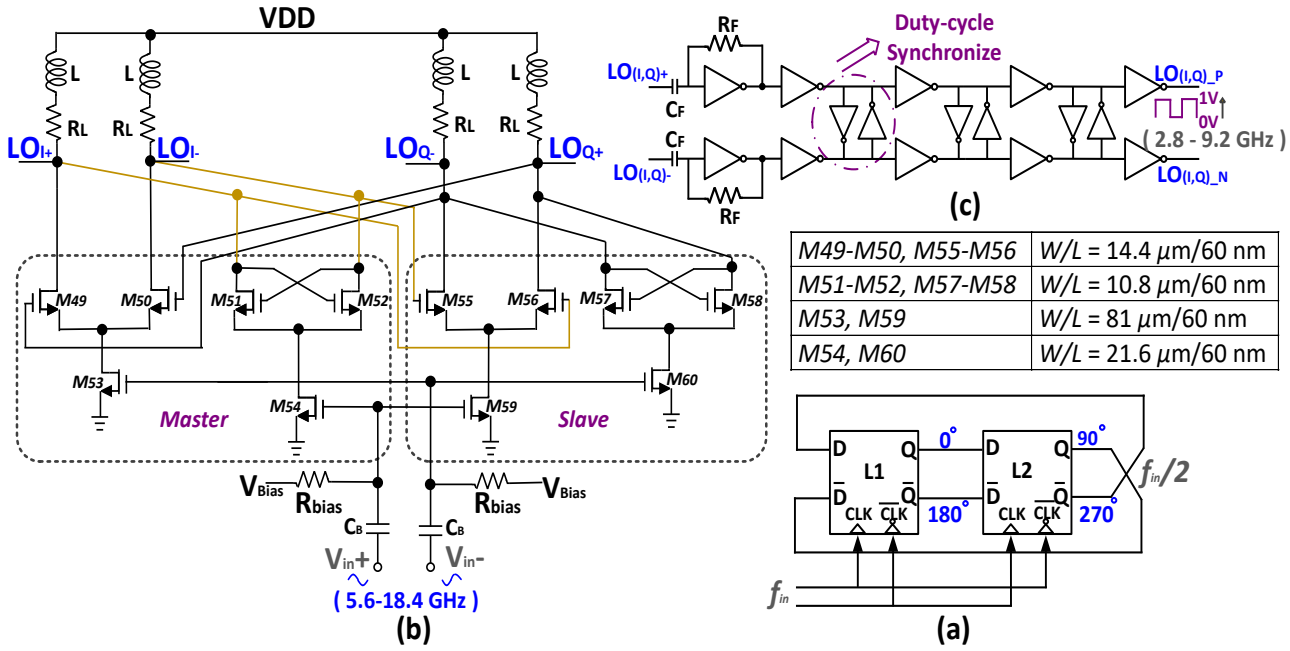

Figure 3.13: Circuit topology of differential quadrature LO generation/distribution unit, (a) CML frequency divider-by-2, (b) divider schematic, and (c) CML-to-CMOS converter and duty cycle corrector. (Reprinted from [7])

tail current transistors are eliminated. To realize the high frequency input matching, R_{bias} resistors are set to 50 Ω, where $C_B = 1.2$ pF is used for input ac coupling. In addition, the cascaded load (L and R_L) will increase the loop gain for good latching. Employing smaller biasing current for the cross-coupled pairs ($M51 - M52$ and $M57 - M58$) compared to the sampling pairs transistors ($M49 - M50$ and $M55 - M56$) results in enhancement of the operation frequency and locking range of the CML divider [67]. The frequency divider is followed by a CML-to-CMOS converter composed of a dc blocking capacitor ($C_F = 1$ pF) and a self-biased inverter with a shunt resistor ($R_F = 10$ KΩ) shown in Fig. 3.13(c). After a chain of inverters, outputs of the divider are converted to rail-to-rail square pulses. The duty cycles of the differential quadrature outputs, I and Q, are synchronized by back-to-back inverters. The last inverters are sized to drive the UWB SSB up-converter along with the UWB down-converter mixer. To ensure that the differential quadrature signals have a duty cycle of 50%, the symmetrical layout is needed to match the delays of the I/Q paths by reducing the parasitic capacitances of the transistors and metal wiring.

3.4 System Integration and Test Set-up

The chip microphotograph of the proposed MBDS system is shown in Fig. 3.14(a), which is fabricated using 65-nm CMOS process and occupies a total chip area 1.68 mm^2 with an active core area of 1.24 mm^2, and consumes overall average power of $\sim$ 67 mW from a 1 V supply. For the chip assembly, a micro lead frame (MLP) 7x7 mm^2 QFN 44 pin package is used, while the wire-bonding is utilized for the all electrical connections between the chip and the package lead frame. A hybrid 4-layers printed circuit board (PCB) with an overall thickness of $\sim$ 1.57 mm is utilized consisting of a top layer Rogers 4350B substrate with ϵ_r = 3.66, tan δ = 0.0031, and thickness of 0.254 mm, and other layers as ISOLA-FR408HR substrate with ϵ_r = 3.68 and tan δ = 0.0092 to reduce the loss for RF signals. The test setup of the prototype (PCB with the packaged chip and the contact-less sensing unit) is illustrated in Fig. 3.14(b). Gaussian pulse generator block is excited with an external ramp input signal with a 42 ns period, 10.5 ns leading/trailing times, and 0.5 Vp-p with 250 mV dc-offset from a dc-power supply using the N8241 Arbitrary Waveform Generator. A 9.6 GHz single-tone with 4 dBm power is generated by E8267D PSG Vector Signal Generator and used for TSPC frequency divider unit to generate the baseband LO clocks. An external single-tone LO (5.6-18.4 GHz) with 1 dBm power provided by N5230A VNA was applied to the quadrature LO generation unit for up/down converters through a 180^0 hybrid with a 3 dB loss at each output. The MUT carrier was capped with a lid to avoid evaporation for the accuracy of the material characterization and placed in middle of the two Vivaldi antennas. Afterward, the differential output of the receiver is first combined with an off-chip power combiner, then applied to an off-chip LPF to filter out the high-frequency harmonics and the noise to improve the SNR, and finally was captured by infiniium DSA91304A oscilloscope. The TD output for each sub-band is stored in oscilloscope within a 15 ns window for material characterization.

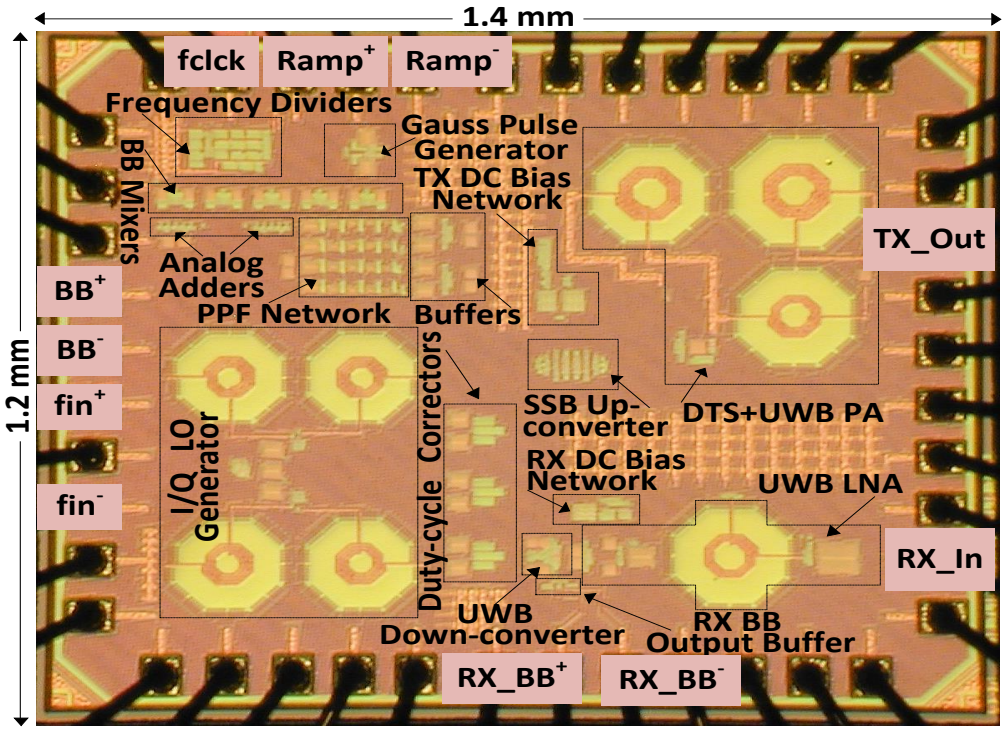

(a)

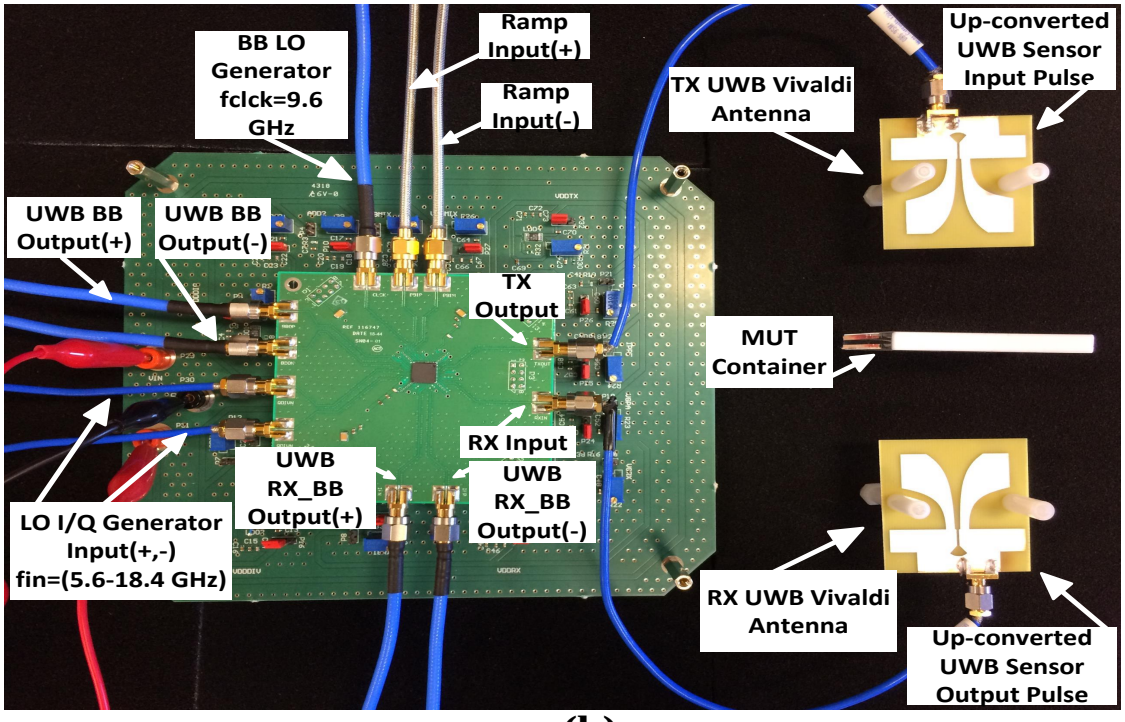

(b)

Figure 3.14: (a) Micrograph of the fabricated MBDS sytem chip, and (b) test set-up for the proposed MBDS system with packaged chip, respectively. (Reprinted from [7])

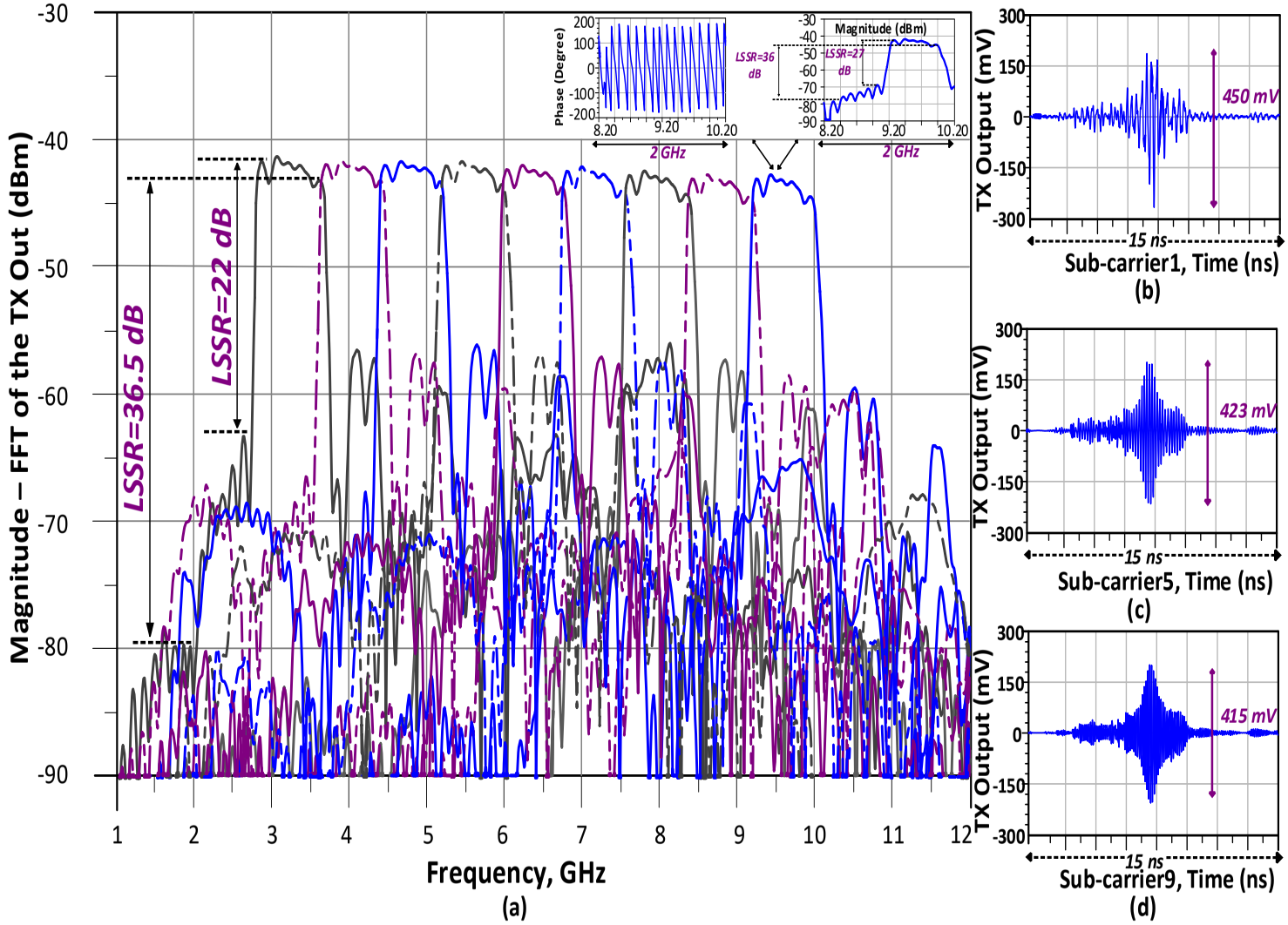

Figure 3.15: (a) Measured magnitude of nine sub-carriers at TX output with flat spectrum , and (b,c,d) measured sub-carriers 1, 5, and 9 in TD, respectively. (Reprinted from [7])

3.5 Experimental Results

3.5.1 Electrical Characterization

The nine sub-carriers measured magnitude at the transmitter output are shown in Fig. 3.15(a) versus frequency. The captured single-ended TX outputs in TD for 3 sub-carriers (1,5,9) are provided in Fig. 3.15(b), (c) and (d), which verify the signal peak-to-peak amplitudes (450 mV $\sim$ 415 mV) are relatively close from the lowest to the highest sub-carrier. Although there is a small magnitude drop as frequency increases, a flat spectrum within the desired frequency range is achieved at the output of the transmitter for each sub-band as shown in Fig. 3.15(a). In order to better show the phase and magnitude change in each sub-band, the last sub-carrier with 2 GHz BW is also shown in Fig. 3.15(a). It can be seen that the shape of the transmitted signal is preserved with a uniform spectrum and linear phase change. Furthermore, the lowest and highest lower sideband suppression ratio (LSSR) are equal to 27 dB and 36 dB, respectively. When the output of the TX is passed through the MUT, the lower sideband of each sub-carrier is already suppressed due to image rejection. Hence, the effect of the material dispersion at RX baseband output will be very small and does not significantly affect the accuracy of the system.

3.5.2 Chemical Characterization and Calibration

To verify the performance of the fabricated MBDS system, seven different organic chemical liquids (xylene, butanol, proponal, ethanol, ethanediol, methanol, and dmso) and binary mixtures (ethanol-methanol) with volume of $\sim$ 5 mL are applied to the contact-less sensing unit. For different MUTs, RX BB output is measured by repeating and averaging 10 times at each sub-band for an MUT, with a standard deviation less than 0.007 within the desired 7 GHz BW (1024 number of averaging points applied during each data capturing). In order to obtain solely the MUT properties, the effects of the entire transceiver are calibrated by subtracting the empty system (MUT = air) measurement results from the loaded system (MUT $\neq$ air) results. Consequently, measured phase and magnitude differences with respect to the reference material, air, ($\Delta\phi$ = ϕ_{Air}-ϕ_{MUT} and ΔMag = Mag_{Air}-Mag_{MUT}) are obtained using the FFT to the captured TD signal at the RX out-

put in MATLAB. The subtraction and the FFT conversion of the captured TD data is proceeded for each sub-band in MATLAB, then $\Delta\phi$ and ΔMag are mapped from baseband RX outputs (100-900 MHz) to the RF frequencies (3-10 GHz) to present the entire frequency span as shown in Fig. 3.16(a) and (b). Although ϵ_r' and ϵ_r'' of air and xylene or butanol and propanol are very similar, the proposed system is successfully capable of discriminating those MUTs from each other as illustrated also using TD measurements in Fig. 3.16(c).

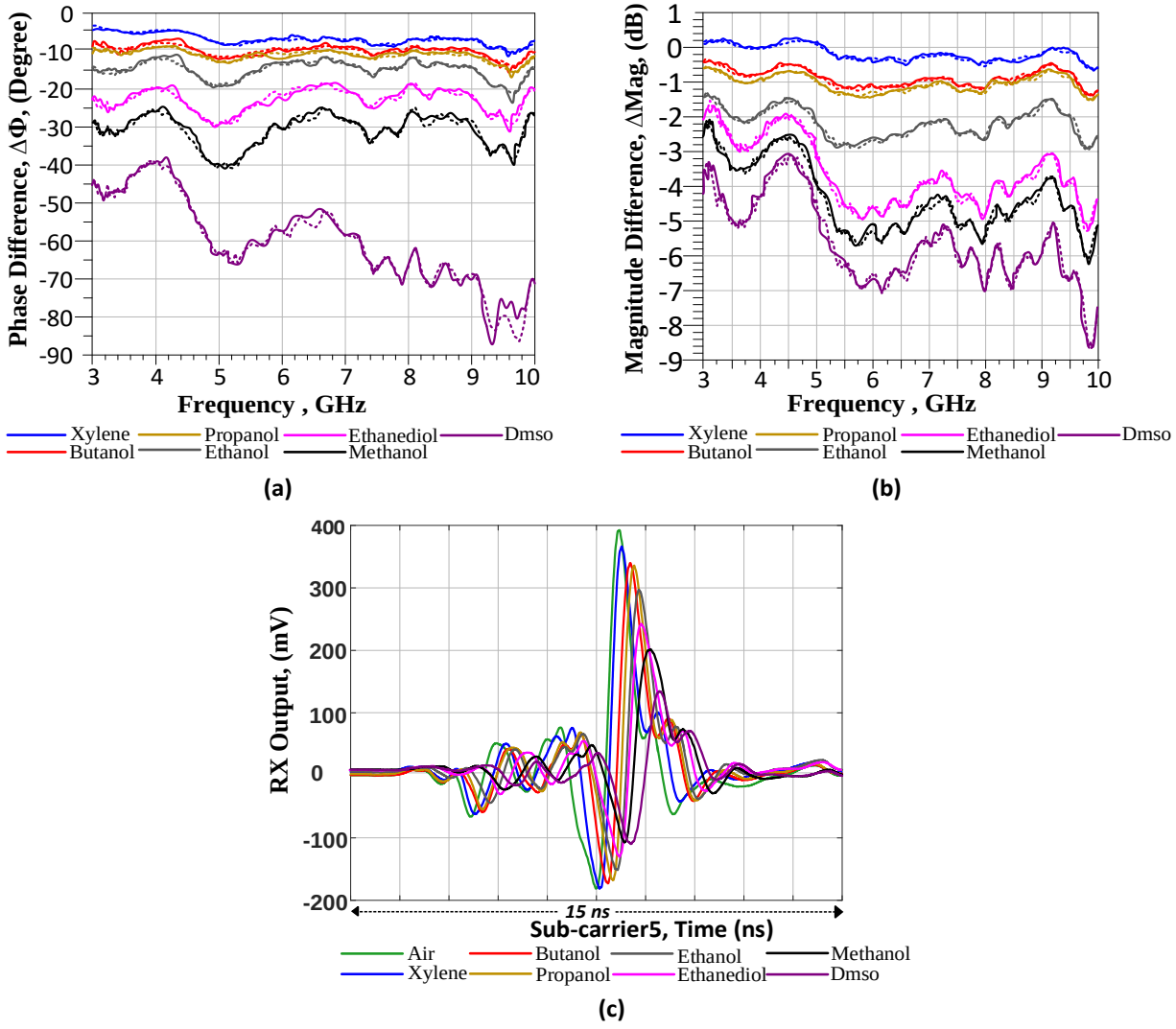

Figure 3.16: (a) $\Delta\phi$-phase and (b) ΔMag-magnitude measurement results of the proposed MBDS system compared with the VNA, and (c) system output in TD for sub-carrier5. (Reprinted from [7])

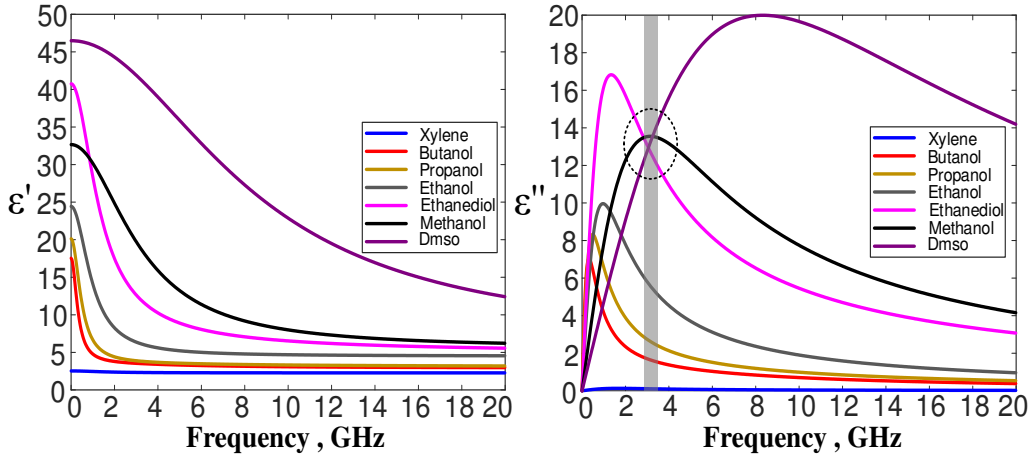

Figure 3.17: Theoretical ϵ_r' and ϵ_r'' curves over the frequency range of 0-20 GHz for the MUTs used in Fig. 3. 16. (Reprinted from [7])

The values of $\Delta\phi$ and ΔMag for each chemical are related to its ϵ_r' and ϵ_r'', receptively, as discussed in Section II. On the other hand, the frequency dependent complex permittivity ($\epsilon_r^*(w) = \epsilon_r'(w) - j\epsilon_r''(w)$) is defined according to the Single-Debye (Cole-Cole) model for xylene, methanol and dmso, Double-Debye model for butanol and propanol, Debye-Γ model for ethanol, Davidson-Cole model for ethanediol, and the Polder-van Santen model for the binary mixtures composed of methanol and ethanol, respectively [3–6]. The proposed MBDS system is expected to characterize the frequency dependent complex permittivity of the MUTs within the range of $\epsilon_r^*(w)_{Air} \leq \epsilon_r^*(w)_{MUT} \leq \epsilon_r^*(w)_{Dmso}$ using measured values of $\Delta\phi$ and ΔMag versus frequency and a calibration method.

To understand the proposed calibration method, theoretical values of the ϵ_r' and the ϵ_r'' of each pure MUT are shown in Fig. 3.17 from 0-to-20 GHz, while measured results of the phase and magnitude differences with respect to theoretical permittivities are shown in Fig. 3.18. The theoretical curves show that $\Delta\phi$ and ΔMag are increasing nonlinearly with horizontal asymptotic behavior when ϵ_r' and ϵ_r'' are increased.

Although a good agreement between the VNA and the system measurement results is achieved as shown in Fig 3.16(a) and (b), measured $\Delta Mag_{,Dmso}$ is higher than methanol and ethanadiol at

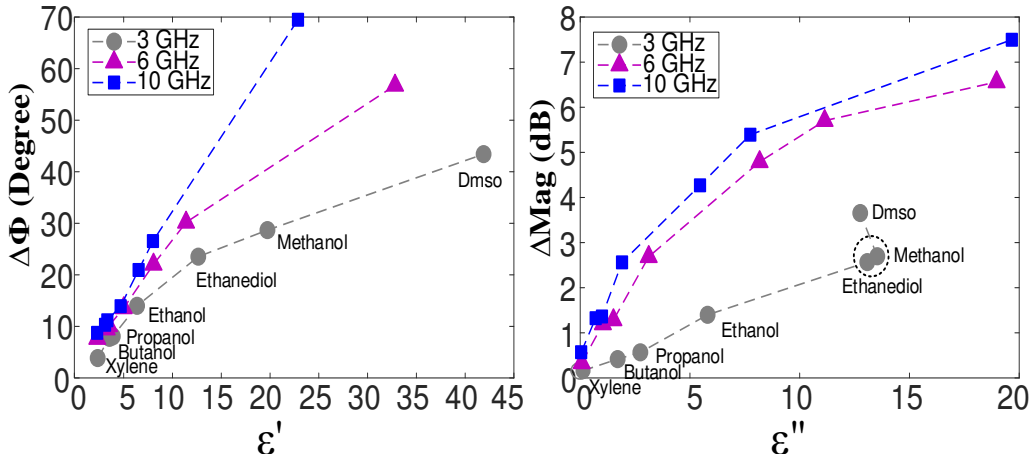

Figure 3.18: Measured $\Delta\phi$ and ΔMag as a function of theoretical ϵ_r' and ϵ_r'' at 3-6-and-10 GHz. (Reprinted from [7])

3 GHz (Fig. 3.18), however; according to the curves in Fig. 3.17, ϵ_r'' of ethanadiol (methanol) is higher than ϵ_r'' of dmso from 3-to-3.07 GHz (3-to-3.25 GHz).

This discrepancy results in calibration error as will be shown later. This effect might be due to contact-less sensing unit behavior around 3 GHz range. Furthermore, another source of the calibration error can be the temperature variations during the measurement since utilized models and their equations for the tested materials are chosen with the assumption that T $\sim 25^0$ C.

The calibration procedure is as following:

1) Reference materials (xylene, butanol, ethanol, methanol, and dmso) are first chosen to cover a wide range of complex permittivity values in the desired frequency range.

2) Since a reciprocal-curve fitting model will be result in the lowest root-mean-squared-error (RMSE) for an asymptotic curve when compared with other models [68, 69], in order to relate the measured ΔMag and $\Delta\phi$ to the complex permittivity of different MUTs, ΔMag and $\Delta\phi$ values of the reference MUTs are nonlinear-least-squared fitted to a reciprocal-quadratic-exponential model for ϵ_r' and a reciprocal-quadratic-power model for ϵ_r'', which experimentally result in the best fitting accuracy, respectively, using the following equations:

$$\epsilon_r' = \frac{1}{(a_1 * \exp(a_2 * \Delta\phi) + a_3 * \exp(a_4 * \Delta\phi)))} \tag{3.4}$$

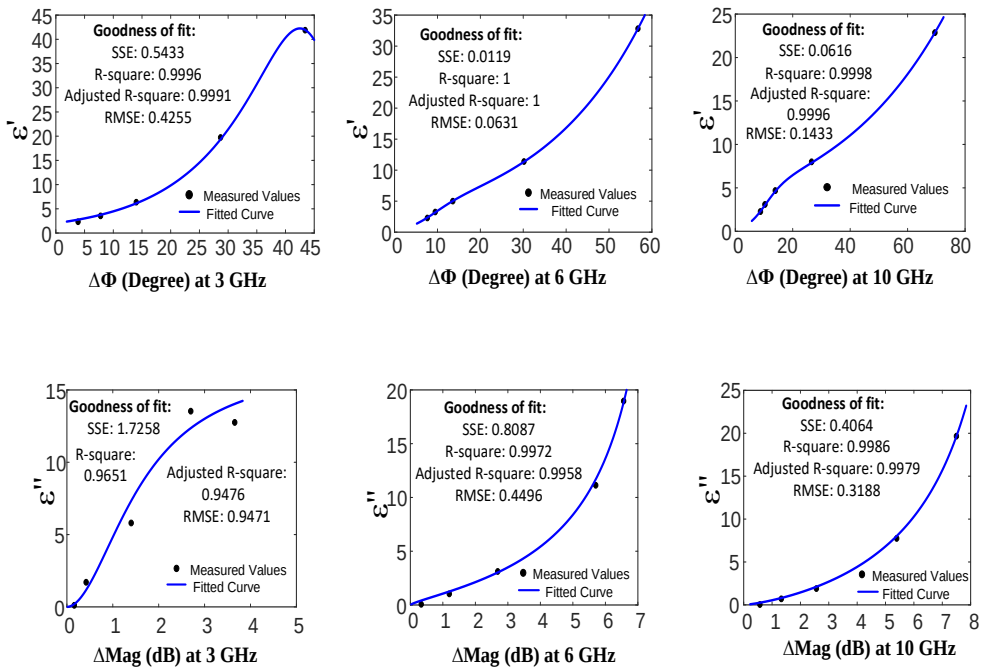

*SSE (Sum of Squares Due to Error): Total deviation from fit to data values, closer to "0" shows the model has a smaller random error.
*R-square: Indicates fit is how successfully explaining the data variation , closer to "1" verifies the model has a better fit.
*Adjusted R-square (Modified R-square): R-square based on the residual degrees of freedom depending on (number of response values – number of fitted coefficients) , closer to "1" shows a better fit.
*RMSE (Root Mean Squared Error): Differences between fit and data, fit standard error, closer to "0" means the fit has high accuracy to define the data.

Figure 3.19: Measured $\Delta\phi$ and ΔMag for the reference materials as a function of ϵ_r' and ϵ_r'' at 3-6-and-10 GHz, respectively, along with the fitted curves. (Reprinted from [7])

$$\epsilon_r'' = \frac{1}{(a_5 * \Delta Mag^{a_6} + a_7)} \tag{3.5}$$

where a_i, 1$\leq$ i $\leq$7, are the fit coefficients. This is illustrated in Fig. 3.19, where both the measured data (dots) and fitted curves (lines) for calibration materials at 3, 6, and 10 GHz are presented. According to the goodness of fit results, which verify how accurately utilized model fits the data [70], as shown in Fig. 3.19, the worst case RMSE is equal to 0.4255% at 3 GHz in ϵ_r' while it is 0.9471% at 3 GHz in ϵ_r''.

3) The measured values of ΔMag and $\Delta\phi$ for the reference materials are used along with the

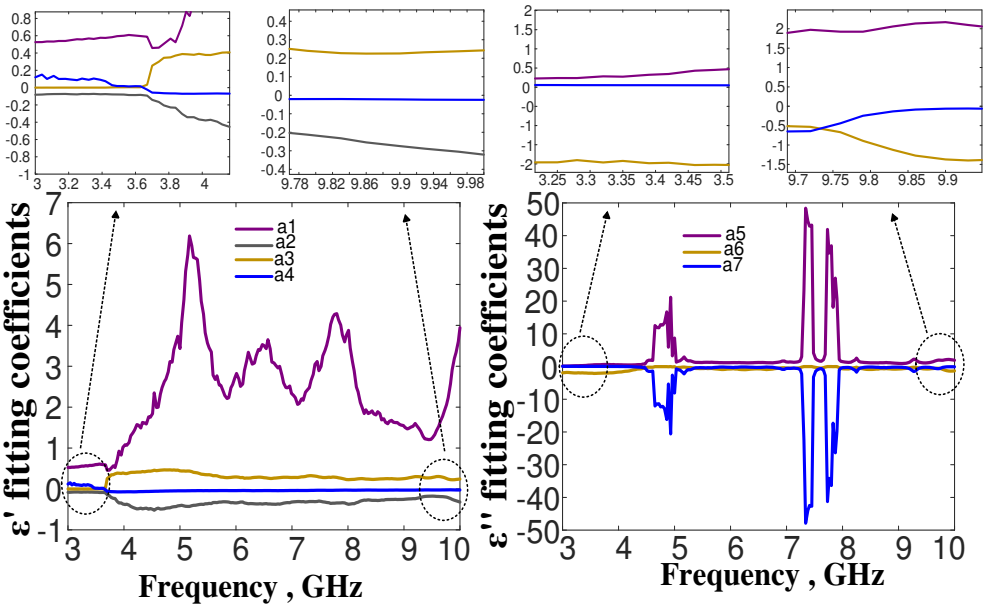

Figure 3.20: Coefficients of ϵ_r'-$\Delta\phi$ and ϵ_r''-ΔMag versus frequency. (Reprinted from [7])

theoretical values of ϵ_r' and ϵ_r'' to generate a database with the calculated fitting coefficients (a_i, i=1, ..., 7) covering the entire frequency range 3-10 GHz using (4) and (5). All of the curve fitting coefficients versus frequency are presented in Fig. 3.20. As can be seen, the coefficients $a_{2,3,4,6}$ are somehow independent of frequency while a_1 has a variance of 1.53 over the entire band. Furthermore, $a_{5,7}$ have sharp changes around 4-5 and 7-8 GHz where ΔMag values are getting closer (according to the sensor VNA results) for different MUTs. Therefore, characterization equations (4), (5) mostly depend on ΔMag and $\Delta\phi$ (hence ϵ_r' and ϵ_r'') of the MUTs through the frequency span rather than the coefficients, respectively, which shows the robustness and the reliability of the calibration method utilized to represent the $\epsilon_r^*(w)$ of MUTs.

To exemplify the overall behavioral model of the system, complex permittivies of the MUTs used in Fig. 3.16 are obtained utilizing the proposed calibration method with extracted coefficients from 3-to-10 GHz, and the results are illustrated as 3-D in Fig. 3.21. The RMSE for the materials (xylene, butanol, proponal, ethanol, ethanediol, methanol, and dmso) is 0.0801%, 0.0581%, 0.0597%, 0.0853%, 0.1478%, 0.1118%, and 0.0113% in ϵ_r', while it is 0.3632%, 0.2631%, 0.2557%,

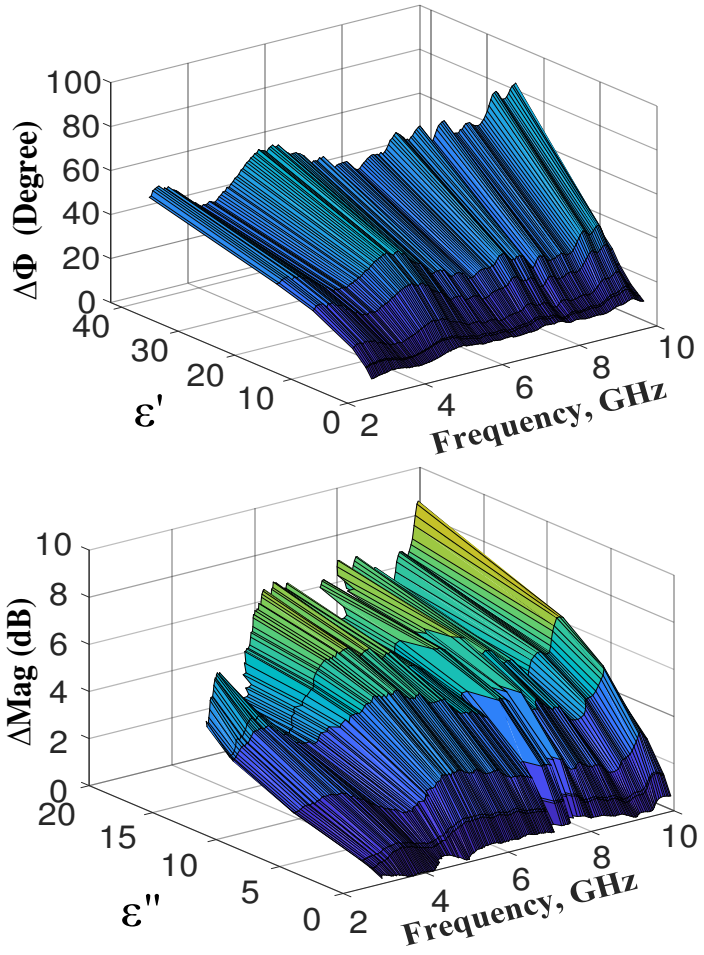

Figure 3.21: 3-D plots of the fitted curves, $\Delta\phi$ versus ϵ_r' and ΔMag versus ϵ_r'' with respect to frequency. (Reprinted from [7])

0.3437%, 0.4238%, 0.3525%, and 0.3047% in ϵ_r'', respectively. With the fitting coefficients stored in the database, the ϵ_r' and ϵ_r'' of acetone as an unknown MUT versus frequency is extracted using its measured ΔMag and $\Delta\phi$ values, and the results are shown in Fig. 3.22. For acetone, the RMSE is 0.1977% in ϵ_r' and 0.3138% in ϵ_r''. These results also indicate that the fitting coefficients have been evaluated fairly accurately.

Another goal for this system is to distinguish the mixture of two MUTs. Therefore, measured ΔMag and $\Delta\phi$ of the ethanol-methanol mixture with the mixing ratios q=0, 10, 20, ..., 90, 100% are used to map the ϵ_r' and ϵ_r'' of the mixtures utilizing the proposed curve fitting model with the

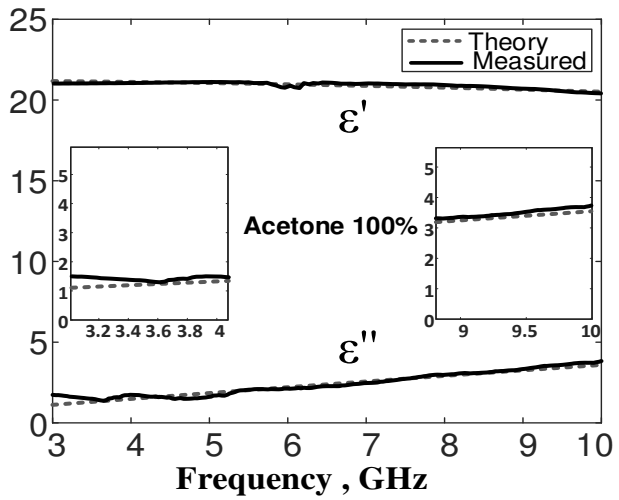

Figure 3.22: ϵ_r' and ϵ_r'' measurement versus frequency for acetone as unknown MUT. (Reprinted from [7])

stored coefficients, and the results are presented in Fig. 3.23. The ϵ_r' of the mixtures is achieved with worst case RMSE of 0.1729% while it is 0.3935% for ϵ_r''.

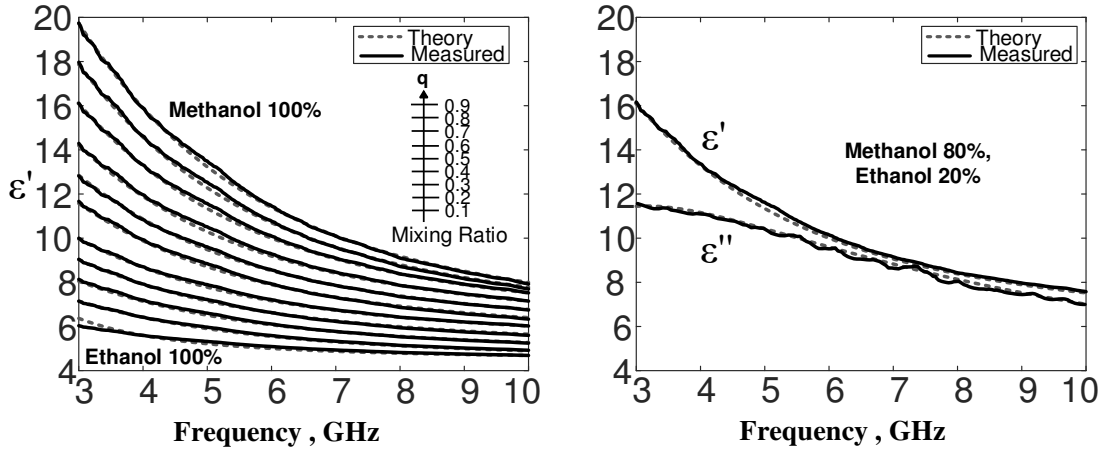

Figure 3.23: ϵ_r' and ϵ_r'' measurement versus frequency for ethanol and methanol mixtures with the mixing ratios q=0,10,...,100%. (Reprinted from [7])

Table 3.2: Performance Summary and Comparison with State of the Art (Reprinted from [7])

	This Work	[32]	[33]	[34]	[35]	[39]	[40]
CMOS Technology	65 nm	0.18 μm	65 nm	90 nm	0.35 μm	0.18 μm	65 nm
Architecture	Homodyne RF-Transceiver	Homodyne RF-receiver	Heterodyne RF-receiver	LC-Osc & PLL	Heterodyne RF-Transceiver	LC-Osc	Homodyne RF-receiver
Excitation Pulse	On-chip 1 GHz BW	Off-chip Single tone	Off-chip Single tone	Self-sustained	Self-sustained	Self-sustained	On-chip Single tone
Meas. Technique	TD	FD	FD	FD	FD	FD	FD
Freq. Range [GHz]	3 - 10	0.62 - 10	1 - 50	7 - 9	0.009 - 2.4	0.98 - 6	5 - 8
Sensing Element	Contact-less (Vivaldi-Antennas)	Contact-based, On-chip (2D Capacitor)	Contact-based, On-chip (T. Line)	Contact-based, On-chip (2D Capacitor)	Contact-based, Off-chip (3D Capacitor)	Contact-based, On-chip (2D Capacitor)	Contact-based, On-chip (T. Line)
Detection Capability	ϵ_r' , ϵ_r''	ϵ_r' , ϵ_r''	ϵ_r' , ϵ_r''	ϵ_r'	ϵ_r' , ϵ_r''	ϵ_r' , ϵ_r''	ϵ_r' , ϵ_r''
Permittivity Error ϵ_r'	RMS <0.2%	RMS <1%	($\lvert\Delta\epsilon_r/\epsilon_r\rvert$ for $\lvert\epsilon_r\rvert$=4.45) <1% @ 20 GHz	Max. 3.7%	RMS <0.7%	RMS <2% (1 - 6 GHz)	RMS <1%
ϵ_r''	RMS <0.4%	RMS <1%			RMS <1.5% (0.5 - 2.4 GHz)	RMS <5% (1- 3.8 GHz)	
Power [mW]	64 - 69	65 - 72	114	16.5	61 - 94	10 - 24	18
Area [mm^2]	1.68	9	1.2	6.25	10.89	6.24	1.68

Table 3.2 summarizes the specifications of the fabricated MBDS system and compares it with the prior published works. This comparison shows that this the first work done in TD with a dc-free homodyne transceiver based architecture as a CMOS MBDS system using a contact-less sensing unit, and resulting in a very high accuracy (RMSE of less than 0.2% for ϵ_r', and RMSE of less than 0.4% for ϵ_r'') with a small chip area. Note that the work can be converted to a self-sustained system if the required input signals (9.6 GHz, 5.8- 18.4 GHz) are provided by an on-chip frequency synthesizer.

3.6 Future Works for the Fully Integrated Contactless MBDS System

The work presented in this chapter focused on the miniaturization of the CMOS UWB MBDS system with a homodyne transceiver architecture for liquid material characterization and developing compact contactless sensing. This section briefly discusses the potential extension of the proposed miniaturization method for possible fully integrated applications.

3.6.1 Miniaturized Contactless Fully Integrated MBDS Platform

Fig.3.24 shows the block diagram of the possible contactless, fully integrated MBDS system, including; (1) the contactless sensing unit, (2) the MBDS chip including UWB transmitter (base-band pulse generator, polyphase filter network with buffers, SSB upconverter with differential to single-ended converter, and driver amplifier with matching network), UWB receiver (LNA with matching network, downconverter, lowpass filter, variable gain amplifier (VGA), analog signal splitter, and sub-Nyquist sampling ADC network), frequency synthesizer and the control unit, and (3) digital signal processing (DSP) unit with FPGA (Field Programmable Gate Array) for Fourier transform calculation.

The spectrometer chip can be connected to the off-chip sensing and DSP units. The 1 GHz BB pulse can be digitized using four sub-Nyquist sampling ADC units, each with 500 MS/s sampling rate. This procedure can be repeated for all ten microwave subbands by changing carrier frequency (f_0) using the frequency synthesizer unit, and the digital Fourier transform (DFT) results from all these subbands can be processed in the DSP unit to provide the complex permittivity signature of

the MUT versus frequency for 2.5-10.5 GHz range. In each frequency subband, a pulse train with proper delay can be submitted to be independently detectable for better accuracy. The detected results for all the pulses related to a particular subband can be averaged in the digital domain.

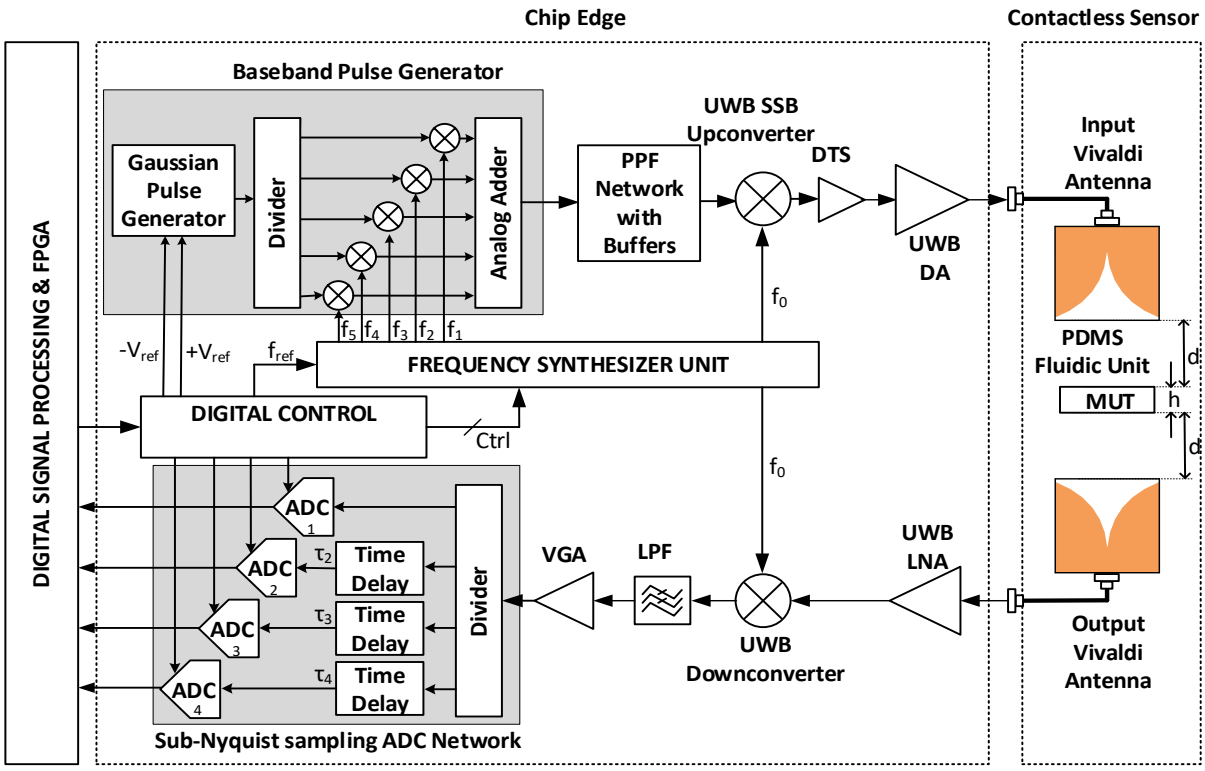

Figure 3.24: The block diagram of the possible contactless fully integrated MBSD system.

The BB pulse can be considered to be short enough to avoid interference due to multiple reflections inside the sensing unit and long enough to be digitized using a sub-Nyquist sampling ADC (4 ADCs with at least 500 Msp/s sampling rate for 1 GHz BW BB pulse).

As explained previously, the upconversion mixer in the transmitter path is designed as an SSB mixer since the signal spectra do not carry exactly the same information on both sides of the carrier; in other words, the signal becomes its own image because of the dispersive characteristic of the materials. Furthermore, when the signal is downconverted to 500MHz, the asymmetric

signal spectrum causes corruption at lower frequencies. Another solution to overcome this issue is to use different LO frequencies for the up/down converter resulting in more complex system architecture. The self-corruption of asymmetric signal effects will be prevented by using reduced lower-sideband suppression, resulting in system performance-reliability enhancement. Besides, one LO for transmitter and receiver will be used. The microwave frequency span of 2.5 – 10.5 GHz can be divided into ten subbands with LO frequencies of 2.4, 3.2, 4, 4.8, 5.6, 6.4, 7.2, 8, 8.8, and 9.6 GHz instead of 9 subcarriers to have integer divider units rather than fractional dividers. This can provide a more simplified frequency synthesizer architecture while resulting in a wider frequency application span with 8 GHz BW instead of 7 GHz one.

Sub-Nyquist Sampling ADC: To digitize a wideband signal of 2.5-10.5 GHz according to the Nyquist theorem, at least 16 GS/s sampling rate is needed, which is not feasible with the current state-of-the-art CMOS ADCs if at least 12-bit resolution is required. The state-of-the-art CMOS ADC performance is limited to 10-bit resolution with a sampling rate of 5 GS/s [71]. This is the main reason to break the 3-10 GHz bandwidth into 1 GHz sub-bands. As a result, the sub-Nyquist sampling approach is proposed [72,73]. With the sub-Nyquist sampling method, a wideband signal will be sampled with a lower rate than the Nyquist rate. It will acquire the broadband signal using relatively few sampled measurements. In other words, 1 GHz signal will be reconstructed with a few measurements using digital signal processing. The proposed sub-Nyquist sampling rate will be 500 MS/s for 1GHz signal BW for each ADC. To implement this ADC, first, the receiver will divide the down-converted signal into four branches with a signal divider in the time domain and then performs the signal digitization with 500 MS/s-12 bit ADCs. To reconstruct a true 1 GHz BW signal [74], an effective sampling rate of 2GHz is achieved by using four parallel ADCs (SAR ADCs with time interleaving [75] or pipeline/SAR ADCs [71]) with 500 MS/s sampling rate with time delays τ_2=0.5ns, τ_3=1.0ns, τ_4=1.5ns) illustrated in Fig.3.24. According to the state-of-the-art, a 12 bit 1.6 GS/s is already implemented with 65 nm CMOS technology [75].

3.6.2 On-chip Wideband Frequency Generation

An integer two-stage phase-locked loop (PLL) architecture (1.6-11.2 GHz) can be used for the frequency synthesizer illustrated in Fig.3.25. The channel spacing in MBDS can be separated by 800MHz. Due to large channel spacing, the reference frequency should be much higher than in conventional frequency synthesizers. A two-step PLL approach can be proposed to achieve low jitter and fast settling time. In this approach, the first PLL not only can generate the baseband carrier frequencies (160-320-480-640-800 MHz) using divide by 1/2/5/10 and two SSB mixers but also can provide a reference frequency (800 MHz) to the second PLL, which can generate the carrier frequencies (2.4-9.6 GHz) for UWB spectroscopy transceiver. The reference frequency to the first PLL can be obtained from a 100 MHz crystal oscillator. The bandwidth of the first PLL can be kept low ($\sim$500 KHz) to provide a high spectral purity reference frequency (800 MHz) to the second PLL to achieve low jitter and not degrade the TX and RX sensitivity. The bandwidth of the second PLL should be set higher ($\sim$80 MHz) to suppress VCO phase noise. To keep the loop stable and have a fast settling time, the bandwidth of the second loop should be at least 1/10th of the reference frequency. Finally, the high reference frequency for the second PLL can enable a low divide ratio (N= 8-14), reducing in-band phase noise [76]. To minimize the tank inductance and the chip area, an LC-VCO can be used to work at 6.4-11.2 GHz range for the second PLL, reducing the frequency synthesizer design complexity. Quadrature phases for UWB SSB upconverter can be generated by low power inductorless injection locking dividers, dividing by 1/2/4 output of the second PLL frequency [77]. The injection locked dividers are based on differential ring oscillator topology, thereby achieving superior phase noise and wide divide range, requiring no calibration or tuning circuitry. Quadrature phase generation can use an injection locking scheme because the polyphase filter is lossy. furthermore, QVCOs (quadrature VCOs) have limitations in terms of the trade-off between phase noise and accuracy of the quadrature sequence and occupy a large area because of LC tanks. Both quadrature VCO and polyphase filter are prone to I/Q mismatch, which can be alleviated by using ring oscillator injection locking dividers. A tri-state buffer can be used to select the carrier frequency for the LO inputs of the up/down conversion mixers.

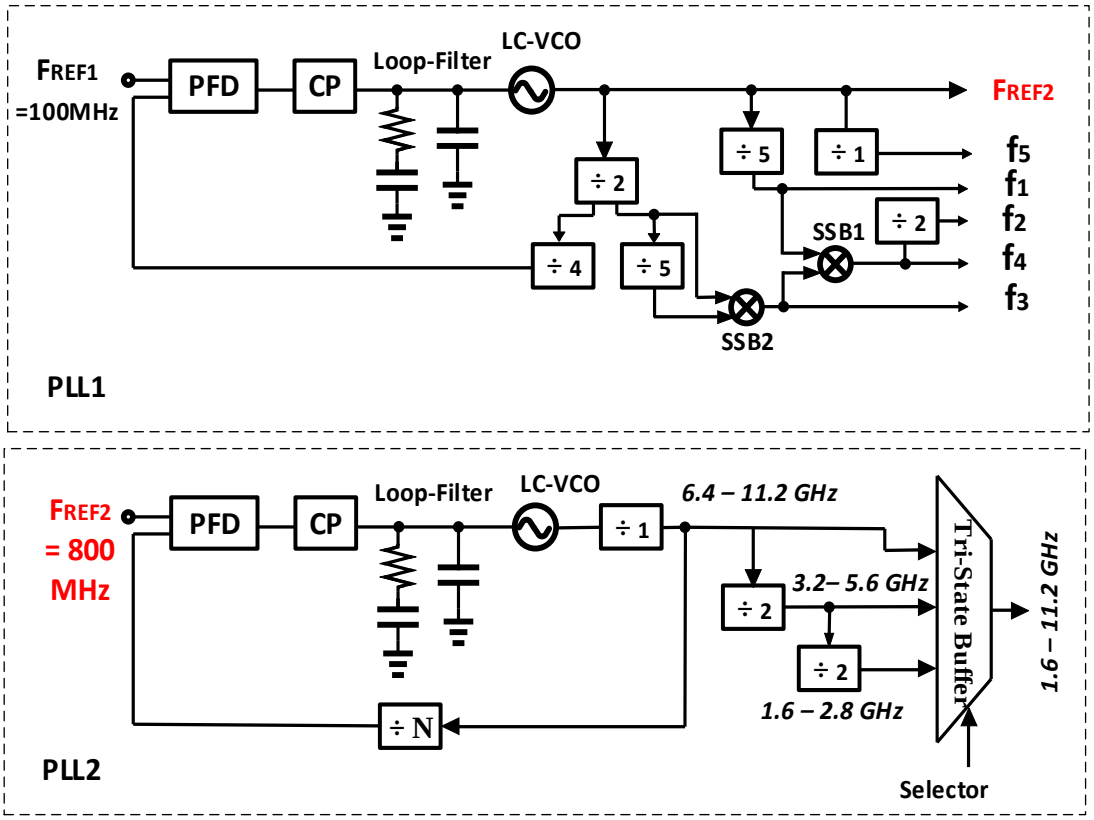

Figure 3.25: The block diagram of the possible frequency synthesizer for a self-sustained fully integrated MBSD system.

4. A CMOS MICROWAVE UWB ADAPTIVE DUAL-COMB DIELECTRIC SPECTROSCOPY SYSTEM

4.1 Introduction

Complex[1][2] relative permittivity, ($\epsilon_r^* = \epsilon_r' - j\epsilon_r''$), which is one of the electromagnetic properties of materials, can vary with frequency from lower than 1 mHz up to sub-THz ranges depending on molecular structure of material. Microwave broadband dielectric spectroscopy (MBDS) systems, which utilize different techniques to sense the complex relative permittivity as a unique response to an external microwave electric field, characterize the frequency spectral features of materials under test (MUTs) for a wide variety of applications in chemical, biological, medical, oil exploration, bio-threat detection, safety, imaging, and agriculture fields [8, 9, 28]. MBDS systems, which have attracted significant attention due to their nondestructive, label-free, rapid and real-time accurate characterization capabilities, can achieve low-cost, low power consumption, and integration with digital integrated circuits (ICs), resulting in a fully integrated system for lab-on-chip applications.

To precisely extract the comprehensive complex relative permittivity information utilizing the broad microwave frequency range, the realization of an MBDS system that has high discrimination ability between different MUTs is highly desirable. Rather than frequency sweep methods (frequency-domain (FD) MBDS) [8, 9], time-domain (TD) MBDS is a powerful high-speed measurement technique for investigating the dielectric properties of MUTs [14, 78–82]. In this approach, an excitation pulse with a short period in time domain first excites the sensing unit loaded with an MUT. Then, either a transmitted or reflected signal through from the MUT is captured in TD and converted into the frequency-domain using the Fourier transform. This process results in a complex transmission/reflection function that shows the magnitude and phase variations of

[1]* ©2020 IEEE. Parts of this section, Part of this section is reprinted with permission from "A CMOS Microwave Broadband Adaptive Dual-Comb Dielectric Spectroscopy System for Liquid Chemical Detection" E. Kaya and K. Entesari, IEEE MTT-S Int. Microw. Symp. Dig., pp. 229-232, Aug. 2020.

[2]* ©2022 IEEE. Parts of this section, Part of this section is reprinted with permission from "Silicon Integrated Broadband Dual Frequency Comb-based Microwave Detector for Material Characterization" E. Kaya and K. Entesari, IEEE Radio and Wireless Symposium (RWS), Dig., pp. 79-82, Jan. 2022.

the exciting signal as a representation of the MUT's dispersive (ϵ_r') and dissipation (ϵ_r'') properties. FD techniques utilize a monochromatic signal sweep while the TD technique measures the spectroscopic signature of the MUT that contains all the frequencies. Namely, the FD techniques provide the complete dielectric spectrum thanks to the entire frequency range sweep, while the TD technique ensures all data collection in a wide frequency range during a single measurement observation. On the other hand, the information content will be eventually the same in either domain.

Traditional MBDS systems that utilize either FD or TD techniques are proven to provide high resolution and accuracy for material characterization. On the other hand, their use for MBDS systems is hindered since they are in need of bulky and expensive equipment such as external vector network analyzers (VNA), high-frequency arbitrary waveform generators (AWG), or high-speed digital oscilloscopes. In other words, they are limited by high power and cost, the large size of the measurement setup, and excessive volume of the MUT [30].

Fortunately, due to the recent advances in current CMOS technologies, the realization of fully integrated, portable, and cost-effective MBDS systems has become feasible. Two silicon-based methods for detecting the complex permittivity have been reported in literature, which utilize only the FD measurement techniques: 1) voltage-controlled oscillator (VCO)/phaselocked loop (PLL) based [34, 35] and 2) RF receiver (RX) based [32, 33] topologies, and both are in direct contact with either an on-chip or an off-chip sensor. Although RF RX-based systems have been proven to provide high accuracy and detection of both real and imaginary parts of the permittivity over a broadband frequency span, power consumption is high as they entail a single tone signal generator that utilizes a broadband sweep. Besides, they are subject to flicker noise and dc-offset limitations [32]. Contrariwise, VCO/PLL-based systems are self-sustained, more accurate, and power-efficient while their use for broadband dielectric spectroscopy is hampered due to their narrow-band nature. One remedy is to use the VCO/PLL-based systems in a tunable architecture such as a wideband low-power low-noise LC digitally controlled oscillator (DCO) [39]. However, achieving a high detection accuracy is still a challenge.

Recently, a miniaturized CMOS TD MBDS system, which utilizes a contact-less sensing unit along with a homodyne dc-free RF transceiver architecture has been presented in [7,83]. Although the system offers significant miniaturization, to identify the complex permittivity of MUTs, it requires separate measurements for 9 sub-carriers within the 7 GHz frequency bandwidth (BW) from 3 to 10 GHz. Hence, it potentially requires an on-chip analog-to-digital converter (ADC) with at least 2 GHz BW resulting in large power consumption and chip area. Therefore, for a comprehensive and high precision measurement, a digital sampling oscilloscope might be required which again results in an expensive and large test setup.

Dual-comb spectroscopy (DCS) is a powerful and an appealing TD technique that has been used in broadband optical spectroscopy systems for material characterizations [84–88]. DCS can be a desirable method in MBDS systems, since it enables integrated architectures, real-time characterization, and self-sustained implementation as a stand-alone operation without the need for any external equipment resulting in a portable and a low-cost system with high-precision [89,90]. A DCS system for MBDS has been implemented in board level [91], which requires two signal sources to generate frequency-combs while it needs another AWG to trigger an oscilloscope with a signal equal to the difference of the repetition rates of the two combs. Although the system uses the 10-MHz output port of a VNA to phase lock the other equipment, the time fluctuations between the comb lines decreases the accuracy. Furthermore, using another AWG for trigger signal rather than frequency-comb generators will cause some time discrepancies. Finally, to caliber out the system effects, this implementation requires an off-chip calibration such as subtraction of both phase and magnitude of the air [18,19] measurement from other MUTs' measurement results.

This project presents an integrated TD CMOS adaptive microwave DCS system to measure the response of different MUTs to a transmitted signal within 3–10 GHz frequency range to distinguish the complex permittivity of unknown materials with high accuracy. Two on-chip microwave frequency-combs with slightly different repetition rates are passed through reference and sensing units, respectively, and then interrogated with a heterodyne UWB mixer to map the broadband microwave information of MUT's complex permittivity loading the sensing unit to the low frequency

intermediate frequencies (IF) which eliminates the requirement of a high-speed oscilloscope or an ADC to capture the data. The entire TD DCS system might have some intrinsic distortions and instabilities during the transmission of the signal and its detection in the sampler. In addition, in a DCS system, there are time fluctuations for the time intervals between the two interfering frequency-combs and phase difference relative to the pulse envelope between the two frequency-combs. These downsides of the DCS systems will significantly degrade the spectrum, reduce signal-to-noise ratio (SNR), and cause false measurement results [92–95]. In order to overcome these issues inherent in DCS systems for the accurate construction of MUT's complex permittivity, two on-chip frequency combs, a 10-MHz reference frequency, and adaptive signals (AS_1, AS_2) for phase and time correction are generated through only one external single reference input (f_{in}). Also by using two on-chip identical sensors, one as a reference (air) and the other containing the sample of interest embedded into two frequency-comb paths, rapid and accurate differential calibration has become feasible. Eventually, comparing the proposed system with the reported board level architecture, the proposed homodyne dc-free microwave DCS system is entirely stabilized and phase locked along with an on-chip system calibration for phase and envelope correction. In other words, due to the highly resolved comb lines and distortion-free spectra, SNR will be improved while the measurement time will be shorter [96–98].

As a proof of concept, this system was first demonstrated in [99] using 65 nm CMOS technology. In this chapter, a more in-depth system analysis and the circuit implementation of different building blocks of the proposed microwave CMOS DCS system are presented. In addition, more insight into electrical and chemical performance are provided.

4.2 UWB Adaptive DCS System Design and Sensing Unit

This section first presents overall system analysis, then discusses the detailed sensing element design and operation, and explains the circuitry interface architecture of the proposed microwave DCS system.

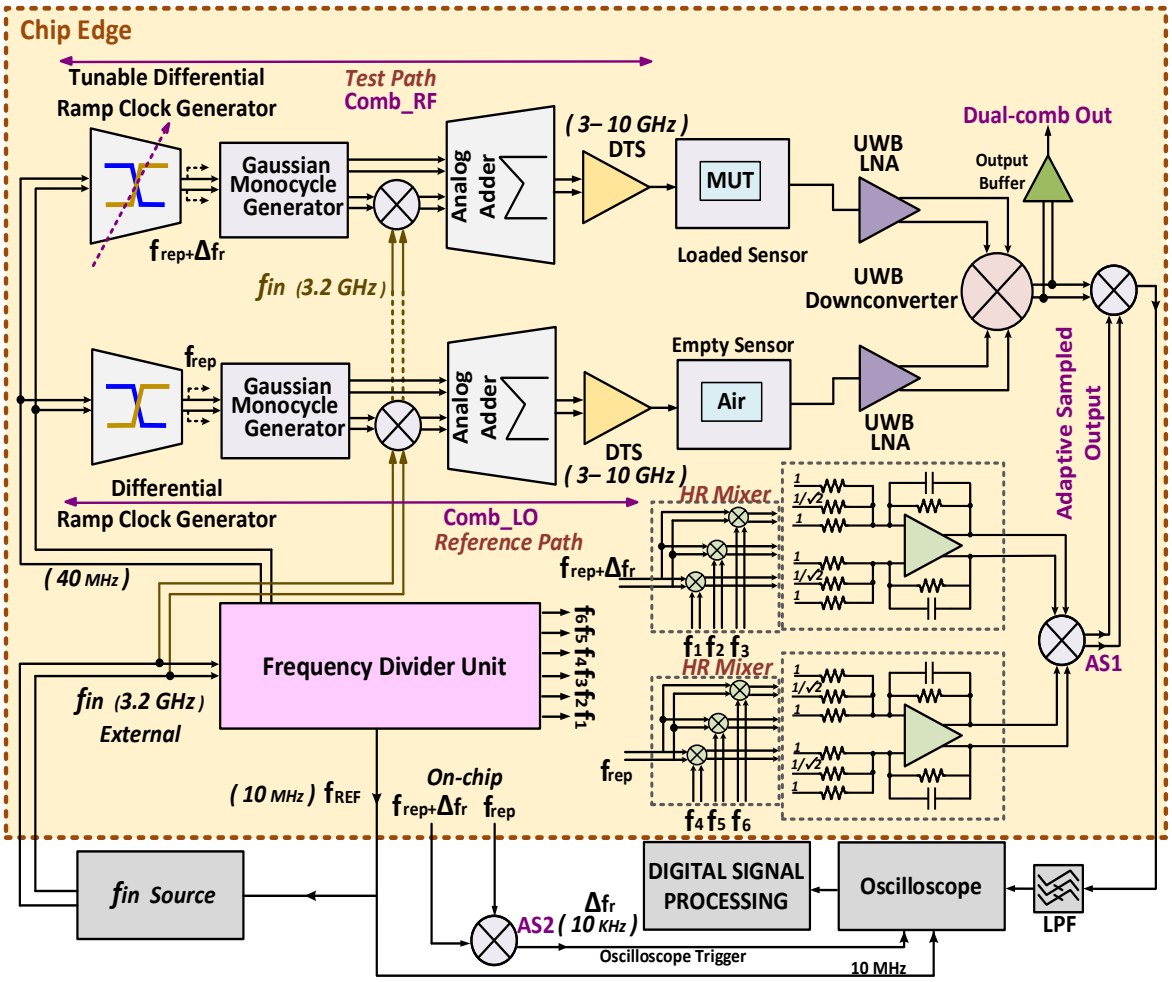

Figure 4.1: Block diagram of the proposed microwave broadband DCS system. (Reprinted from [99])

4.2.1 Overall UWB Adaptive DCS System Architecture:

The proposed system utilizes four main approaches to expel the known main challenges of the comb-based systems which are discussed earlier: 1) two on-chip frequency combs and a 10 MHz reference signal are generated through an input reference clock (f_{in}), thus, beat notes along with all comb tones are stabilized and all external devices involved in the system are phase locked, 2) two on-chip adaptive signals (AS_1 and AS_2) are executed, thereby, real-time on-chip phase and time error correction is achieved, 3) two on-chip identical sensors for both frequency combs are implemented, hence, equal delay between two paths along with an on-chip phase and magnitude

system calibration is utilized, and 4) an on-chip UWB excitation pulse with a uniform spectrum along with a linear phase change within the desired frequency span is generated, so that the dissipation factor of MUT (ϵ_r'') using the magnitude change (ΔMag) and the dispersive property of MUT (ϵ_r') using the phase change ($\Delta\phi$) of the captured adaptive sampled dual-comb system output are precisely characterized.

Fig.4.1 shows the complete conceptual block diagram of the proposed DCS system. The proposed integrated TD DCS system mainly composes of four essential parts: 1) frequency combs generator unit, 2) sensing unit, 3) UWB amplification and down conversion along with baseband (BB) adaptive sampling unit, and 4) frequency divider unit.

The frequency combs generator unit basically consists of two combs ($Comb_{RF}$ and $Comb_{LO}$) along with a tunable offset frequency (Δf_r) and slightly different pulse repetition frequencies f_{rep} and f_{rep}+Δf_r, where (f_{rep}= 40 MHz, Δf_r= 10 KHz and hence f_{rep}+Δf_r= 40.01 MHz, respectively. The main concept underlying the design of on-chip tunable frequency combs references to an external source (f_{in}=3.2 GHz) is generating simultaneously both combs on the same chip from a single source to synchronize the pulse trains of two combs. In other words, utilizing a single feeding source for the proposed system, the mutual coherence between two combs is achieved. The sensing signals are provided merging two on-chip monocycle Gaussian pulses; while a set of frequency dividers are used to produce an internal square-wave reference clock (f_{rep}) that determines the repetition rate of generated pulses through the external source for differential ramp generators of which output is the main input of the Gaussian first derivative pulse generators.

For sensing unit that is composed of two identical sensors, GSSG coplanar waveguide (CPW) transmission lines are used due to their broadband nature. The $Comb_{LO}$ is passed through the reference sensor (unloaded=air), while the $Comb_{RF}$ interrogates the test sensor (loaded=MUT), afterward which conveys the microwave constitutional properties of the MUT.

Then, both attenuated frequency combs, reference and radiated test one, are amplified using two UWB low noise amplifiers (LNA) for the proceeding mixer stage while the amplification is kept at a level sufficiently below the 1-dB compression point of downconverter. The heterodyne detection

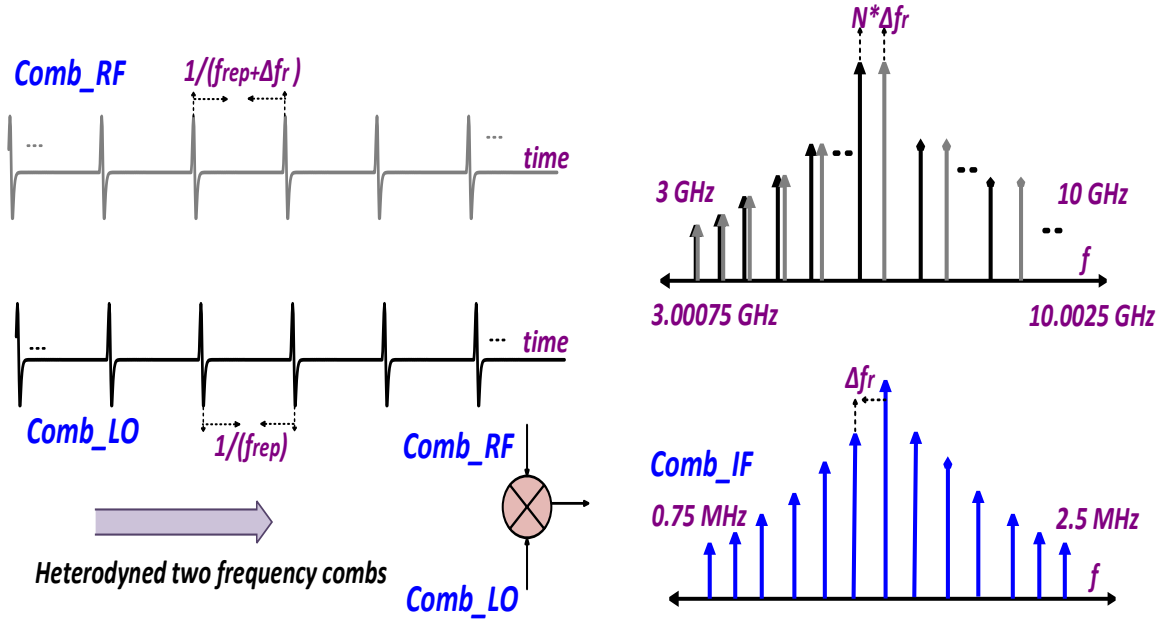

Figure 4.2: DCS system combs in TD and FD. (Reprinted from [99])

is performed using an active UWB mixer which coherently downconvertes microwave signals to low-frequency IF baseband comb uniquely corresponding one of the tones in the $Comb_{RF}$. IF comb teeth are sampled every 1/ f_{rep}= 25 ns and repeated with the period of 1/Δf_r= 0.1 ms.

For adaptive sampling, to generate the first adaptive clock AS_1 on-chip through both combs, harmonic rejection mixer (HRM) with third and fifth harmonic suppression is used while gain scaling is utilized to increase the harmonic rejection along with alleviation of the gain mismatch. It is used to upconvert the BB interferograms to compensate the phase variations on-chip. On the other hand, for the second adaptive clock AS_2 (=Δf_r) is generated by mixing two on-chip frequency combs via an off-chip low frequency mixer which is used as an external clock to trigger data acquisition device to provide restitution for time variations [96]. Eventually, all the proposed approaches make the setup insensitive to phase and time errors.

The frequency divider unit including both true single-phaseclock (TSPC) frequency dividers and current-mode-logic (CML) frequency dividers provides the required reference clock (f_{rep}) for combs generation and LO frequencies for HRM.

Fig.4.2 shows the conceptual principles of the DCS systems' both comb pulse trains in the TD and frequency domain (FD), respectively. The pulse reputation rate between BB IF comb trains is equal to Δf_r. Due to the periodic input signal, the output signal of the UWB comb generator is sampled by the input pulse reputation frequency within the operation frequency range 3-10 GHz.

The desired microwave BW (Δ_v= 7 GHz) is mapped to 0.75-2.5 MHz spectrum with 1.75 MHz IF BW, while utilizing 175 number of comb lines within 3-10 GHz frequency range resulting in a compression factor, m (=$f_{rep}/\Delta f_r$) of 4000, and satisfies the constraint, ($\Delta_v \leq \mathrm{m} f_{rep}/2 = f_{rep}^2/2\Delta f_r$) for successful one-to-one mapping from RF comb to IF comb.

After a low pass-filter (LPF), a low frequency oscilloscope is used to capture the adaptive sampled DCS output in TD, and then, data are imported to MATLAB for characterization of the complex permittivity of the MUT.

4.3 Sensor Design

The complex relative permittivity $\epsilon_r^* = \epsilon_r' - j\epsilon_r''$ is a unique subscription of materials over frequency, which is a fundamental parameter that effects the propagation of electric fields and describes how electric field behaves or interacts with any material (liquid/solid). A transmitted or reflected signal through the MUT can give complex permittivity of material over frequency. Real relative permittivity ϵ_r' indicates how much energy from an external electric field is stored by the MUT, while imaginary relative permittivity ϵ_r'' indicates how lossy the MUT is to an external electric field. By measuring the dielectric spectra response of the MUT, we can relate the effect of structure influencing its dielectric properties on the amplitude and phase of the transmitted signal through the MUT to define its dispersive and dissipation characteristics.

On-chip sensors for the description of substances are ordinarily planar and implemented utilizing metallization and dielectric multilayers at the back end of line (BEOL) of a silicon process. Chip-level sensors actualizations can be lumped such as interdigitated capacitor [32, 39] or transmission-line (TL) based architecture [33] achieving broadband material sensing when the MUT interacts the electric field inside the planar sensor. In addition, the electrical parameters of the planar TL sensor will change when a dielectric sample placed on it that is highly dependent on

permittivity of the MUT since when the MUT is loaded on the signal strip, properties of TL, such as characteristic impedance, phase velocity, losses, and quality factor will change with the dielectric constant, loss tangent (ratio between dielectric constant (ϵ_r') and loss factor (ϵ_r'')), volume, and thickness of the MUT [26].

Compared to microstrip line, frequency variation of the effective permittivity of coplanar waveguide (CPW) line is lower [100]; therefore, CPW line achieves broadband circuit application while amplitude or phase changes of the signal line will reflect the MUT effects rather than the TL itself for wide frequency range material characterization. The electromagnetic wave (EM) propagates on the surface of the signal conductor along the TL [101], consequently, CPW coefficient S_{21} parameters (phase and magnitude) will be used for the sensing mechanism with varying different MUTs. To keep the electric fields concentrated around signal lines [102], an on-chip CPW planar transmission line sensor is based on a grounded CPW (GCPW) line implemented using TSMC 65-nm CMOS process as shown in Fig. 4.3 (a), (b), and (c). A ground–signal–signal–ground (GSSG) CPW line [103] provides sufficient matching ($S_{11} <$ -10 dB) and flat group delay over the entire UWB band. S_{11} simulation results for different materials which show the dynamic range of the proposed sensing unit are shown in Fig. 4.4 To isolate the CPW signal lines from the lossy substrate and reduce the eddy current losses in the substrate [104], slow-wave CPW (S-CPW) line structure has slotted floating strip shield below the signal strips' metal layer is used as depicted in Fig. 4.3 (b) and (c). Furthermore, coplanar waveguide that has finite width ground planes (FGC) is utilized because it is electrically small in terms of total width of TL and permits smaller layouts, has low attenuation, low dispersion, low coupling, and no parasitic resonances [100].

High frequency lines can be characterized with their resistance, transmission, and wave effects, while these effects can be leveraged by the line geometries and the surrounding materials. In addition, fringing fields from the direction of the center signal lines terminate with adjacent grounds, and hence they might be changed by the surrounding materials too. In most of the existing integrated sensing units, MUTs are in direct contact with the signal lines, which can deteriorate the lifetime of the sensor. A novel approach is utilized for the sensing unit here to avoid direct contact

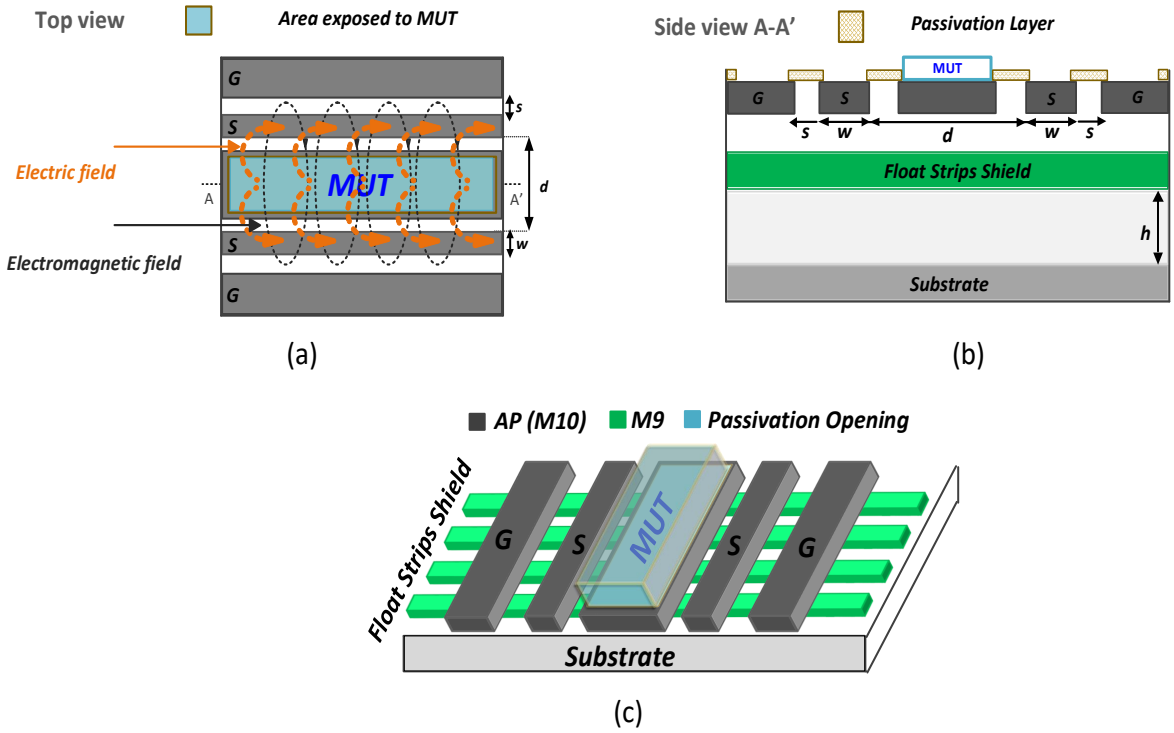

Figure 4.3: Proposed sensing unit conceptual structure and MUT loaded case (strips are not shown), (a) and (b) top and side views, and (c) 3D layout of the S-CPW sensor, respectively.(Reprinted from [90,99])

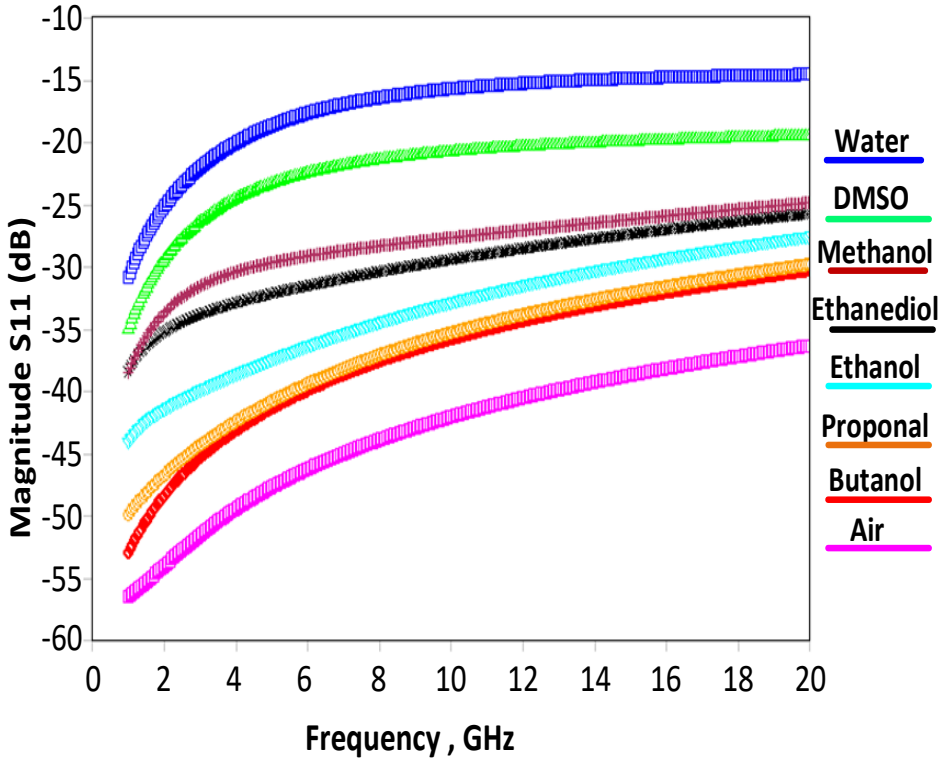

Figure 4.4: S_{11} simulated magnitude results of the loaded sensor with different MUTs.

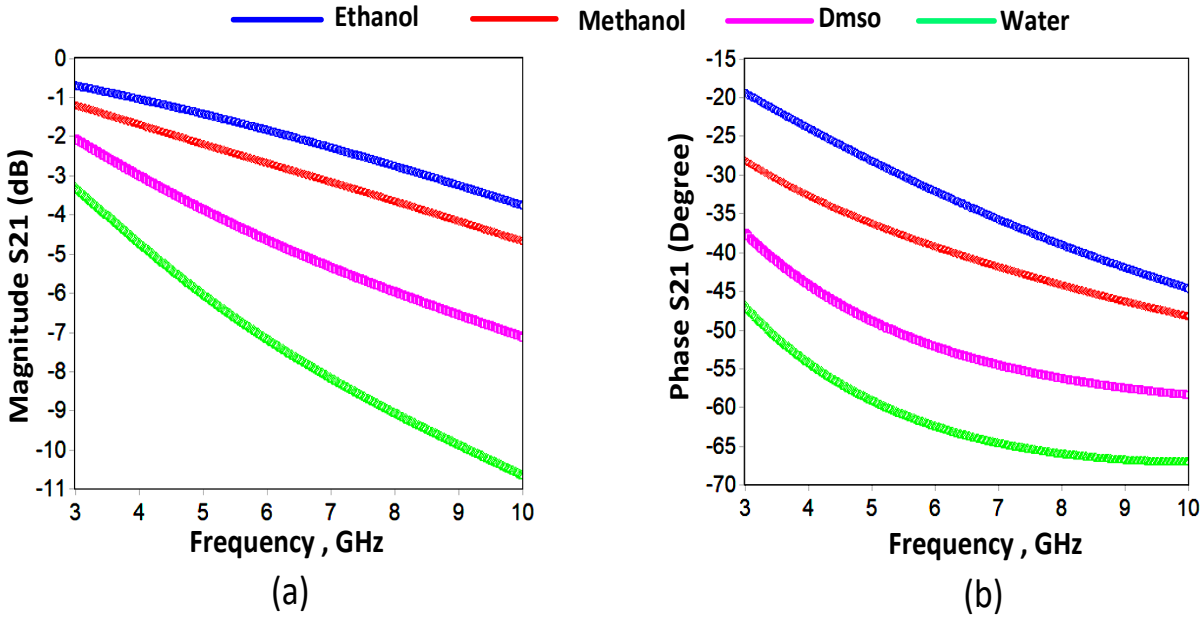

Figure 4.5: S_{21} simulated magnitude (a) and phase (b) results of the loaded sensor with different MUTs. (Reprinted from [90])

of MUT with the signal lines and address this issue (shown in Fig. 4.3 (a)). A floating open-ended line is placed in between two signal lines with equal spacing, and both signal lines are combined in a way that work as a power splitter and combiner while both sides are terminated with a proper impedance for 50 Ω matching at the output of differential to single (DTS) ended converters and LNA inputs (see Fig. 4.1 and Fig. 4.6). Furthermore, since both side of the CPW lines carry the same signal polarity, here is an electromagnetic field with the same direction covering both signal lines. Therefore, the open-floating line is used as a sensing unit loaded with different materials. Due to the restrictions of the CMOS 65 nm fabrication, only second passivation layer is removed using the pad-open layer so that CPW line is designed using the top thickest metal (AP) layer with floating shield slots on the lower metal layer (M9) as shown in Fig. 4.3 (c). By removing the passivation layer, the MUT is in close proximity to both signal lines, thus increasing the sensor sensitivity, while not in direct contact with the signal lines and improving the sensor lifetime. Both the magnitude and phase of a microwave signal passing through the signal lines of the CPW sensor are changed due to the dielectric properties of different MUTs located in between the two signal lines, as illustrated in Fig. 4. 3 (a). This effect can be used to characterize the dielectric properties of an unknown MUT. Fig. 4.5 (a) and (b) represent the magnitude and phase simulation results of the sensor loaded by different MUTs. In addition, sensing floating line will also increase the isolation against the crosstalk of signals. Furthermore, during layout, triple guardring is implemented at both sides of each ground of the S-CPW lines to decrease the coupling effects between the test and reference paths.

4.4 Circuit Implementation

Fig. 4.6 and Fig. 4.7 show the circuit schematic of the proposed integrated DCS system. One of the main goals is to implement an on-chip tunable offset frequency (Δf_r) to have a control on the comb spacing; therefore, while generating the differential ramp input for the test path, 40 MHz reference signal is passed through an inverter oscillator with a tunable capacitor (C_{Tune}), to generate f_{rep}+Δf_r (RF comb) according to f=1/(1.1$R_{T1}C_{Tune}$).

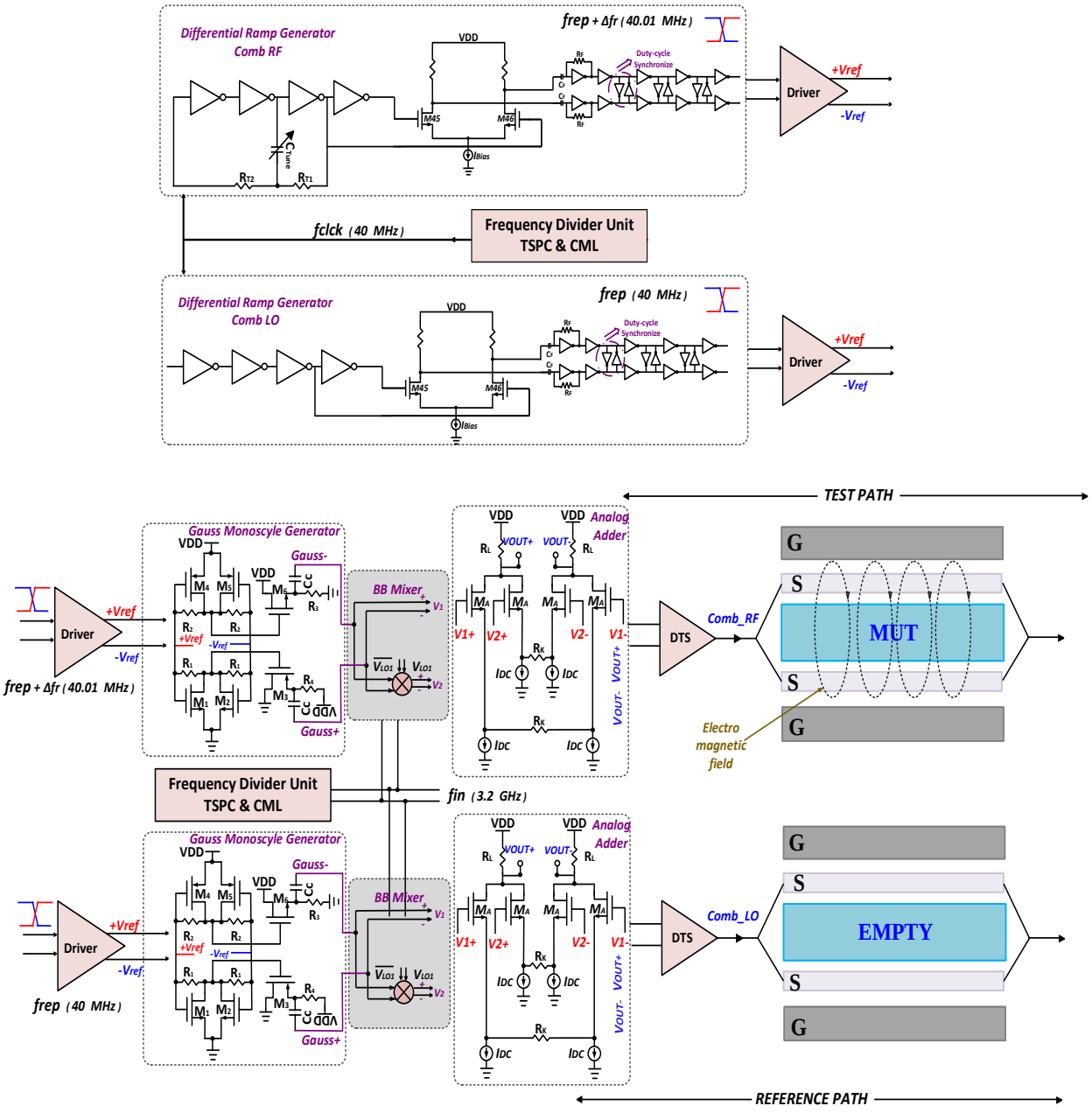

Figure 4.6: Circuit schematic of the proposed DCS system. (Reprinted from [99])

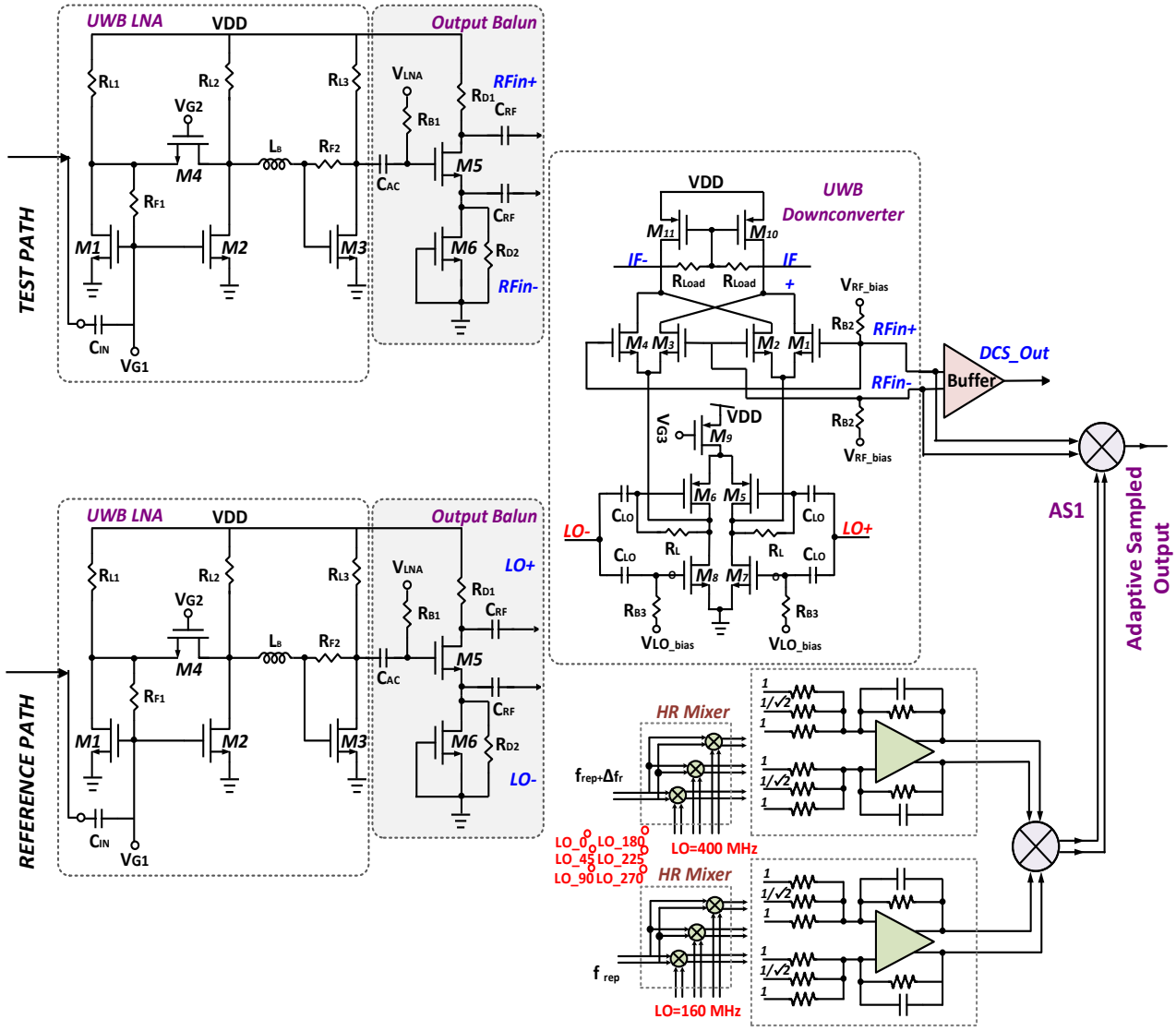

Figure 4.7: (Continue of Fig.4.6) Circuit schematic of the proposed DCS system. (Reprinted from [99])

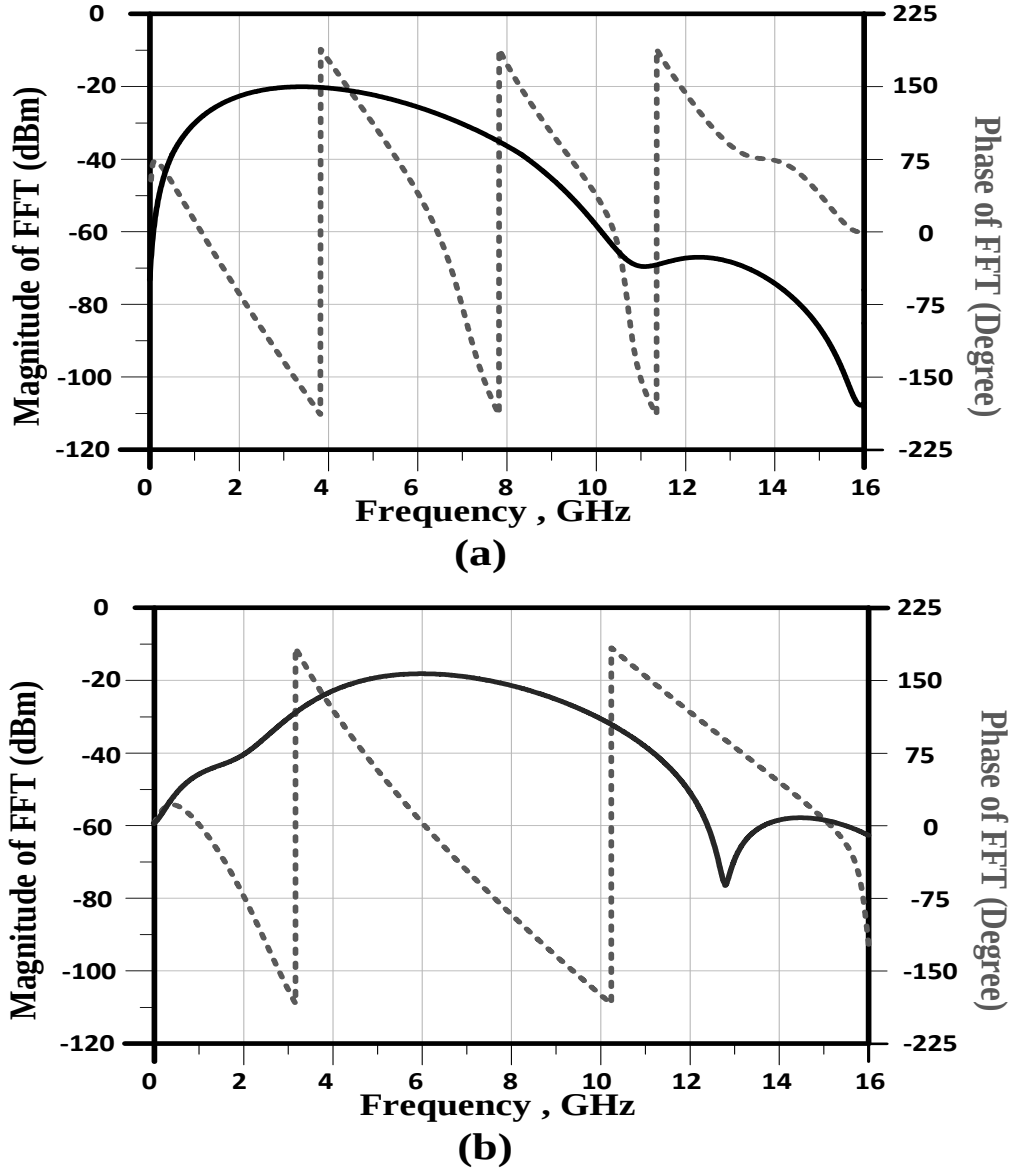

Figure 4.8: (a) Generated Gaussian monopulse in FD, and (b) generated on-chip UWB pulse in FD, respectively. (Reprinted from [99])

The required 40 MHz f_{REF} differential ramp generator is generated through an on-chip frequency divider unit using an external signal f_{in}= 3.2 GHz. For the low frequency generation, true single phase clock (TSPC) dividers are used while for the harmonic rejection (HR) mixers to generate the required LO frequencies (6 phases, 0-45-90-180-225 and 270 degrees) for the AS_1 signal generation, current-mode-logic (CML) frequency dividers are used with a ratio of 4. To generate

the AS_1 signal (240 MHz) for on-chip adaptive sampling for real-time phase calibration, RF comb is upconverted with 400 MHz, while the LO comb is up-converted with 160 MHz, to eliminate the harmonics' effects, harmonic rejection mixers (based on a passive mixer architecture) are utilized. Due to the narrow BW of the IF comb with low frequency content at the BB, one of the advantages of the DCS systems is to enable a single UWB pulse processing instead of sub-carriers proposed in [7]. Therefore, an on-chip UWB pulse generation is achieved with a Gaussian monocyle pulse generator, since Gaussian derivatives have a dc-free broadband spectrum itself as shown in Fig. 4.8 (a), it has a 6 GHz 10-dB BW (1 GHz-7 GHz) centered at 4.5 GHz. To generate the 3-10 GHz signal, this signal is upconverted using the 3.2 GHz input signal, and hence new Gaussian monocycle pulse is moved to 4.2-to-10.2 GHz with 10-dB BW. With an analog adder two Gaussian first derivative pulses are combined and the generated on-chip pulse spectrum and phase results are shown in Fig. 4.8 (b).

4.5 Fabrication and Experimental Results

Fig. 4.9 (a) shows the chip micrograph of the proposed DCS system, packaged chip, and the plastic tube for MUT disposition, and Fig. 4.9 (b) shows the fabricated printed circuit board to test the chip respectively. The chip fabricated in 65nm CMOS technology occupies an area of 1.98 mm^2 and consumes average $\sim$72 mW from a 1 V supply. For the chip assembly, QFN 28 pin open cavity plastic package (OCPP) 4 x 4 mm^2 is used. To protect the bondwires and to eliminate any material leakage to the LO_{Comb}, an open cavity laser-cut plastic package is used, which is partially encapsulated with epoxy so that only the sensor of the RF_{Comb} is open to the air, while the passivation opening is not utilized for the LO_{Comb} sensor to prevent the possible chemicals leaks and degradation of the system accuracy. A cylindrical plastic tube covering the opened sensing unit area is glued on top of the packaged chip to hold the liquid under test (Fig. 6(c)), while the tube is capped after MUT insertion to prevent the liquid evaporation. To verify the chip performance of the proposed DCS system, different chemical liquids (ethanol, methanol, and water) with volumes $\sim$0.01 nL were injected into the tube using a Finnpipette single-channel micropipette.

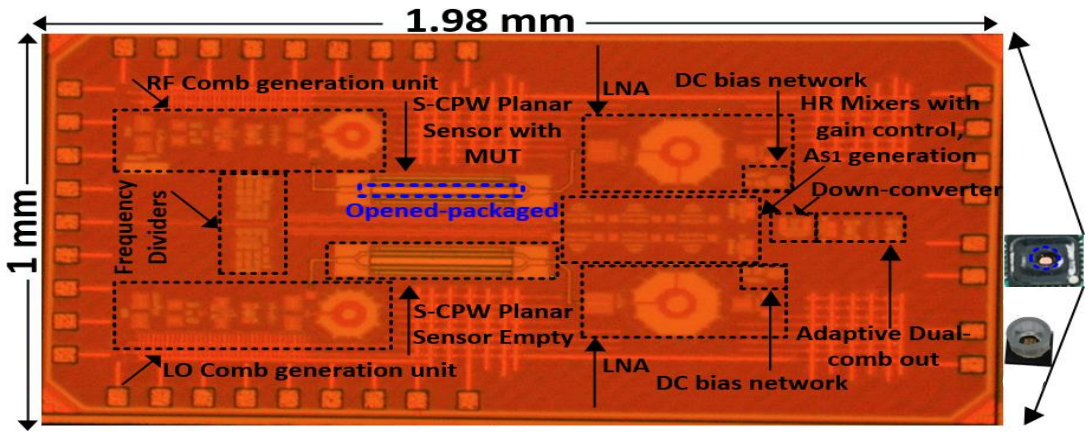

(a)

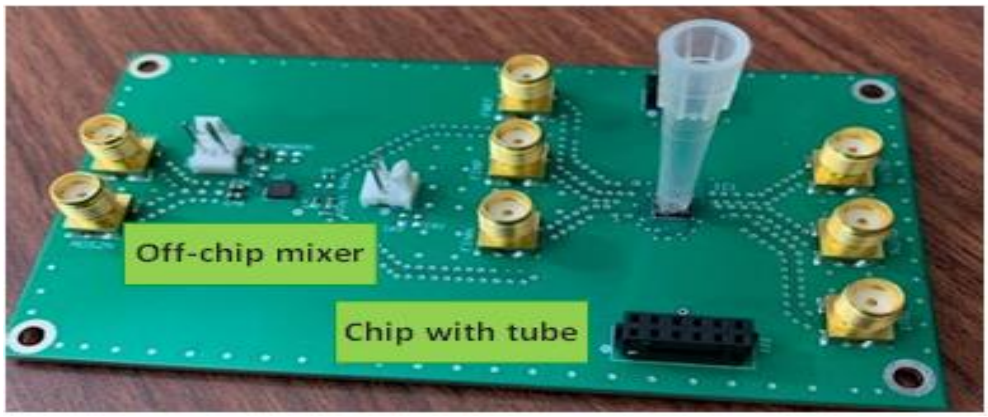

(b)

Figure 4.9: (a) Micrograph of the fabricated DCS sytem, (b) plastic tube glued on top of chip, and (c) partially packaged chip (only the sensor of the test path is open). (Reprinted from [90,99])

Fig. 4.10 shows a window of IF combs in TD captured with a low frequency oscilloscope. The time difference is 0.1 ms between the comb teeth which verifies the Δf_r=10 KHz frequency. The effects of test MUTs on the signal magnitude and phase in the microwave range are mapped to the IF baseband. The effects of three test MUTs on the output signal magnitude and phase in the desired microwave range are mapped to the baseband by applying FFT to a window of IF baseband comb-captured signal in the TD with a low-frequency oscilloscope, as shown in Figure 4. 11 (a) and (b), respectively. Fig. 4.12 (a) and (b) depict the averaged some selected BB output samples in FD comparing with the sensor simulations (see Fig. 4.5 (a) and (b)) to verify the proposed system

for material characterization. The proposed CMOS broadband microwave DCS system achieves an RMS permittivity error of less than 0.24%, and 0.37% for ϵ_r' and ϵ_r'' over the entire desired bandwidth compared to sensor outputs.

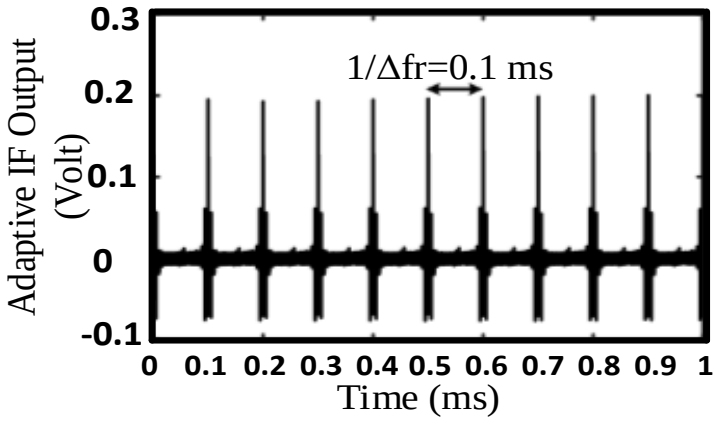

Figure 4.10: Measurement results of the proposed DCS system in TD. (Reprinted from [99])

Table 4.1 summarizes the performance of the fabricated system and compares it with the prior published works, which shows that the proposed system has a simplified miniaturized architecture with a small chip area while utilizing an on-chip single carrier UWB pulse generation and on-chip system calibration. The FD systems utilizing single-tone input require complex, power-hungry sweeping frequency synthesizers, while the self-sustained systems have narrow BW and provide the MUT complex permittivity spectrum choosing specific sensing frequency points; in other words, they might either need a long measurement and calibration time or have low accuracy due to low resolution. On the other hand, the TD homodyne RF-TX system relaxes the sampling rate of the output that requires an ADC with at least a 2-Gs/s sampling rate. However, the TD dual-frequency comb-based system requires only an inexpensive, low-frequency ADC for measurements by reducing the cost of the system significantly. Note that the work can be converted to a self-sustained system if the required input signal (3.2 GHz) is provided by an on-chip frequency synthesizer.

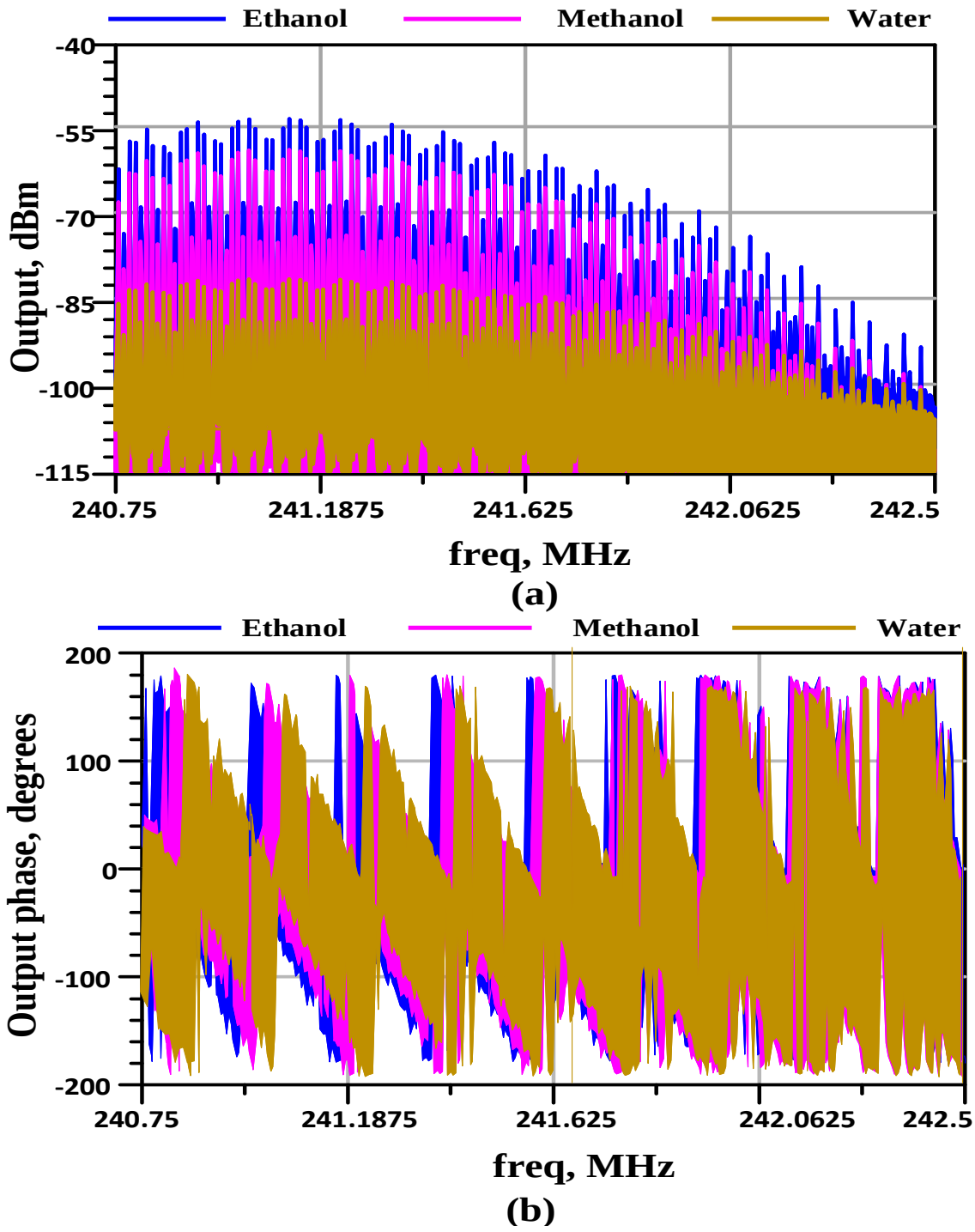

Figure 4.11: (a) Magnitude and (b) phase measurement results of the proposed DCS system in FD for ethanol, methanol, and water, respectively. (Reprinted from [99])

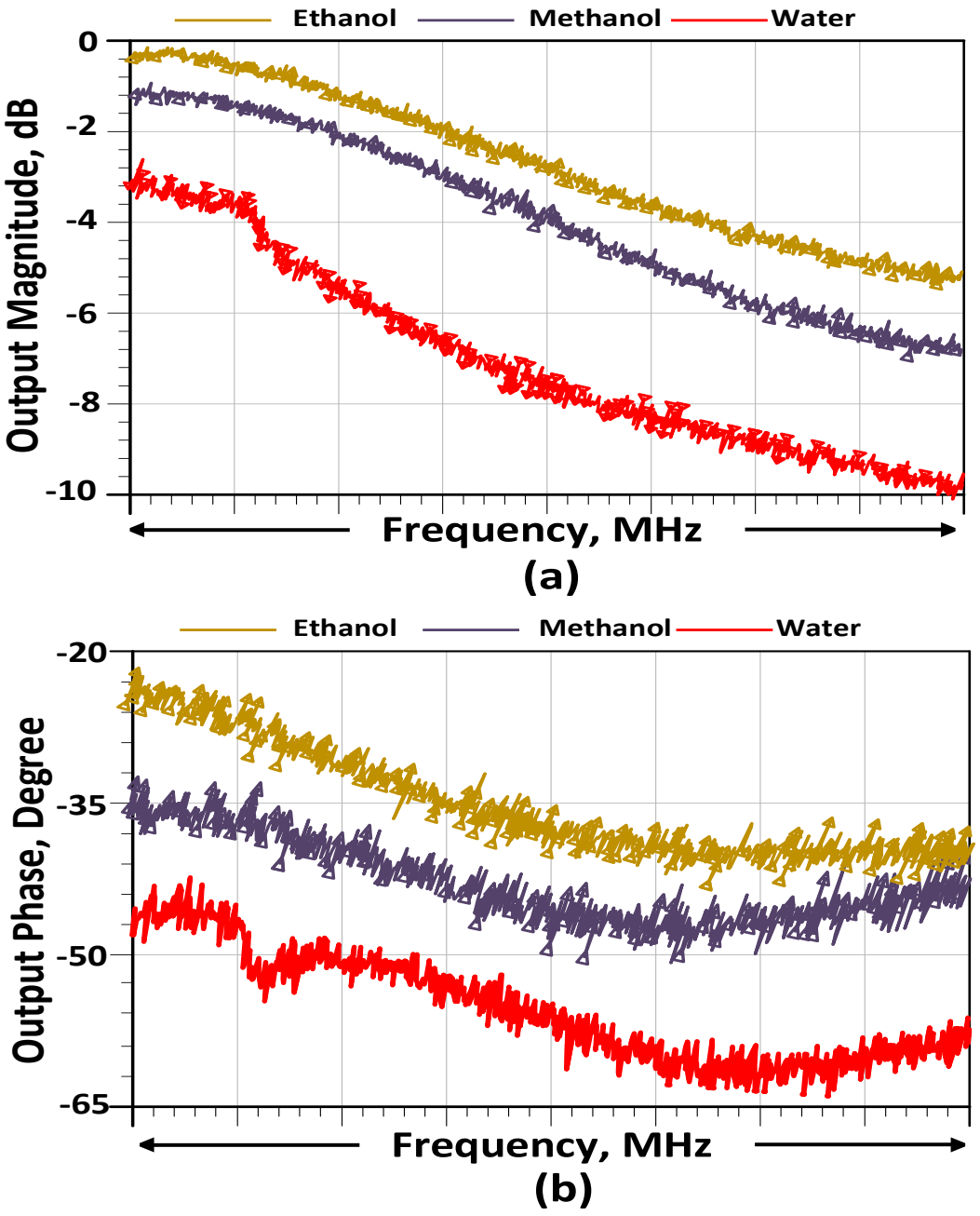

Figure 4.12: Output (a) Magnitude and (b) phase difference from the reference material measurement, FFT results of the proposed DCS system in FD for ethanol, methanol, and water, respectively.

Table 4.1: CMOS Dielectric Microwave Detector Comparison with State of the Art

Reference	CMOS	Architec./Meas. Tech.	Excitation Pulse	Freq. Range (GHz)	Sensing Unit	Area [mm^2]	Detection Capability
[7]	65 nm	Homodyne RF-TX/TD	On-chip 1 GHz BW	3-10	Off-chip, Vivaldi Antenna	1.68	ϵ_r' and ϵ_r''
[32]	0.18μm	Homodyne RF-RX/FD	Off-chip Single tone	0.62-10	On-chip, 2D Capacitor	9	ϵ_r' and ϵ_r''
[33]	65 nm	Heterodyne RF-RX/FD	Off-chip Single tone	1-50	On-chip, T Line	1.2	ϵ_r' and ϵ_r''
[34]	90 nm	LC-Osc & PLL/FD	Self-sustained	7-9	On-chip, 2D Capacitor	6.25	ϵ_r'
[39]	0.18μm	LC-Osc/FD	Self-sustained	0.98-6	On-chip, 2D Capacitor	6.24	ϵ_r' and ϵ_r''
[40]	65 nm	Homodyne RF-RX/FD	Self-sustained	5-8	On-chip, T Line	1.68	ϵ_r' and ϵ_r''
This Work	65 nm	Dual-frequency-comb/TD	On-chip, 8 GHZ BW	3-10	On-chip (GSSG) S-CPW	1.98	ϵ_r' and ϵ_r''

5. CONCLUSION

This dissertation focuses on novel miniaturized on-chip RF/microwave broadband spectroscopy systems for chemical/biomaterial identification through their complex permittivity property.

An ultra-wideband (UWB), 3-10 GHz, miniaturized contactless microwave broadband dielectric spectroscopy system prototype in the time domain for complex permittivity characterization of the liquid chemicals is proposed and implemented using 65nm CMOS technology and validated by determining unknown chemical materials and mixtures. A CMOS RF homodyne transceiver with a dc-free down-conversion architecture is employed to detect the magnitude and the phase variation of a wideband RF pulse after passing through a contactless sensor carrying the MUT at the receiver baseband. Organic chemicals including xylene, butanol, ethanol, methanol, and DMSO are characterized, and their detected complex permittivities are used as reference material under test (MUT). A calibration method using nonlinear reciprocal-quadratic curve fittings which relates the phase and magnitude differences ($\Delta\phi$, ΔMag) of the output signal with respect to a reference material (air) to the ϵ_r' and ϵ_r" of the MUTs is presented. The proposed microwave broadband dielectric spectroscopy system is able to detect the complex permittivity of the organic chemicals with an $RMSE_{min}$ = 0.0113% and $RMSE_{max}$ = 0.1478% for ϵ_r' and as $RMSE_{min}$ = 0.2557% and $RMSE_{max}$ = 0.4238% for ϵ_r'', while it is as worst-case 0.1729% in ϵ_r' and 0.3935% in ϵ_r'' for mixtures within the desired frequency range. The prototyped system occupies an active area of 1.24 mm^2 while consuming 64$\sim$69 mW from a 1 V supply.

A time-domain integrated ultra-wideband microwave coherent dual-comb spectroscopy (DCS) system, with two on-chip frequency combs with tunable and slightly different repetition frequency rates, is presented for liquid chemicals detection. One of the frequency combs (RF_{Comb}) interrogates a coplanar waveguide, ground-signal-signal-ground, (CPW-GSSG) planar transmission line sensor loaded with the MUT. In contrast, the other identical empty sensor is excited by the second comb (LO_{Comb}). Two frequency combs are then heterodyned using a UWB mixer to generate the dual-comb output representing the MUT properties from microwave frequencies mapped to low

frequencies, eliminating the need to use high-frequency analog-to-digital converters (ADCs). To achieve detection of both real and imaginary parts of the complex permittivity of liquid samples, an adaptive sampling method and phase-locking of all sources are utilized. The 3-10 GHz microwave DCS system, fabricated in 65 nm CMOS, occupies 1.98 mm^2 an area and consumes $\sim$72 mW from a 1 V supply. To verify the chemical detection, MUTs, including ethanol, methanol, and water, results at the output of the DCS system are presented and compared to sensor simulation results. The proposed CMOS broadband microwave DCS system achieves an RMS permittivity error of less than 0.24$\%$, and 0.37$\%$ for ϵ_r' and ϵ_r'' over the entire desired bandwidth.

The proposed approaches provide miniaturized, fast, simplified, power and area efficient on-chip time-domain spectroscopy systems for unknown chemical sensing with high accuracy utilizing their complex permittivity detection. To the best of the author's knowledge, prototyped both microwave system-on-chips (SoCs) are the first homodyne transceiver-based contactless and the first CMOS dual-comb spectroscopy systems.

In future work, a prototype for microwave dual-comb dielectric spectroscopy is under development: a fully integrated CMOS chemical sensor for complex permittivity detection for the broader frequency range of 1 - 30 GHz for medical applications will incorporate a frequency synthesizer to enable a self-sustained operation, an on-chip auto-calibration circuitry, and a digital signal processing module for auto-calibration based on artificial intelligence neural networks to realize ultra-miniaturized portable spectroscopy systems.

REFERENCES

[1] W. H. Woodward, "Broadband dielectric spectroscopy-a practical guide," in *Broadband Dielectric Spectroscopy: A Modern Analytical Technique*, pp. 3–59, ACS Publications, 2021.

[2] F. Kremer and A. Schönhals, *Broadband dielectric spectroscopy*. Springer Science & Business Media, 2002.

[3] A. P. Gregory and R. Clarke, *Tables of the complex permittivity of dielectric reference liquids at frequencies up to 5 GHz*. National Physical Laboratory Teddington, 2001.

[4] F. Buckley, "Tables of dielectric dispersion data for pure liquids and dilute solutions," *National Bureau of Standards Circular*, vol. 589, pp. 7–8, 1958.

[5] A. H. Shivola, "Self-consistency aspects of dielectric mixing theories," *IEEE Transactions on Geoscience and Remote Sensing*, vol. 27, no. 4, pp. 403–415, 1989.

[6] A. Sihvola, "Mixing rules with complex dielectric coefficients," *Subsurface Sensing Technologies and Applications*, vol. 1, no. 4, pp. 393–415, 2000.

[7] E. Kaya, A. P. Saghati, and K. Entesari, "A 3-10-ghz cmos time-domain complex dielectric spectroscopy system using a contactless sensor," *IEEE Transactions on Microwave Theory and Techniques*, pp. 1–16, 2019.

[8] H. Cook, "Dielectric behaviour of human blood at microwave frequencies," *Nature*, vol. 168, no. 4267, p. 247, 1951.

[9] A. Lonappan, V. Thomas, G. Bindu, C. Rajasekaran, and K. Mathew, "Nondestructive measurement of human blood at microwave frequencies," *Journal of Electromagnetic Waves and Applications*, vol. 21, no. 8, pp. 1131–1139, 2007.

[10] A. Lonappan, V. T. Gopinathan Nair Bindu, and K. Mathew, "Analysis of human semen using microwaves," *Progress In Electromagnetics Research*, vol. 57, pp. 277–284, 2006.

[11] A. Lonappan, V. Thomas, G. Bindu, C. Rajasekaran, and K. Mathew, "Analysis of human cerebro spinal fluid at the ism band of frequencies," *Journal of Electromagnetic Waves and Applications*, vol. 20, no. 6, pp. 773–779, 2006.

[12] P. Banerjee, G. Ghosh, and S. K. Biswas, "A system to measure dielectric constant and loss of liquids at microwave frequencies," in *2009 Applied Electromagnetics Conference (AEMC)*, pp. 1–2, IEEE, 2009.

[13] C. Wakai, A. Oleinikova, M. Ott, and H. Weingärtner, "How polar are ionic liquids? determination of the static dielectric constant of an imidazolium-based ionic liquid by microwave dielectric spectroscopy," *The Journal of Physical Chemistry B*, vol. 109, no. 36, pp. 17028–17030, 2005.

[14] Y. Feldman, A. Andrianov, E. Polygalov, I. Ermolina, G. Romanychev, Y. Zuev, and B. Milgotin, "Time domain dielectric spectroscopy: An advanced measuring system," *Review of Scientific Instruments*, vol. 67, no. 9, pp. 3208–3216, 1996.

[15] R. H. Cole, "Time-domain spectroscopy of dielectric materials," *IEEE Transactions on Instrumentation and Measurement*, no. 4, pp. 371–375, 1976.

[16] Y. Cui and P. Wang, "The design and operation of ultra-sensitive and tunable radio-frequency interferometers," *IEEE Transactions on Microwave Theory and Techniques*, vol. 62, no. 12, pp. 3172–3182, 2014.

[17] R. E. Ghiri, A. P. Saghati, E. Kaya, and K. Entesari, "A 3–10 ghz contact-less complex dielectric spectroscopy system," in *2017 IEEE MTT-S International Microwave Symposium (IMS) Digest*, pp. 621–623, IEEE, 2017.

[18] R. E. Ghiri, A. P. Saghati, E. Kaya, and K. Entesari, "A miniaturized contactless uwb microwave system for time-domain dielectric spectroscopy," *IEEE Transactions on Microwave Theory and Techniques*, vol. 65, no. 12, pp. 5334–5344, 2017.

[19] R. E. Ghiri, E. Kaya, and K. Entesari, "Time-domain dielectric spectroscopy using a miniaturized contact-based uwb system," *IEEE Transactions on Microwave Theory and Techniques*, vol. 66, no. 12, pp. 5863–5872, 2018.

[20] D. K. Ghodgaonkar, V. V. Varadan, and V. K. Varadan, "A free-space method for measurement of dielectric constants and loss tangents at microwave frequencies," *IEEE Transactions on Instrumentation and measurement*, vol. 38, no. 3, pp. 789–793, 1989.

[21] Z. Akhter and M. J. Akhtar, "Free-space time domain position insensitive technique for simultaneous measurement of complex permittivity and thickness of lossy dielectric samples," *IEEE Transactions on Instrumentation and Measurement*, vol. 65, no. 10, pp. 2394–2405, 2016.

[22] I. Vakili, L. Ohlsson, L.-E. Wernersson, and M. Gustafsson, "Time-domain system for millimeter-wave material characterization," *IEEE Transactions on Microwave Theory and Techniques*, vol. 63, no. 9, pp. 2915–2922, 2015.

[23] C. A. Balanis, *Antenna theory: analysis and design*. John wiley & sons, 2015.

[24] J. Wu, Z. Zhao, Z. Nie, and Q.-H. Liu, "A printed uwb vivaldi antenna using stepped connection structure between slotline and tapered patches," *IEEE Antennas and Wireless Propagation Letters*, vol. 13, pp. 698–701, 2014.

[25] H. Fröhlich, *Theory of dielectrics: dielectric constant and dielectric loss*. Clarendon Press, 1949.

[26] I. Bahl and S. S. Stuchly, "Analysis of a microstrip covered with a lossy dielectric," *IEEE Transactions on Microwave Theory and Techniques*, vol. 28, no. 2, pp. 104–109, 1980.

[27] G. Gonzalez, *Microwave transistor amplifiers analysis and design*. Prentice-Hall, Inc., 1996.

[28] K. Entesari, A. A. Helmy, and M. Moslehi-Bajestan, "Integrated systems for biomedical applications: Silicon-based rf\/microwave dielectric spectroscopy and sensing," *IEEE Microwave Magazine*, vol. 18, no. 5, pp. 57–72, 2017.

[29] Y.-Z. Wei and S. Sridhar, "Technique for measuring the frequency-dependent complex dielectric constants of liquids up to 20 ghz," *Review of Scientific Instruments*, vol. 60, no. 9, pp. 3041–3046, 1989.

[30] A. A. Helmy and K. Entesari, "A 1–8-ghz miniaturized spectroscopy system for permittivity detection and mixture characterization of organic chemicals," *IEEE Transactions on Microwave Theory and Techniques*, vol. 60, no. 12, pp. 4157–4170, 2012.

[31] R. E. Ghiri, A. P. Saghati, E. Kaya, and K. Entesari, "A 3–10 ghz contact-less complex dielectric spectroscopy system," in *2017 IEEE MTT-S International Microwave Symposium (IMS) Digest*, pp. 621–623, IEEE, 2017.

[32] M. M. Bajestan, A. A. Helmy, H. Hedayati, and K. Entesari, "A 0.62–10 ghz complex dielectric spectroscopy system in cmos," *IEEE Transactions on Microwave Theory and Techniques*, vol. 62, no. 12, pp. 3522–3537, 2014.

[33] J.-C. Chien, M. Anwar, E.-C. Yeh, L. P. Lee, and A. M. Niknejad, "A 1–50 ghz dielectric spectroscopy biosensor with integrated receiver front-end in 65nm cmos," in *2013 IEEE MTT-S International Microwave Symposium (IMS) Digest*, pp. 1–4, IEEE, 2013.

[34] A. A. Helmy, H.-J. Jeon, Y.-C. Lo, A. J. Larsson, R. Kulkarni, J. Kim, J. Silva-Martinez, and K. Entesari, "A self-sustained cmos microwave chemical sensor using a frequency synthesizer," *IEEE Journal of Solid-State Circuits*, vol. 47, no. 10, pp. 2467–2483, 2012.

[35] M. Bakhshiani, M. A. Suster, and P. Mohseni, "A 9 mhz–2.4 ghz fully integrated transceiver ic for a microfluidic-cmos platform dedicated to miniaturized dielectric spectroscopy," *IEEE Transactions on Biomedical Circuits and Systems*, vol. 9, no. 6, pp. 849–861, 2015.

[36] O. Elhadidy, S. Shakib, K. Krenek, S. Palermo, and K. Entesari, "A 0.18-μm cmos fully integrated 0.7–6 ghz pll-based complex dielectric spectroscopy system," in *Proceedings of the IEEE 2014 Custom Integrated Circuits Conference*, pp. 1–4, IEEE, 2014.

[37] H. Wang, S. Kosai, C. Sideris, and A. Hajimiri, "An ultrasensitive cmos magnetic biosensor array with correlated double counting noise suppression," in *2010 IEEE MTT-S International Microwave Symposium (IMS) Digest*, pp. 616–619, IEEE, 2010.

[38] O. Elhadidy, S. Shakib, K. Krenek, S. Palermo, and K. Entesari, "A wide-band fully-integrated cmos ring-oscillator pll-based complex dielectric spectroscopy system," *IEEE Transactions on Circuits and Systems I: Regular Papers*, vol. 62, no. 8, pp. 1940–1949, 2015.

[39] M. Elkholy and K. Entesari, "A wideband low-power lc-dco-based complex dielectric spectroscopy system in 0.18-μm cmos," *IEEE Transactions on Microwave Theory and Techniques*, vol. 65, no. 11, pp. 4461–4474, 2017.

[40] S. Ma, N. Li, and J. Ren, "A 5-to-8-ghz wideband miniaturized dielectric spectroscopy chip with i/q mismatch calibration in 65-nm cmos," *IEEE Transactions on Very Large Scale Integration (VLSI) Systems*, vol. 26, no. 8, pp. 1554–1564, 2018.

[41] R. E. Ghiri, E. Kaya, and K. Entesari, "A miniaturized 3–10 ghz time-domain contact-based dielectric spectroscopy system," in *2018 IEEE MTT-S International Microwave Symposium (IMS) Digest*, pp. 108–110, IEEE, 2018.

[42] E. Kaya, A. P. Saghati, and K. Entesari, "A cmos time domain microwave broadband dielectric spectroscopy system with a contact-less sensor for liquid chemical detection," in *2019 IEEE MTT-S International Microwave Symposium Digest, accepted for publication*, IEEE, 2019.

[43] E. Janssen, K. Doris, A. Zanikopoulos, A. Murroni, G. Van der Weide, Y. Lin, L. Alvado, F. Darthenay, and Y. Fregeais, "An 11b 3.6 gs/s time-interleaved sar adc in 65nm cmos," in *2013 IEEE International Solid-State Circuits Conference Digest of Technical Papers (ISSCC)*, pp. 464–465, IEEE, 2013.

[44] H. Wei, P. Zhang, B. D. Sahoo, and B. Razavi, "An 8 bit 4 gs/s 120 mw cmos adc," *IEEE Journal of Solid-State Circuits*, vol. 49, no. 8, pp. 1751–1761, 2014.

[45] M. Bassi, M. Caruso, A. Bevilacqua, and A. Neviani, "A 1.75–15 ghz stepped frequency receiver for breast cancer imaging in 65 nm cmos," in *2012 Proceedings of The European Solid-State Circuits Conference (ESSCIRC)*, pp. 353–356, IEEE, 2012.

[46] Y.-K. Hsieh and L.-H. Lu, "A 19 ghz cmos signal generator for 77 ghz fmcw radars," *IEEE Microwave and Wireless Components Letters*, vol. 24, no. 5, pp. 339–341, 2014.

[47] H. Hedayati and K. Entesari, "A 90-nm cmos uwb impulse radio transmitter with 30-db in-band notch at ieee 802.11 a system," *IEEE Transactions on Microwave Theory and Techniques*, vol. 61, no. 12, pp. 4220–4232, 2013.

[48] M. Min, U. Pliquett, T. Nacke, A. Barthel, P. Annus, and R. Land, "Signals in bioimpedance measurement: different waveforms for different tasks," in *13th International Conference on Electrical Bioimpedance and the 8th Conference on Electrical Impedance Tomography*, pp. 181–184, Springer, 2007.

[49] C.-F. Liao and S.-I. Liu, "A broadband noise-canceling cmos lna for 3.1–10.6-ghz uwb receivers," *IEEE Journal of Solid-State Circuits*, vol. 42, no. 2, pp. 329–339, 2007.

[50] S. S. Ho and C. E. Saavedra, "A cmos broadband low-noise mixer with noise cancellation," *IEEE Transactions on Microwave Theory and Techniques*, vol. 58, no. 5, pp. 1126–1132, 2010.

[51] R. Sapawi, R. K. Pokharel, S. A. Murad, A. Anand, N. Koirala, H. Kanaya, and K. Yoshida, "Low group delay 3.1–10.6 ghz cmos power amplifier for uwb applications," *IEEE Microwave and Wireless Components Letters*, vol. 22, no. 1, pp. 41–43, 2012.

[52] N. Poobuapheun, W.-H. Chen, Z. Boos, and A. M. Niknejad, "A 1.5-v 0.7–2.5-ghz cmos quadrature demodulator for multiband direct-conversion receivers," *IEEE Journal of Solid-State Circuits*, vol. 42, no. 8, pp. 1669–1677, 2007.

[53] M. Borremans, "Up converter mixer linearization improvement," June 2 2009. US Patent 7,542,739.

[54] W.-H. Chen and B. Jung, "High-speed low-power true single-phase clock dual-modulus prescalers," *IEEE Transactions on Circuits and Systems II: Express Briefs*, vol. 58, no. 3, pp. 144–148, 2011.

[55] Z. Deng and A. M. Niknejad, "The speed–power trade-off in the design of cmos true-single-phase-clock dividers," *IEEE Journal of Solid-State Circuits*, vol. 45, no. 11, pp. 2457–2465, 2010.

[56] J. Kaukovuori, K. Stadius, J. Ryynanen, and K. A. Halonen, "Analysis and design of passive polyphase filters," *IEEE Transactions on Circuits and Systems I: Regular Papers*, vol. 55, no. 10, pp. 3023–3037, 2008.

[57] T.-Y. Lu and W.-Z. Chen, "A 3–10 ghz, 14 bands cmos frequency synthesizer with spurs reduction for mb-ofdm uwb system," *IEEE Transactions on Very Large Scale Integration (VLSI) Systems*, vol. 20, no. 5, pp. 948–958, 2012.

[58] Y.-T. Lo and J.-F. Kiang, "A single-sideband mixer with band selection through an output switching quad," in *The 40th European Microwave Conference*, pp. 1130–1133, IEEE, 2010.

[59] N.-S. Kim and J. M. Rabaey, "A high data-rate energy-efficient triple-channel uwb-based cognitive radio," *IEEE Journal of Solid-State Circuits*, vol. 51, no. 4, pp. 809–820, 2016.

[60] K.-H. Chen and S.-I. Liu, "Inductorless wideband cmos low-noise amplifiers using noise-canceling technique," *IEEE Transactions on Circuits and Systems I: Regular Papers*, vol. 59, no. 2, pp. 305–314, 2012.

[61] B. Shi and M. Y. W. Chia, "A 3.1-10.6 ghz rf front-end for multiband uwb wireless receivers," in *2005 IEEE Radio Frequency Integrated Circuits Symposium (RFIC) Digest Papers*, pp. 343–346, IEEE, 2005.

[62] R.-F. Ye, T.-S. Horng, and J.-M. Wu, "Low power fsk receiver using an oscillator-based injection-locked frequency divider," *IEEE Microwave and Wireless Components Letters*, vol. 24, no. 2, pp. 114–116, 2014.

[63] E. A. Klumperink, S. M. Louwsma, G. J. Wienk, and B. Nauta, "A cmos switched transconductor mixer," *IEEE Journal of Solid-State Circuits*, vol. 39, no. 8, pp. 1231–1240, 2004.

[64] J.-B. Seo, J.-H. Kim, H. Sun, and T.-Y. Yun, "A low-power and high-gain mixer for uwb systems," *IEEE Microwave and Wireless Components Letters*, vol. 18, no. 12, pp. 803–805, 2008.

[65] Z. Zhang, Z. Chen, L. Tsui, and J. Lau, "A 930 mhz cmos dc-offset-free direct-conversion 4-fsk receiver," in *IEEE International Solid-State Circuits Conference (ISSCC) Digest of Technical Papers*, pp. 290–291, IEEE, 2001.

[66] H.-K. Chiou, K.-C. Lin, W.-H. Chen, and Y.-Z. Juang, "A 1-v 5-ghz self-bias folded-switch mixer in 90-nm cmos for wlan receiver," *IEEE Transactions on Circuits and Systems I: Regular Papers*, vol. 59, no. 6, pp. 1215–1227, 2012.

[67] W.-C. Wang, C.-P. Liao, Y.-K. Lo, Z.-D. Huang, F. R. Shahroury, and C.-Y. Wu, "The design of integrated 3-ghz to 11-ghz cmos transmitter for full-band ultra-wideband (uwb) applications," in *2008 IEEE International Symposium on Circuits and Systems (ISCAS)*, pp. 2709–2712, IEEE, 2008.

[68] "Curve fitting with linear and nonlinear regression." `https://blog.minitab.com/blog/adventures-in-statistics-2/curve-fitting-with-linear-and-nonlinear-regression`. (Accessed on 04/05/2019).

[69] D. Wheeler, G. Shaw, and S. Barr, *Statistical techniques in geographical analysis*. Routledge, 2013.

[70] S. T. U. Guide, "suggest@ mathworks. com product enhancement suggestions," 1999.

[71] M. Brandolini, Y. Shin, K. Raviprakash, T. Wang, R. Wu, H. M. Geddada, Y.-J. Ko, Y. Ding, C.-S. Huang, W.-T. Shin, *et al.*, "26.6 a 5gs/s 150mw 10b sha-less pipelined/sar hybrid adc in 28nm cmos," in *2015 IEEE International Solid-State Circuits Conference-(ISSCC) Digest of Technical Papers*, pp. 1–3, IEEE, 2015.

[72] M. Mishali and Y. C. Eldar, "Blind multiband signal reconstruction: Compressed sensing for analog signals," *IEEE Transactions on Signal Processing*, vol. 57, no. 3, pp. 993–1009, 2009.

[73] M. Mishali and Y. C. Eldar, "From theory to practice: Sub-nyquist sampling of sparse wideband analog signals," *IEEE Journal of Selected Topics in Signal Processing*, vol. 4, no. 2, pp. 375–391, 2010.

[74] G. T. Ruck, "Ultrawideband radar receiver," in *Ultrawideband Radar*, vol. 1631, pp. 174–180, International Society for Optics and Photonics, 1992.

[75] J.-W. Nam, M. Hassanpourghadi, A. Zhang, and M. S.-W. Chen, "A 12-bit 1.6 gs/s interleaved sar adc with dual reference shifting and interpolation achieving 17.8 fj/conv-step in 65nm cmos," in *2016 IEEE Symposium on VLSI Circuits (VLSI-Circuits)*, pp. 1–2, IEEE, 2016.

[76] Y.-C. Lo, N. Rashidi, Y.-H. Hwang, and J. Silva-Martinez, "A 0.6 ps jitter 2–16 ghz 130nm cmos frequency synthesizer for broadband applications," in *2015 IEEE International Symposium on Circuits and Systems (ISCAS)*, pp. 3048–3051, IEEE, 2015.

[77] M. Caruso, M. Bassi, A. Bevilacqua, and A. Neviani, "A 2–16 ghz 65 nm cmos stepped-frequency radar transmitter with harmonic rejection for high-resolution medical imaging applications," *IEEE Transactions on Circuits and Systems I: Regular Papers*, vol. 62, no. 2, pp. 413–422, 2014.

[78] Y. Feldman, I. Ermolina, and Y. Hayashi, "Time domain dielectric spectroscopy study of biological systems," *IEEE Transactions on Dielectrics and Electrical Insulation*, vol. 10, no. 5, pp. 728–753, 2003.

[79] W. S. Zaengl, "Dielectric spectroscopy in time and frequency domain for hv power equipment. i. theoretical considerations," *IEEE Electrical Insulation Magazine*, vol. 19, no. 5, pp. 5–19, 2003.

[80] J. E. Pedersen and S. R. Keiding, "Thz time-domain spectroscopy of nonpolar liquids," *IEEE Journal of Quantum Electronics*, vol. 28, no. 10, pp. 2518–2522, 1992.

[81] R. Nozaki and T. K. Bose, "Broadband complex permittivity measurements by time-domain spectroscopy," *IEEE Transactions on Instrumentation and Measurement*, vol. 39, no. 6, pp. 945–951, 1990.

[82] I. Ermolina, Y. Polevaya, Y. Feldman, B. . Ginzburg, and M. Schlesinger, "Study of normal and malignant white blood cells by time domain dielectric spectroscopy," *IEEE Transactions on Dielectrics and Electrical Insulation*, vol. 8, no. 2, pp. 253–261, 2001.

[83] E. Kaya, A. P. Saghati, and K. Entesari, "A cmos time domain microwave broadband dielectric spectroscopy system with a contact-less sensor for liquid chemical detection," in *IEEE MTT-S International Microwave Symposium (IMS) Digest*, pp. 800–803, 2019.

[84] N. Picqué and T. W. Hänsch, "Frequency comb spectroscopy," *Nature Photonics*, vol. 13, no. 3, pp. 146–157, 2019.

[85] I. Coddington, N. Newbury, and W. Swann, "Dual-comb spectroscopy," *Optica*, vol. 3, no. 4, pp. 414–426, 2016.

[86] A. Dutt, C. Joshi, X. Ji, J. Cardenas, Y. Okawachi, K. Luke, A. L. Gaeta, and M. Lipson, "On-chip dual-comb source for spectroscopy," *Science Advances*, vol. 4, no. 3, p. e1701858, 2018.

[87] M. Yu, Y. Okawachi, A. G. Griffith, N. Picqué, M. Lipson, and A. L. Gaeta, "Silicon-chip-based mid-infrared dual-comb spectroscopy," *Nature Communications*, vol. 9, no. 1, pp. 1–6, 2018.

[88] J. Olson, Y. Ou, A. Azarm, and K. Kieu, "Bi-directional mode-locked thulium fiber laser as a single-cavity dual-comb source," *IEEE Photonics Technology Letters*, vol. 30, no. 20, pp. 1772–1775, 2018.

[89] E. Kaya and K. Entesari, "A broadband cmos pulse generator for uwb systems," in *2020 IEEE Radio and Wireless Symposium (RWS)*, pp. 9–11, IEEE, 2020.

[90] E. Kaya and K. Entesari, "Silicon integrated broadband dual frequency comb-based microwave detector for material characterization," in *2022 IEEE Radio and Wireless Symposium (RWS)*, pp. 79–82, IEEE, 2022.

[91] R. E. Ghiri and K. Entesari, "A miniaturized uwb microwave dual-comb dielectric spectroscopy system," *IEEE Transactions on Microwave Theory and Techniques*, vol. 67, no. 12, pp. 5218–5227, 2019.

[92] Z. Chen, M. Yan, T. W. Hänsch, and N. Picqué, "A phase-stable dual-comb interferometer," *Nature Communications*, vol. 9, no. 1, pp. 1–7, 2018.

[93] T. Ideguchi, A. Poisson, G. Guelachvili, T. W. Hänsch, and N. Picqué, "Adaptive dual-comb spectroscopy in the green region," *Optics Letters*, vol. 37, no. 23, pp. 4847–4849, 2012.

[94] G. Ycas, F. R. Giorgetta, E. Baumann, I. Coddington, D. Herman, S. A. Diddams, and N. R. Newbury, "High-coherence mid-infrared dual-comb spectroscopy spanning 2.6 to 5.2 μm," *Nature Photonics*, vol. 12, no. 4, pp. 202–208, 2018.

[95] A. Schliesser, N. Picqué, and T. W. Hänsch, "Mid-infrared frequency combs," *Nature Photonics*, vol. 6, no. 7, p. 440, 2012.

[96] T. Ideguchi, A. Poisson, G. Guelachvili, N. Picqué, and T. W. Hänsch, "Adaptive real-time dual-comb spectroscopy," *Nature Communications*, vol. 5, p. 3375, 2014.

[97] Y.-D. Hsieh, Y. Iyonaga, Y. Sakaguchi, S. Yokoyama, H. Inaba, K. Minoshima, F. Hindle, T. Araki, and T. Yasui, "Spectrally interleaved, comb-mode-resolved spectroscopy using swept dual terahertz combs," *Scientific Reports*, vol. 4, p. 3816, 2014.

[98] I. Coddington, W. Swann, and N. Newbury, "Coherent dual-comb spectroscopy at high signal-to-noise ratio," *Physical Review A*, vol. 82, no. 4, p. 043817, 2010.

[99] E. Kaya and K. Saghatiand Entesari, "A cmos microwave broadband adaptive dual-comb dielectric spectroscopy system for liquid chemical detection," in *IEEE MTT-S International Microwave Symposium (IMS) Digest*, August 2020.

[100] G. E. Ponchak, L. P. Katehi, and E. M. Tentzeris, "Finite ground coplanar (fgc) waveguide: it's characteristics and advantages for use in rf and wireless communication circuits," in *International Wireless Communications Conference (WCC"98)*, 1998.

[101] M. Sameer and P. Agarwal, "Coplanar waveguide microwave sensor for label-free real-time glucose detection," *Radioengineering*, vol. 28, no. 2, p. 491, 2019.

[102] M. Frank, A. Talai, R. Weigel, and A. Koelpin, "In-line material characterization sensors operating at 10ghz and 77ghz," in *2017 IEEE Asia Pacific Microwave Conference (APMC)*, pp. 1306–1309, IEEE, 2017.

[103] D. Cottet, J. Grzyb, T. Kirstein, and G. Troster, "Electrical characterization of textile transmission lines," *IEEE Transactions on Advanced Packaging*, vol. 26, no. 2, pp. 182–190, 2003.

[104] A. H. M. Shirazi, A. Nikpaik, S. Mirabbasi, and S. Shekhar, "A quad-core-coupled triple-push 295-to-301 ghz source with 1.25 mw peak output power in 65nm cmos using slow-wave effect," in *2016 IEEE Radio Frequency Integrated Circuits Symposium (RFIC)*, pp. 190–193, IEEE, 2016.